

6-2-2007

# Fabrication and characterization of three-dimensional magnetic media

David Doria

*Florida International University*

**DOI:** 10.25148/etd.FI15101217

Follow this and additional works at: <https://digitalcommons.fiu.edu/etd>

 Part of the [Electrical and Computer Engineering Commons](#)

---

## Recommended Citation

Doria, David, "Fabrication and characterization of three-dimensional magnetic media" (2007). *FIU Electronic Theses and Dissertations*. 3080.

<https://digitalcommons.fiu.edu/etd/3080>

This work is brought to you for free and open access by the University Graduate School at FIU Digital Commons. It has been accepted for inclusion in FIU Electronic Theses and Dissertations by an authorized administrator of FIU Digital Commons. For more information, please contact [dcc@fiu.edu](mailto:dcc@fiu.edu).

FLORIDA INTERNATIONAL UNIVERSITY

Miami, Florida

FABRICATION AND CHARACTERIZATION OF THREE-DIMENSIONAL  
MAGNETIC MEDIA

A thesis submitted in partial fulfillment of the

requirements for the degree of

MASTER OF SCIENCE

in

ELECTRICAL ENGINEERING

by

David Doria

2007

To: Dean Vish Prasad  
College of Engineering and Computing

This thesis, written by David Doria, and entitled Fabrication and Characterization of Three-Dimensional Magnetic Media, having been approved in respect to style and intellectual content, is referred to you for judgment.

We have read this thesis and recommend that it be approved.

Roman Chomko

Roberto Panepucci

Sakhrat Khizroev, Major Professor

Date of Defense: June 2, 2006

The thesis of David Doria is approved.

Dean Vish Prasad  
College of Engineering and Computing

Dean George Walker  
University Graduate School

Florida International University, 2007

## DEDICATION

I dedicate the research to my parents; who have given me their never-ending support and love, bestowing in me the utmost confidence to complete the tasks at hand. Their selflessness and support have provided to me the opportunity to proceed through graduate school with the ability to concentrate completely on my studies.

## ACKNOWLEDGMENTS

I would like to acknowledge all the members whom I have worked side by side with during the last year: Nissim Amos, Yazan Hijazi, Rabee Ikkawi, Nikhil Joshi, and Andre Lavrenov. Through their support and the environment of a teamwork oriented laboratory, instilled by them before I arrived, I have been able to learn and complete the necessary duties to effectively complete my research. I would especially like to thank Dr. Sakhrat Khizroev and Dr. Roman Chomko for their guidance and the opportunity they have given me to learn, research, and excel in Nanomagnetism and the data storage trade, through class work and experimental analysis

ABSTRACT OF THE THESIS  
FABRICATION AND CHARACTERIZATION OF  
THREE-DIMENSIONAL MAGNETIC MEDIA

by

David Doria

Florida International University, 2007

Miami, Florida

Professor Sakhrat Khizroev, Major Professor

Conventional longitudinal magnetic recording has scarcely progressed the last couple of years, leaving the data storage industry frantically searching for alternative ways to store information and increase memory areal density. The research was directed towards the development of three-dimensional magnetic memory for recording purposes. Three-dimensional memory, an alternative to longitudinal recording, would achieve well over the current areal density of the latter. Another focus of the research was directed towards development of the magneto-optical Kerr effect (MOKE) magnetometer, an important tool used to measure magnetic behavior through hysteresis curves.

The fabrication of three-dimensional media was prepared with the aid of a sputtering system and focused ion beam (FIB). Amongst the metals exploited for fabrication of three-dimensional media were cobalt, palladium, tantalum, and permalloy. Examination of fabricated magnetic films was investigated with utilization of the magneto-optical Kerr effect magnetometer, atomic force microscope (AFM), magnetic force microscope (MFM), and x-ray diffractometer.

# TABLE OF CONTENTS

CHAPTER	PAGE
1. INTRODUCTION .....	1
2. BACKGROUND THEORY .....	2
2.1 Physics of Magnetism .....	3
2.2 Origin of Magnetism .....	5
2.3 Types of Magnetism .....	11
2.4 Temperature on Magnetic Behavior .....	15
2.5 Magnetic Domains and Domain Walls .....	16
2.6 Hysteresis .....	18
2.7 Soft and Hard Magnetic Materials .....	20
2.8 Superparamagnetism .....	23
3. DESCRIPTION OF THREE-DIMENSIONAL MEDIA .....	24
3.1 Perpendicular Anisotropy .....	25
3.2 Physics of Three-Dimensional Media .....	29
3.3 Writing on Three-Dimensional Media .....	33
3.4 Reading on Three-Dimensional Media .....	37
3.5 Patterned Media .....	38
3.6 Patterned Soft Underlayer .....	39
4. FABRICATION OF THREE-DIMENSIONAL MEDIA .....	44
4.1 Sputtering Process .....	46
4.2 Deposition of Soft Magnetic Underlayer .....	50
4.3 Focused Ion Beam for Patterning .....	51
4.4 Deposition of Magnetic Layers .....	52
5. RESULTS - MAGNETO-OPTICAL KERR EFFECT SYSTEM SETUP .....	54
5.1 Polarization of Light .....	55
5.2 Magneto-Optical Kerr Effect Theory .....	58
5.3 Magneto-Optical Kerr Effect Setup .....	61

6.	RESULTS - CHARACTERIZATION OF MAGNETIC MEDIA .....	64
6.1	Magneto-Optical Kerr Effect Magnometer.....	69
6.2	Atomic Force Microscopy .....	80
6.3	Magnetic Force Microscopy .....	83
6.4	X-Ray Diffraction.....	84
7.	CONCLUSIONS.....	88
	REFERENCES .....	91



## LIST OF TABLES

TABLE	PAGE
Table 1: Quantum numbers.....	7
Table 2: Types of magnetism, susceptibility, and magnetic behavior.....	11
Table 3: Deposition rates established for different metals.....	49
Table 4: Deposition parameters for different permalloy samples.....	50
Table 5: Deposition layers for different multilayer samples .....	53
Table 6: Coercivity dependence on cobalt and palladium thickness .....	72
Table 7: Remanence dependence on cobalt and palladium thicknesses .....	72
Table 8: Squareness factor dependence on cobalt and palladium thicknesses .....	73
Table 9: Coercive squareness factor dependence on cobalt and palladium thicknesses .....	74
Table 10: Maximum energy product dependence on cobalt and palladium thicknesses .....	74
Table 11: Magnetic behavior dependence on layer repetition of cobalt and palladium.....	75
Table 12: Magnetic behavior dependence on Co <sub>70</sub> Cr <sub>18</sub> Pt <sub>12</sub> magnetic layer thickness.....	75
Table 13: Magnetic characteristics of Co/Pd sample.....	76
Table 14: Magnetic characteristics of flat and patterned permalloy.....	78
Table 15: Magnetic characteristics of flat and patterned permalloy.....	79

## LIST OF FIGURES

FIGURE	PAGE
Figure 1: Earth's magnetic field and its geographical poles .....	2
Figure 2: Orbital magnetic moment and spin magnetic moment.....	5
Figure 3: Orbital energy diagram.....	8
Figure 4: Saturation magnetization as a function of temperature .....	15
Figure 5: Domain division (a) single domain (b) two domains (c) four domains (d) closure domains.....	16
Figure 6: Domain walls showing (a) Bloch domain wall (b) and Néel domain wall [6].....	17
Figure 7: Hysteresis loop and its relation to domains [5] .....	19
Figure 8: Variations of hysteresis loops for soft and hard magnetic materials [5] .....	20
Figure 9: B-H energy product within a hysteresis curve .....	22
Figure 10: Diagram showing (a) perpendicular media and (b) 3-D magnetic media [8] .....	24
Figure 11: Shape anisotropy and crystalline anisotropy due to thickness .....	26
Figure 12: (a) Interfacial and crystalline anisotropy orienting the easy axis and (b) thickness dependence of perpendicular anisotropy due to anisotropy [12] .....	27
Figure 13: Perpendicular anisotropy due to cobalt hexagonal closed packed structure.....	28
Figure 14: (a) 3-D multi-level and (b) 3-D absolute recording modes [8] .....	29
Figure 15: Magnetic layers exchange decoupled by non-magnetic layers .....	30
Figure 16: Simulations of effect of interlayer thickness where (a) the magnetic layers are coupled and (b) the magnetic layers are decoupled [8].....	31
Figure 17: (a) Co/Pt stack for perpendicular recording and (b) 3-D multilayers Co (top) used as a magnetic layer and Co/Pt (bottom) thin layers that constitutes a single magnetic layer [8].....	32

Figure 18: Simulation of demagnetization field within a perpendicular magnetic layer..... 32

Figure 19: (a) Identification of layers during writing and (b) cross-sectional diagrams showing two time moments where field due to the biasing wire is used to identify layers [8]..... 33

Figure 20: Multilevel recording through variation of write current ..... 34

Figure 21: (a) Single grid structure and (b) magnetization near (c) and far from the bottom layer [8]..... 35

Figure 22: Field penetrating through multilayers during recording..... 35

Figure 23: Recording on (a) an erased media (b) and on previously recorded adjacent cells [8] ..... 36

Figure 24: (a) Stray field verses digital level (b) and signal-to-noise ratio verses number of layers [8]..... 37

Figure 25: Patterned media with island diameter of 50 nm by focused ion beam [8]..... 38

Figure 26: (a) Longitudinal (b) and perpendicular recording with soft underlayer [17]..... 39

Figure 27: (a) Noise due to movement of domain walls (b) and reduction of noise with biasing [18] ..... 40

Figure 28: Convex patterned soft under layer to move image head [19]..... 41

Figure 29: (a) Effect of soft underlayer through the media (b) and field gradients along the track..... 42

Figure 30: Effect of patterned soft underlayer on readback sensitivity ..... 42

Figure 31: Fields through magnetic layers without a soft underlayer ..... 43

Figure 32: Fields through magnetic layers with convex patterned soft underlayer..... 43

Figure 33: Deposition through a sputtering system [3] ..... 45

Figure 34: Image of patterned permally through the focused ion bea, ..... 51

Figure 35: Propagation of linearly polarized light [3] .....	56
Figure 36: Propagation of circularly polarized light [3] .....	57
Figure 37: Propagation of elliptically polarized light [3] .....	57
Figure 38: Reflection geometry off a magnetized sample and orientation of p and s directions [22].....	59
Figure 39: (a) Longitudinal p-polarized (b) and s-polarized incident beams .....	59
Figure 40: (a) Transverse aligned (b) and polar aligned incident reflection beams .....	60
Figure 41: Optical chopper to pulse the laser and the controller to adjust the frequency.....	61
Figure 42: (a) Magnets aligned to analyze in longitudinal mode (b) and perpendicular mode.....	62
Figure 43: Magneto-optical Kerr effect magnetometer layout .....	63
Figure 44: Atomic force microscope consisting of laser, cantilever, and photodetectors .....	65
Figure 45: Magnetic force microscope utilized to analyze magnetic films .....	67
Figure 46: X-ray diffraction (a) Rayleigh scattering and (b) interference [3] .....	68
Figure 47: Hysteresis curve for fabricated multilayer sample observed from magnetometer.....	70
Figure 48: Hysteresis curve for fabricated $\text{Co}_{70}\text{Cr}_{18}\text{Pt}_{12}$ sample observed from magnetometer.....	71
Figure 49: Hysteresis curve for Co/Pd sample observed from magnetometer .....	76
Figure 50: Hysteresis curve for fabricated permalloy sample without patterns .....	77
Figure 51: Hysteresis curve for fabricated permalloy sample with patterns .....	78
Figure 52: Hysteresis curve for fabricated permalloy sample of 400 nm.....	79
Figure 53: AFM image in 3D of step coverage for rate determination .....	80
Figure 54: AFM utilization for step height measurements and rate determination .....	81

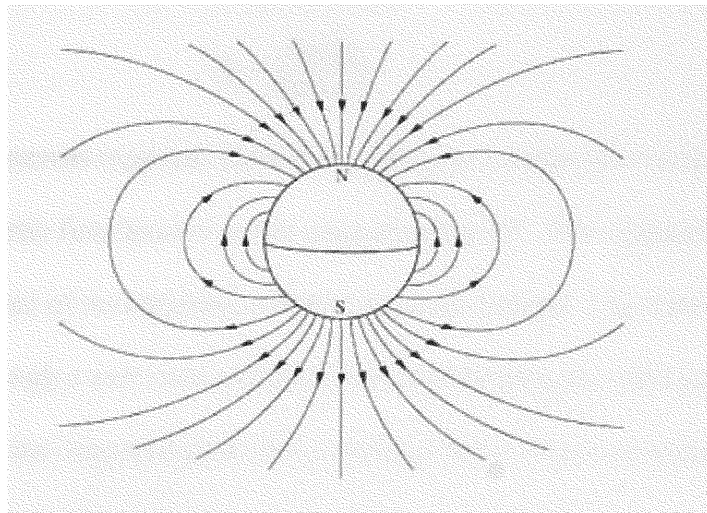
Figure 55: (a) AFM image of a patterned permalloy sample in 2D mode (b) and in 3D mode.....	82
Figure 56: AFM image of sputtered permalloy at 100 nm .....	82
Figure 57: MFM image of permalloy with domains aligned.....	83
Figure 58: X-ray diffraction on palladium cubic face centered structure.....	84
Figure 59: X-ray diffraction on tantalum cubic body centered structure.....	85
Figure 60: X-ray diffraction on cobalt.....	86
Figure 61: X-ray diffraction showing peaks for tantalum, silicon, and palladium.....	87

## 1. INTRODUCTION

The storage device industry is continuously facing the challenge to increase the storage capacity and read and write speeds while simultaneously reducing cost manufacturing. The trend for smaller, faster computers, high speed, huge databases for internet applications, more capable home and supercomputers, and the rapid growth of broadband communications promotes the storage device industry to further downscale the areal density within memory. Magnetic longitudinal recording, the current conventional technique for memory, has been the mainstream data storage technology for more than four decades [1]. The growth rate of areal density has exceeded 100 percent per year in the past, where the newest advances by leading companies are in the range of beyond 100 Gbit/in<sup>2</sup>, which corresponds to a 160 x 40 nm<sup>2</sup> bit cell) [2]. Nonetheless, there has been a slow progression in recent years in longitudinal magnetic recording due to the superparamagnetic limit. The superparamagnetic limit in longitudinal recording no longer permits the continuous downscaling of bit sizes. The halt of downscaling due to the superparamagnetic limit is due to the thermal energy becoming comparable to the magnetostatic energy stored for a grain, causing instability in storing information, where the push for high accuracy is demanded by the data storage industry. New approaches are currently being explored to continue the push for higher areal densities past the current superparamagnetic limit. Therefore, this study becomes significant because it provides an alternative to conventional longitudinal media which would provide higher areal density in magnetic memory. This study will also address some issues and provide schemes in fabrication of three-dimensional magnetic memory.

## 2. BACKGROUND THEORY

A dipole is a pair of electric charges or magnetic poles that oppose each other, separated by some distance. Dipoles can be characterized by their dipole moment, which is a vector quantity expressed by the product of the charge or magnetic strength of one of the poles and the distance between the two opposing poles. The direction of the dipole moment corresponds to the direction from the magnetic south pole pointing towards the magnetic north pole. The magnetic field generated from a magnetic dipole flows outward from the north pole and into the south pole. Magnetic dipoles are generated by current loops or quantum mechanical moments because of the absence of magnetic monopoles in nature. Figure 1 illustrates the Earth's magnetic field and its magnetic poles, where the geographical north and south poles are the reversed magnetic south and north poles, respectively.



**Figure 1: Earth's magnetic field and its geographical poles**

## 2.1 Physics of Magnetism

The electric field and the magnetic field can be described from Lorentz force law. The Lorentz force law indicates that the direction of the force due to magnetism is perpendicular to both the velocity of the moving charge and the magnetic field as shown in Equation 1. The force  $F$  in Equation 1 is the vector sum of the electric field and the cross product of the magnetic field with the velocity of the moving charge.

$$\vec{F} = q\vec{E} + q\vec{v} \times \vec{B} \quad (1)$$

Equation 2 portrays the magnetic force of two opposite poles that attract with a force that is inversely proportional to the distance between them. The masses of the two particles are represented by  $m_1$  and  $m_2$ , with the distance  $r$  between them. The constant  $\mu_0$  is known as the permeability of free space,  $4\pi \times 10^{-7} \text{ Hm}^{-1}$ , which is the ratio of the induction divided by an external field in a vacuum.

$$F = \frac{m_1 m_2}{4\pi \mu_0 r^2} \quad (2)$$

When an external magnetic field  $H$  is applied to a material, it responds by generating a magnetic field known as the magnetization  $M$ . The magnetization of the material is a measure of the magnetic moment per unit volume. The total flux of magnetic field through a unit cross sectional area, considering the external applied magnetic field and the magnetization of the material itself, is known as magnetic induction,  $B$ . These three parameters are related through Equation 3 in International System of Units.

$$B = \mu_0 (H + M) \quad (3)$$



The magnetic susceptibility  $\chi$  is a measure of how magnetizable a material is in the presence of an external magnetic field, which can be used to express the different types of magnetism, as seen in Equation 4, described by the magnetization of the material over the external magnetic field.

$$\chi = M / H \quad (4)$$

The relative permeability of the material  $\mu$  also describes the effect of an external magnetic field on its magnetism, as seen in Equation 5, described by the ratio of the magnetic induction over the external magnetic field.

$$\mu = B / H \quad (5)$$

The torque  $\tau$  exerted by the magnetic force is shown in Equation 6. The torque is perpendicular to the magnetic field and the magnetic moment  $\mu$  through the cross product of the two.

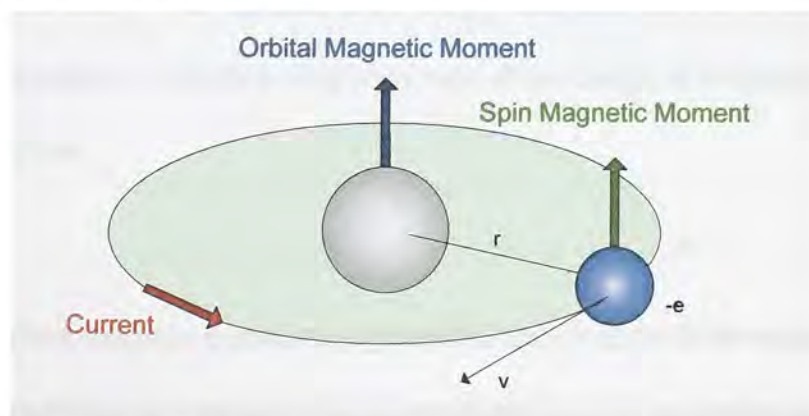
$$\tau = \mu \times B \quad (6)$$

The Biot-Savart law completely specifies the magnetic field generated by a current. The magnetic field can be calculated through the current density  $j$  and the radius of the loop, detailed in Equation 7.

$$B(r) = \frac{\mu_0}{4\pi} \int \frac{j(r') \times (r-r')}{|r-r'|^3} d^3r' \quad (7)$$

## 2.2 Origin of Magnetism

Magnetic fields are dipolar in nature, having north and south poles, which also applies to a single electron in an atom. When placed in a magnetic field, a magnetic dipole tends to align itself in opposed polarity to that field, in an effort to reduce the total energy stored. Magnetism is generated from two types of motions of the electrons within atoms. The first type of motion of electrons inside an atom is the motion of the electrons in an orbit around the nucleus of the atom. The second type of motion of electrons originates from the spin of the electrons around its own axis. The orbital motion and the spin motion independently produce an orbital magnetic moment  $\mu_L$  and spin magnetic moment  $\mu_S$  on each electron, respectively, causing them to behave similar to atomic permanent magnets, illustrated in Figure 2. In most elements the magnetic moments of the electrons cancel each other because of the Pauli Exclusion Principle, which states that each electron orbit can be occupied by only two electrons of opposite spin. However, a few elements, namely the transition metals of iron, cobalt and nickel, have magnetic moments that do not cancel.



**Figure 2: Orbital magnetic moment and spin magnetic moment**

Magnetism can be generated by electric current in a loop which produces an orbital magnetic momentum, expressed in Equation 8. The orbital magnetic moment is given by the product of the current  $I$  and the area of the loop  $A$ .

$$\mu_L = I A \quad (8)$$

The orbital magnetic moment can also be described for an electron orbiting around an atom. With an orbital radius  $r$  and an angular frequency  $\omega$ , the orbital magnetic moment of an electron can be expressed, shown in Equation 9, where the charge of an electron is  $1.602 \times 10^{-19}$  C.

$$\mu_L = -\frac{1}{2} |e| \omega r^2 \quad (9)$$

The angular momentum for an electron circumnavigating in an orbit describes the momentum about the axis of rotation. The angular momentum of an electron is dependant on the angular frequency and the radius, presented in Equation 10, where the mass of an electron  $m_e$  is  $9.109 \times 10^{-31}$  kg.

$$L = m_e \omega r^2 \quad (10)$$

The ratio of the orbital magnetic moment and the angular momentum is known as the gyromagnetic ratio  $\gamma$ . The expression for the gyromagnetic ratio of an electron is displayed in Equation 11, which is simply the ratio of the charge of an electron and the mass of an electron.

$$\gamma = \frac{-|e|}{2 m_e} \quad (11)$$

The smallest magnetic momentum quantum is known as the Bohr magneton  $\mu_B$ . The Bohr magneton is the product of the gyromagnetic ratio of an electron and Plank's

constant  $h$ ,  $6.626 \times 10^{-34}$  Js, divided by  $2\pi$ , shown in Equation 12. The ratio of Planck's constant divided by  $2\pi$  is commonly represented by the symbol  $\hbar$ .

$$\mu_B = \frac{-|e|\hbar}{2 m_e} \quad (12)$$

The state of an electron in an atom can be conveyed by four quantum numbers.

The four quantum numbers specify the complete and unique quantum state of a single electron, which are known as the principal quantum number, orbital angular momentum quantum number, magnetic quantum number, and spin quantum number, denoted as  $n$ ,  $l$ ,  $m$ , and  $s$ , respectively, detailed in Table 1.

Number	Denoted	Allowed Range	Explanation
Principal quantum number	N	Positive integer	overall energy of orbital and distance from the nucleus of an electron
Orbital angular momentum quantum number	L	$n - 1$	orbital angular momentum number of an electron
Magnetic quantum number	M	integer from $-l$ to $l$	related to the magnetic momentum of an electron
Spin quantum number	S	$\frac{1}{2}$ or $-\frac{1}{2}$	intrinsic angular momentum of an electron

**Table 1: Orbital energy diagram**

The Schrödinger wave equation describes energy eigen states that have corresponding real numbers  $n$ , known as the principal quantum number, which define the discrete energy levels  $E_n$ . The discrete energy levels are described by the first energy level  $E_1$  divided by the square of the principal quantum number. The principal quantum number represents the relative overall energy of each orbital, where the energy of each orbital increases as the distance from the nucleus increases. The set of orbitals with the same  $n$  value are referred to as electron shells or energy levels. The principal quantum numbers are real positive numbers (1, 2, 3, 4 ...) designated by letters (K, L, M, N ...).

The orbital angular momentum quantum number represents an atomic orbital which determines its orbital angular momentum. The orbital angular momentum quantum number can consist of an integer from zero to one less than the principal quantum number. These quantum numbers (0, 1, 2, 3 ...) are designated by letters (s, p, d, f ...), which represent the orbitals, or subshells, as seen in Figure 3. The orbital angular momentum  $L$  can be described by the orbital angular momentum quantum number as seen in Equation 13.

$$\vec{L} = \hbar [l(l+1)]^{1/2} \quad (13)$$

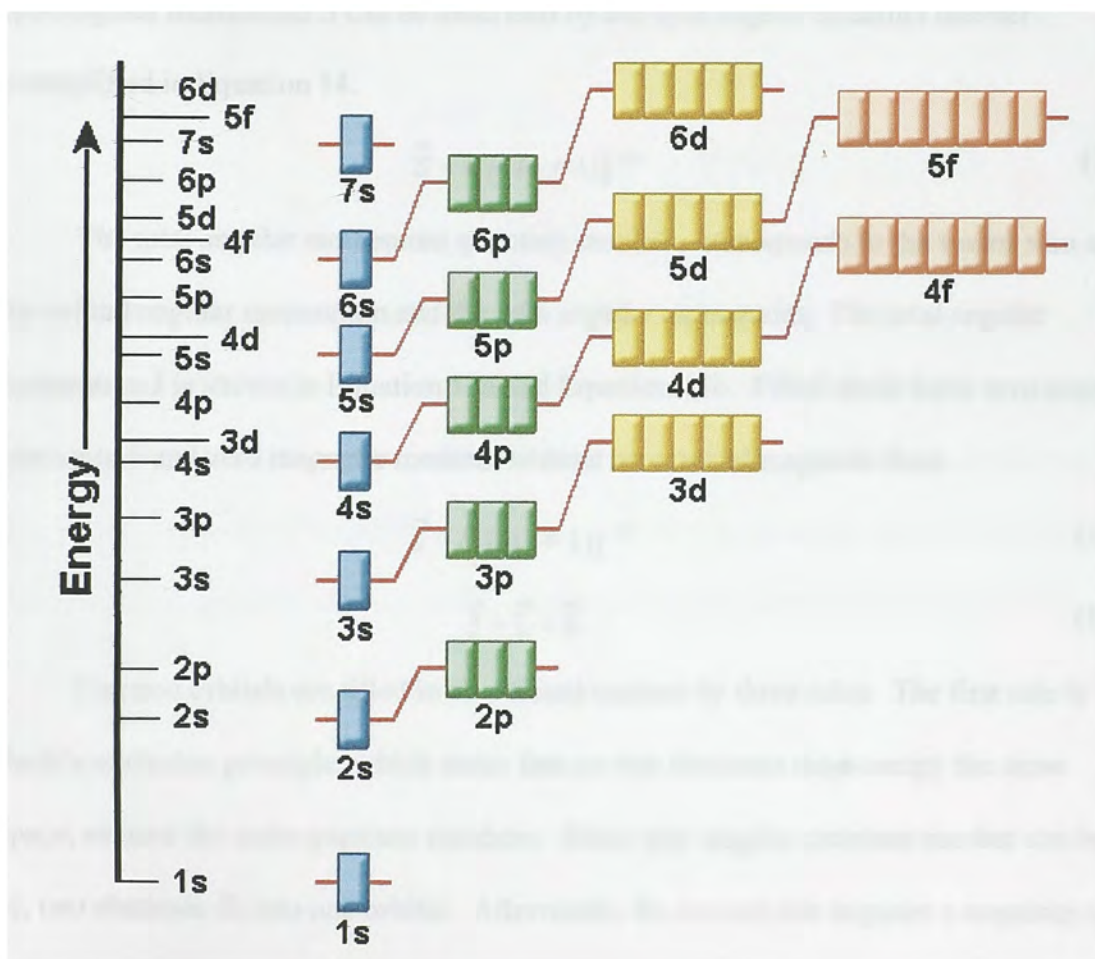


Figure 3: Orbital energy diagram

The magnetic quantum number describes the unique quantum state of an electron. The magnetic quantum number denotes the energy levels available contained by an orbital. The total number of available energy levels contained by an orbit is one plus double the orbital angular momentum quantum number. These available energy levels can range from the negative orbital angular momentum quantum number to the positive orbital angular momentum quantum number  $(-l, l + 1 \dots 0 \dots l - 1, l)$ .

The spin angular quantum number quantifies the intrinsic angular momentum of an electron. The spin angular quantum number of an electron possesses a spin of  $\pm \frac{1}{2}$ . The spin angular momentum  $S$  can be described by the spin angular quantum number exemplified in Equation 14.

$$\vec{S} = \hbar [s (s + 1)]^{-1/2} \quad (14)$$

The total angular momentum quantum number  $j$  corresponds to the vector sum of the orbital angular momentum and the spin angular momentum. The total angular momentum  $J$  is shown in Equation 15a and Equation 15b. Filled shells have zero angular momentum and zero magnetic moment without an external magnetic field.

$$\vec{J} = \hbar [j (j + 1)]^{-1/2} \quad (15a)$$

$$\vec{J} = \vec{L} + \vec{S} \quad (15b)$$

Electron orbitals are filled in an ordered manner by three rules. The first rule is Pauli's exclusion principle, which states that no two electrons may occupy the same space, or have the same quantum numbers. Since spin angular quantum number can be  $\pm \frac{1}{2}$ , two electrons fit into one orbital. Afterwards, the second rule imposes a sequence to inserting electrons, where orbitals are filled in order of increasing energy. Hund's rule describes the third rule of ordering, which states that electrons are added with parallel,

aligned spin until half the orbital is full, maximizing the spin angular momentum. After the orbital is half full, the electrons are all inserted with opposite spin; pairing up to the electrons of opposing spin until the orbital are completely filled, resulting in zero spin angular momentum. Furthermore, the energies of the shells vary according to their principle quantum number, evident when the 4s shell gives up an electron to the 3d shell, where these elements consequently have the possibility of larger magnetic moments [3].

The magnetic moment is related to the angular momentum of a quantum state through the Landé g-factor  $g_j$ . The Landé g-factor is calculated through the total angular momentum, orbital angular momentum, and the spin angular momentum as seen in Equation 16.





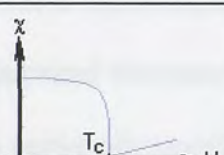

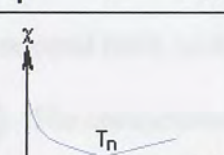
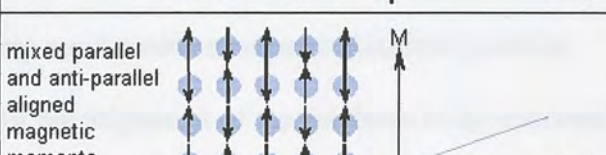
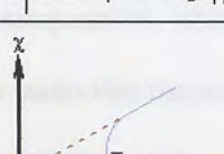

$$g_j = 1 + \frac{\vec{J}(\vec{J} + 1) + \vec{S}(\vec{S} + 1) - \vec{L}(\vec{L} + 1)}{2\vec{J}(\vec{J} + 1)} \quad (16)$$

From the derivations of the different quantum moments and angular moments, the magnetic moment of an atom  $\mu$  can be derived, which is related to the orbital magnetic moment of current in a loop and atomic magnetic moment described in the beginning of the section. The magnetic moment can be calculated through the product of the Landé g-factor, Bohr magnetron, and the total angular momentum, displayed in Equation 17.

$$\mu = -g_j \mu_B \vec{J} \quad (17)$$

## 2.3 Types of Magnetism

All materials can be classified into one of the various types of magnetism, which describe how materials respond to magnetic fields. The five types of groups which describe the magnetic behavior and susceptibility materials are diamagnetism, paramagnetism, ferromagnetism, ferrimagnetism, and antiferrimagnetism, shown in Table 2. These five classifications of magnetism are dependant on the susceptibility and the magnetic behavior in the presence of external magnetic fields and temperature

Type of Magnetism	Susceptibility	Magnetic Behavior
Diamagnetism		no magnetic moment 
Paramagnetism		randomly oriented magnetic moments 
Ferromagnetism		parallel aligned magnetic moments 
Antiferromagnetism		mixed parallel and anti-parallel aligned magnetic moments 
Ferrimagnetism		anti-parallel aligned magnetic moments 

**Table 2: Types of magnetism, susceptibility, and magnetic behavior**



Diamagnetism is a fundamental property of all materials. The orbital motion of electrons creates atomic current loops which produce magnetic fields. When an external magnetic field is applied to a material, these current loops do not cooperate and tend to oppose the applied field, though it is usually very weak, which may be viewed as an atomic version of Lenz's law [4]. Diamagnetic materials are composed of atoms absent of any magnetic moments, signifying that all the orbital shells are filled and all electrons are paired. However, a negative magnetization is produced when the material is exposed to an external magnetic field, resulting in negative susceptibility,  $\chi$ , which describes the magnetization of a material in response to a magnetic field. The negative magnetic susceptibility in diamagnetic materials is the effect of the current produced induced in the electron orbits by the applied field. Diamagnetic materials also have the characteristic behavior of having susceptibility independent of temperature.

Paramagnetic materials exhibit a magnetization proportional to the applied magnetic field. These materials are composed of atoms that introduce a net magnetic moment due to unpaired electrons in partially filled orbits. In the presence of an external magnetic field, a partial alignment of the atomic magnetic moments is developed in the direction of the external field, yielding a net positive magnetization and positive susceptibility [4]. The competence of the alignment of the moments to the external field is disordered by temperature, where this temperature dependency is known as Curie's law. Curie's law states that the magnetization of the material is proportional to the field divided by the temperature; hence, the susceptibility is inversely proportional to the temperature through the Curie constant C as shown in Equation 18.

$$\chi = C / T \quad (18)$$

Ferromagnetism is the type of magnetism which exhibits a practical amount of magnetization and responsible for most of the magnetic behavior encountered in everyday applications. Ferromagnetic materials exhibit a large exchange energy which causes adjacent atoms to magnetize in the same direction to minimize the energy. Iron, cobalt, and nickel are the more common materials that demonstrate the magnetic behavior of ferromagnetism. Ferromagnetic materials have a parallel alignment of magnetic moments that result in a large net magnetization, even with the absence of an external magnetic field. The magnetization of ferromagnetic materials is highly susceptible to magnetic fields which can saturate at moderate magnetic fields. Ferromagnetic materials can retain a memory, or remanence magnetization, of an external applied magnetic field once it is removed. A sufficient magnetic field in the opposite direction of its current magnetization must be applied to demagnetize the material and eventually magnetizes the material towards the direction of the new magnetic field. The exchange energy in ferromagnetic materials is ultimately overcome by thermal energy at higher temperatures, where these materials behave similar to paramagnetic materials. Due to their favorable magnetic properties, ferromagnetic materials are widely used for transformers, permanent magnets, and data storage.

In ionic compounds, typically oxides, more complex forms of magnetic ordering occur as a result of the crystal structure of the material. The magnetic ordering of ferromagnetism occurs when the magnetic structure is composed of two sublattices separated by oxygen. The oxygen mediates the exchange energy between the two lattices, which induces a parallel but opposite alignment. The net magnetic moment is the sum of the two opposite moments, where one lattice provides a larger contribution to

the total magnetism of the material than the other. However, ferrimagnetic materials are similar to ferromagnetic materials since they both exhibit the same magnetic behaviors of hysteresis, remanence, and both are affected by temperature. Beyond the Néel temperature  $T_n$ , ferrimagnetic materials behave similar to paramagnetic materials.

Antiferromagnetic materials are also compounds that form complex magnetic ordering due to the mediation of oxygen between the sublattices. However, antiferromagnetic materials have a net magnetic moment of zero because the moments of the different sublattices are opposite and equal. Beyond the Néel temperature, antiferromagnetic materials behave similar to paramagnetic materials.

## 2.4 Temperature on Magnetic Behavior

Temperature can influence the magnetic characteristics of materials. A raise of the temperature yields an increase in the magnitude of the thermal vibrations of atoms [5]. Therefore, the atomic magnetic moments become free to rotate, randomizing the directions of any moments that may be aligned. The thermal moments counteract the coupling forces between the adjacent dipole moments causing dipole misalignment, the outcome effect showing a decrease in saturation magnetization [5]. As the temperature is increased, the saturation magnetization,  $M_s$ , diminishes gradually and abruptly reducing to near zero at the Curie temperature  $T_c$  shown in Figure 4. Below the Curie temperature, exchange interactions are strong relative to the external magnetic field. Beyond the Curie temperature, the mutual spin coupling forces are completely destroyed, where ferromagnetic and ferrimagnetic material behave similar to paramagnetic materials.

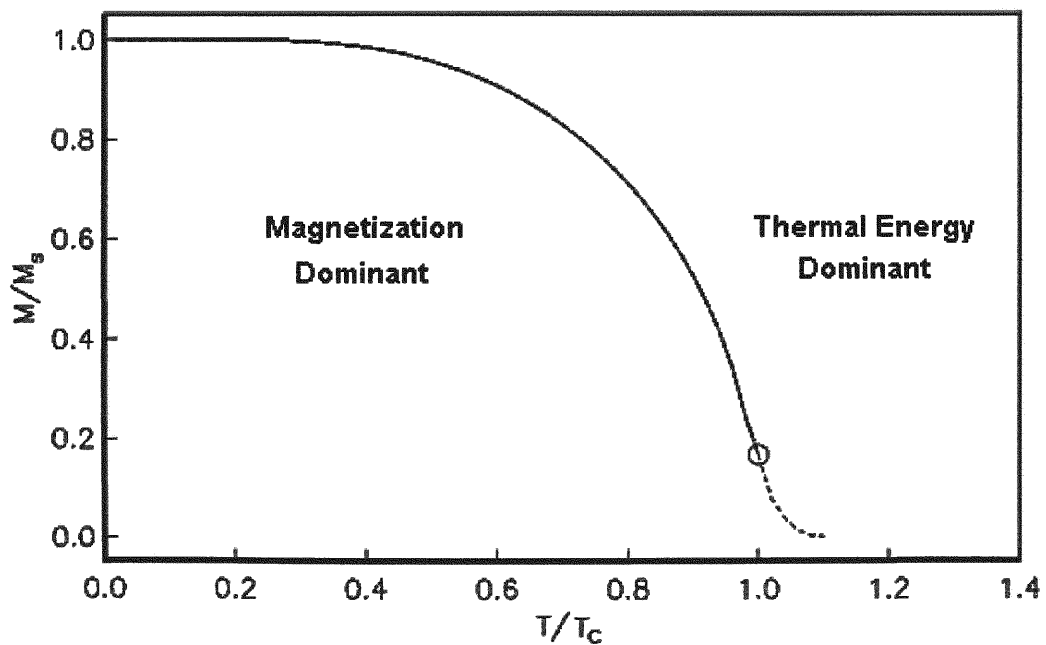
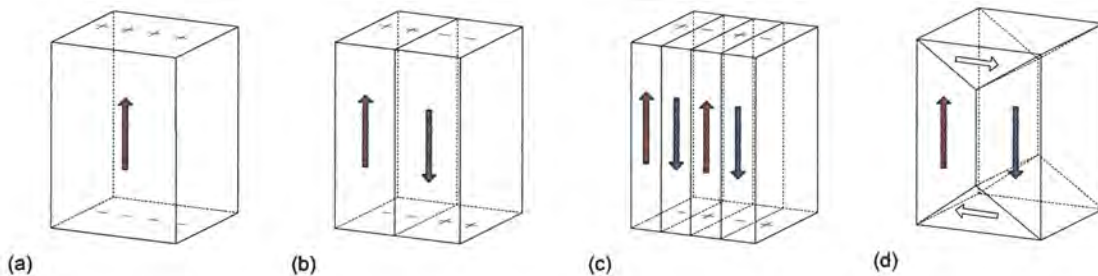


Figure 4: Saturation magnetization as a function of temperature

## 2.5 Magnetic Domains and Domain Walls

Ferromagnetic and ferrimagnetic materials, below the Curie temperature, are composed of small volume regions containing mutual alignment of all magnetic dipoles moments called domains. Within each domain, the magnetization of that domain is saturated. Adjacent domains are separated by domain walls, where the direction of the magnetization gradually shifts from the alignment of one domain to the other. The magnitude of the magnetic field for the entire solid is the vector sum of the magnetization of all the domains, where each domain contributes a fraction weighted by its volume. Magnetic domains in ferromagnetic materials are generated in order to minimize the sum of energy terms, magnetostatic energy, exchange energy, anisotropy energy, and Zeeman energy [6]. Films are separated into domains with different orientations of magnetization to reduce the magnetostatic energy, illustrated in Figure 5.

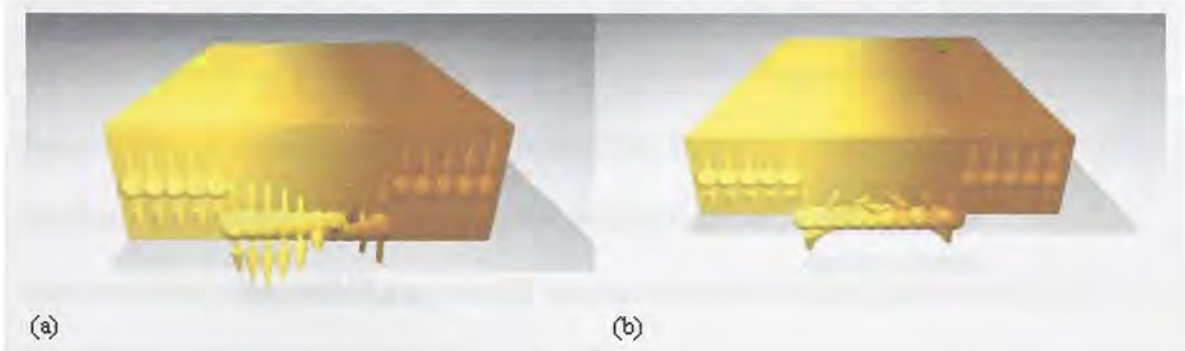


**Figure 5: Domain division (a) single domain (b) two domains (c) four domains (d) closure domains**

Domain walls separate domains, magnetized with different orientations, reducing the energy through the width of the wall. The domain wall width is mainly determined by the exchange energy and anisotropy energy. Magnetostatic, or dipole, energy depends on the magnetization that arises from the alignment of magnetic dipoles, primarily from electron spins in solids [6]. A single domain finite sample has associated with it

significant magnetostatic energy, but the disintegration of the magnetization into domains reduces the total magnetostatic energy. Exchange energy depends on the basic spin interaction that causes cooperative magnetic ordering. The exchange energy tends to make a magnetic domain wall as wide as possible since the exchange energy decreases with decreasing angle between spins on neighboring atoms inside the wall [6].

The spins inside the wall rotate gradually, leading to a certain width of the magnetic domain wall, illustrated in Figure 6. The exchange energy between neighboring spins tends to increase the wall width. A larger rotation of spins between two neighbors causes higher exchange energy. The magnetic anisotropy energy depends on the orientation of the magnetization with respect to the crystallographic axes of the material, resulting from spin and orbit interaction [6]. Zeeman energy is the outcome of the interaction of the magnetization with external magnetic fields. The domain walls have two main types of spin structures within them, commonly known as Bloch and Néel domain walls. Within Bloch domain walls, the spin rotates in the plane parallel to the wall plane. The wall width of a  $180^\circ$  Bloch wall is proportional to the exchange constant and anisotropy energy [6]. Inside Néel domain walls, the spin rotates in the plan of the film.



**Figure 6: Domain walls showing (a) Bloch domain wall (b) and Néel domain wall [6]**

## 2.6 Hysteresis

The nonlinear relationship between the applied external magnetic field,  $H$ , and the magnetization of the material,  $M$ , is known as hysteresis. If the material is initially unmagnetized, zero magnetization, the domains are randomly oriented such that there is a net magnetization of zero. As the external magnetic field is increased, the magnetization of the material increases as well. The domains begin to align to the external magnetic field due to the changing of domain shapes and sizes resulting from the movement of the domain walls. After further increasing of the external field, the magnetization of the material reaches the saturation magnetization, where a further increase in external field has no effect on the magnetization. At this magnetization all the domains are aligned to the same direction as the external field, in effect becoming one domain. From saturation, as the external magnetic field is reduced by reversal of direction, the magnetization does not decrease through the same path as it was increased. When the external field reaches zero, the material remains magnetized at a magnetization known as the remanence,  $M_r$ . From saturation, additional energy is needed to reorient the domains in the opposite direction. With the absence of any external magnetic field, most of the magnetization remains, resembling a permanent magnet. To reduce the magnetization of the material back to zero, an opposing external magnetic field, known as the coercivity,  $-H_c$ , must be applied. Upon continuation of the applied field in the reverse direction, the magnetization of the material eventually reaches saturation in the negative end,  $-M_s$ . A second reversal towards the positive end yields the same outcome as when reaching negative saturation, where a negative remanence,  $-M_r$ , is the magnetization at the absence

external field and the coercivity,  $H_c$ , is the necessary external field to begin the increasing of the magnetization towards positive saturation.

The hysteresis loop shows the history dependant phenomenon of magnetization of a ferromagnetic material, shown in Figure 7. To reside within the hysteresis loop from the unmagnetized state, the material must reach its saturation magnetization. An unsaturated material would not have the same characteristics when opposing external magnetic fields are applied. However, a material within the hysteresis loop may be demagnetized by repeatedly alternating the external magnetic field while simultaneously decreasing the magnitude.

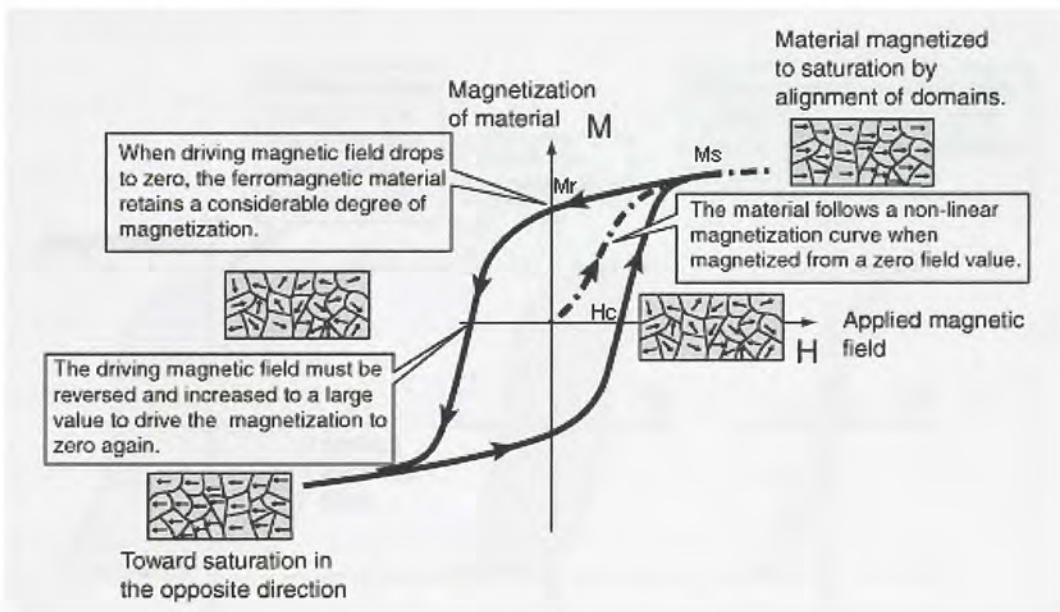
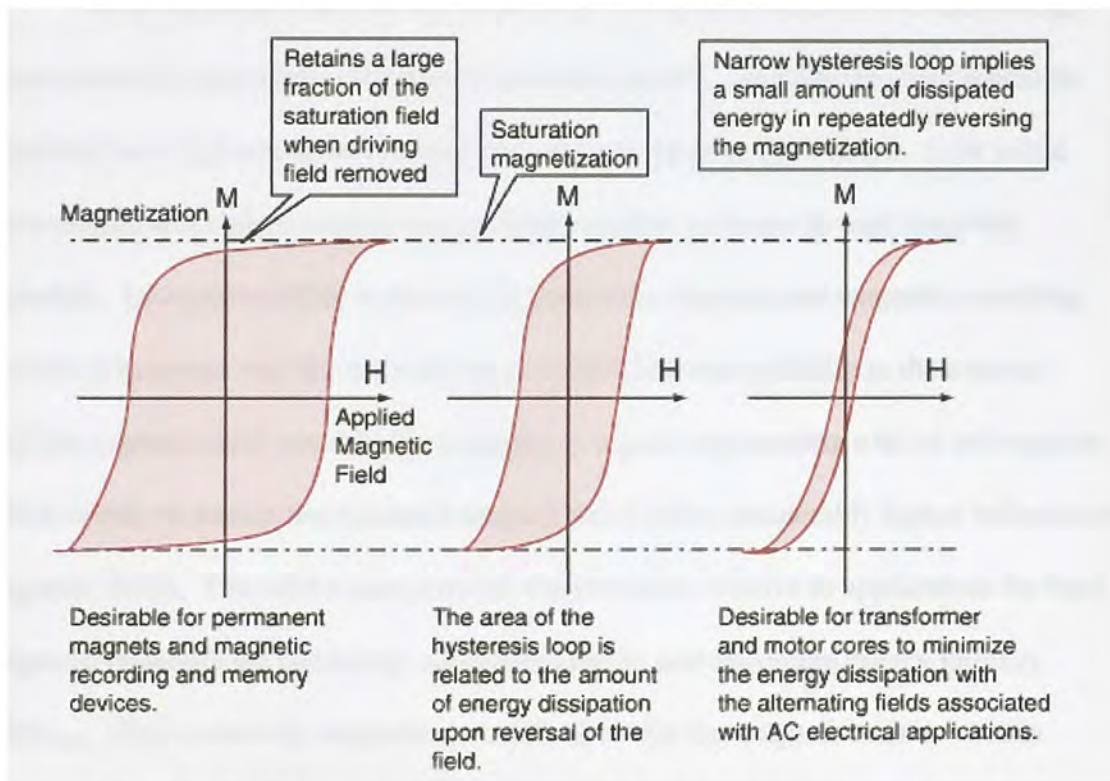


Figure 7: Hysteresis loop and its relation to domains [5]



## 2.7 Soft and Hard Magnetic Materials

Both ferromagnetic and ferrimagnetic materials can be classified as either a soft or hard magnetic material based on their hysteresis characteristics. The area within the hysteresis loop represents the magnetic energy loss per unit volume of the material per magnetization [5]. The area inside the hysteresis loop is the distinguishing characteristic in the hysteresis curves amongst the two, shown in Figure 8, where soft magnetic materials exhibit small areas and hard magnetic materials display larger areas. Due to the different variations in hysteresis, several applications have been developed which benefit from either that smaller or larger areas in the hysteresis curves



**Figure 8: Variations of hysteresis loops for soft and hard magnetic materials [5]**

Soft magnetic materials are applied to devices that are frequently exposed to alternating magnetic fields where the energy loss must be low, transformers being a

common exploitation of these materials. Additionally, soft magnetic materials must have a high initial permeability, where the permeability is correlated to the slope of the magnetization as a function of magnetic field. Low coercivities are also common to soft magnetic materials, signifying that saturation of the material is achievable by applying a low external magnetic field. Low values of coercivity correspond to the easy movement of domain walls as the external magnetic field is changed [5]. Ideally, soft magnetic materials also demonstrate remanent magnetization values of zero, indicating that removal of an external magnetic field causes the magnetization of the material to diminish.

Hard magnetic materials are employed in permanent magnets and data storage. These materials have high resistance to demagnetization. Additionally, hard magnetic materials have high remanence, coercivity, and saturation magnetization. Low initial permeability and high hysteresis energy losses are also common to hard magnetic materials. Low permeability is crucial for permanent magnets and magnetic recording because it becomes vital for the material to exhibit low susceptibility to the external applied magnetic field, resulting in a magnet or a grain representing a bit of information, which is able to sustain the remanent magnetization with considerably higher influence of magnetic fields. Two of the more crucial characteristics relative to applications for hard magnetic materials are coercivity, squareness factor, and maximum energy product,  $(BH)_{\max}$ . High coercivity magnetic materials allow for the magnetization to remain reasonably constant with an insufficient external magnetic field to overcome the coercivity and therefore demagnetizing or magnetizing in the opposite direction. Squareness factor  $S$ , calculated by the ratio of remanence by the saturation magnetization,

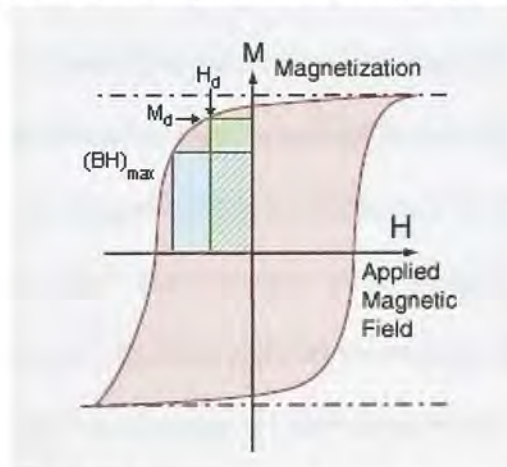
is a dimensionless number between zero and one, shown in Equation 19. The value of one denotes a perfect square; conversely, the value of zero signifies no remanence and no hysteresis, where larger squareness factors are desired for magnetic recording.

$$S = M_r / M_s \quad (19)$$

Coercive squareness, shown in Equation 20, is a ratio of the magnetic field at the intersection of the tangent line at the coercivity and the vertical line crossing through the remanent magnetization by the coercivity, a dimensionless number between zero and one.

$$S^* = \frac{H (M_r = \frac{dM}{dH}_{H_c})}{H_c} \quad (20)$$

The  $(BH)_{\max}$  is defined as the area of the largest B-H rectangle that can be formulated within the second quadrant of the hysteresis curve, illustrated in Figure 9. The value of the maximum energy product corresponds to the energy required to demagnetize a permanent magnet, signifying that larger  $(BH)_{\max}$  values represents the need for larger energy values to demagnetize the material [5].



**Figure 9: B-H energy product within a hysteresis curve**

## 2.8 Superparamagnetism

Superparamagnetism is a phenomenon by which magnetic materials may exhibit a paramagnetic behavior at temperatures below the Curie temperature. Normally, coupling forces in ferromagnetic materials cause the magnetic moments of adjacent atoms to align, generating very large magnetic fields. At temperatures above the Curie temperature, the thermal energy overcomes the coupling forces, causing the atomic magnetic moments to fluctuate randomly [3]. Because there is no longer any magnetic order, the internal magnetic field no longer exists and the material exhibits paramagnetic behavior.

Superparamagnetism occurs when the material is composed of small grain sizes, ranging less than 20 nm [3]. Magnetic materials with grain sizes at this range, and temperature below the Curie temperature, where the thermal energy is not sufficient to overcome coupling forces between adjacent atoms, the thermal energy is still sufficient to change the direction of magnetization of the entire grain. The ensuing fluctuations in the direction of magnetization cause the total magnetization to cancel. The material behaves paramagnetic, except that instead of each individual atom independently influenced by an external magnetic field, the magnetic moment of the entire crystallite tends to align with the magnetic field. As the grain size decreases, so does anisotropy energy, consequently decreasing the temperature at which the material becomes superparamagnetic [3]. To ensure at least ten year stability, Equation 21 demonstrates the superparamagnetic limit dependant on the recording layer anisotropy energy  $K_U$ , the thermal activation volume  $V$ , Boltzmann's constant at  $1.38 \times 10^{-23} \text{ m}^2\text{kgs}^{-2}\text{K}^{-1}$ , and the temperature  $T$  [27].

$$K_U V \times (k_B T)^{-1} \sim 40-60 \quad (21)$$

### 3. DESCRIPTION OF THREE-DIMENSIONAL MEDIA

Several technologies have been proposed and recently developed to address the superparamagnetic limit. The near-future approaches to defer the superparamagnetic limit have been perpendicular media, patterned media, and heat-assisted magnetic recording (HAMR), all of which are two dimensional alternatives. However, to further exceed well past the one terabit/in<sup>2</sup> mark, it seems evident for the need to stack recording layers in a vertical dimension, known as three-dimensional (3-D) magnetic recording. The orientation of the bits in three-dimensional recording is perpendicular to the magnetic layer. Information could be recorded through the surface, where more than one bit can be recorded on the same unit area as compared with two-dimensional media as illustrated in Figure 10. The effective areal density would grow by a factor of N, where N is the number of the layers, which are separated by the non-magnetic layers, in the multilayer stack. The concept of three-dimensional magnetic recording was contemplated during Dr. Sakhrat Khizroev's involvement in the study of perpendicular magnetic recording at Seagate Research and IBM Almaden Research Center.

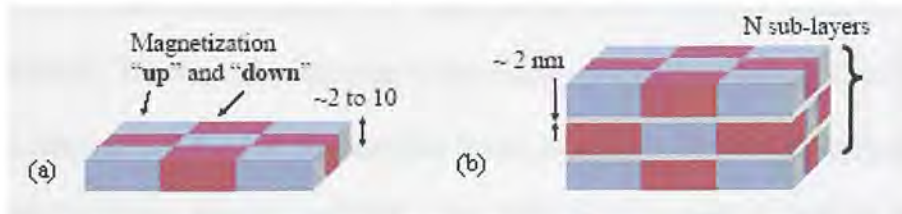


Figure 10: Diagram showing (a) perpendicular media and (b) 3-D magnetic media [8]

### 3.1 Perpendicular Anisotropy

Perpendicular anisotropy can be obtained by either the quantum mechanical interactions at the interface boundaries in multilayers, or the crystalline anisotropy [9]. Multilayers present positive uniaxial anisotropy when the magnetic layer thicknesses are reduced to a few monolayers [10]. The quantum mechanical interactions of interfacial surface anisotropy is a consequence of surface atoms located in a different environment than where bulk atoms would be situated in. Interfacial surface anisotropy has been shown to originate from single-ion mechanism, dipole-dipole interaction, and surface roughness [11].

The perpendicular anisotropy energy  $K_U$  can be generally expressed mathematically in Equation 22 by the shape and crystalline contribution to the magnetic anisotropy constant  $K_V$ , the interface energy  $K_S$ , resulting from broken symmetry of interface atoms known as Néel's surface anisotropy, and the thickness  $t$  of the magnetic layer, where smaller thicknesses promotes higher perpendicular anisotropy energy [10].

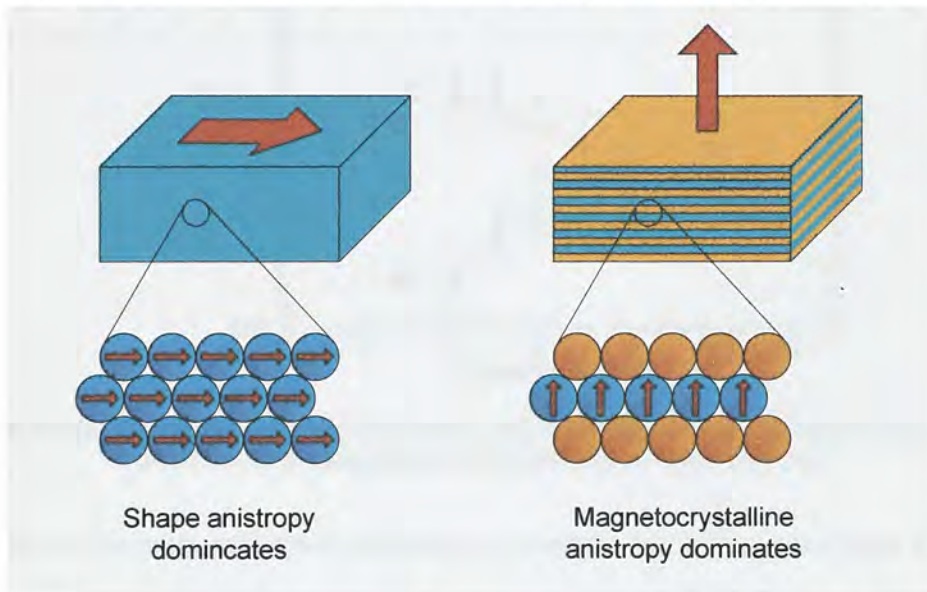
$$K_U = K_V + 2K_S / t \quad (22)$$

Another mathematical model for the perpendicular anisotropy energy has also been formulated. The dependence of the perpendicular anisotropy energy due to the orientation of magnetization of the magnetic layers is shown. This mathematical model, as expressed in Equation 23, describes the perpendicular anisotropy energy as a function of volume  $V$ , area  $S$ , the angle  $\theta$  between the magnetization  $M$  and the normal to the plane, and  $K_V$  and  $K_S$  are bulk (volume) and surface constants, respectively [11].

$$K_U = [V (K_V - 2\pi M^2) + 2 S K_S] \sin^2 \theta \quad (23)$$

Shape anisotropy has a tendency to resist orientation of perpendicular to the plane. The shape anisotropy arises from dipolar coupling of atomic moments.

Alignment of the moments, the basis of shape anisotropy, favors orientation along the largest extent of the sample, parallel to the plane for magnetic media. The effect of shape anisotropy is unfavorable for magnetic recording as seen in Figure 11; however, it is reduced as the thickness of the layer is decreased from bulk thickness to monolayers and considerably less than the interfacial surface anisotropy exhibited by multilayers.



**Figure 11: Shape anisotropy and crystalline anisotropy due to thickness**

Interfacial surface anisotropy is originated from thin magnetic layers bounded on both ends. Multilayers effectively exhibit the presence of interfacial surface anisotropy due to the extremely thin magnetic layers of approximately 0.2 nm to 1 nm, roughly one to five monolayers. At these thin layers, interfacial surface anisotropy and magnetocrystalline anisotropy, both oriented perpendicular to the plane, exceed the parallel aligned surface anisotropy, shown in Figure 12a. As the thickness of the magnetic layer is increased, surface anisotropy begins to dominate, shown in Figure 12b.

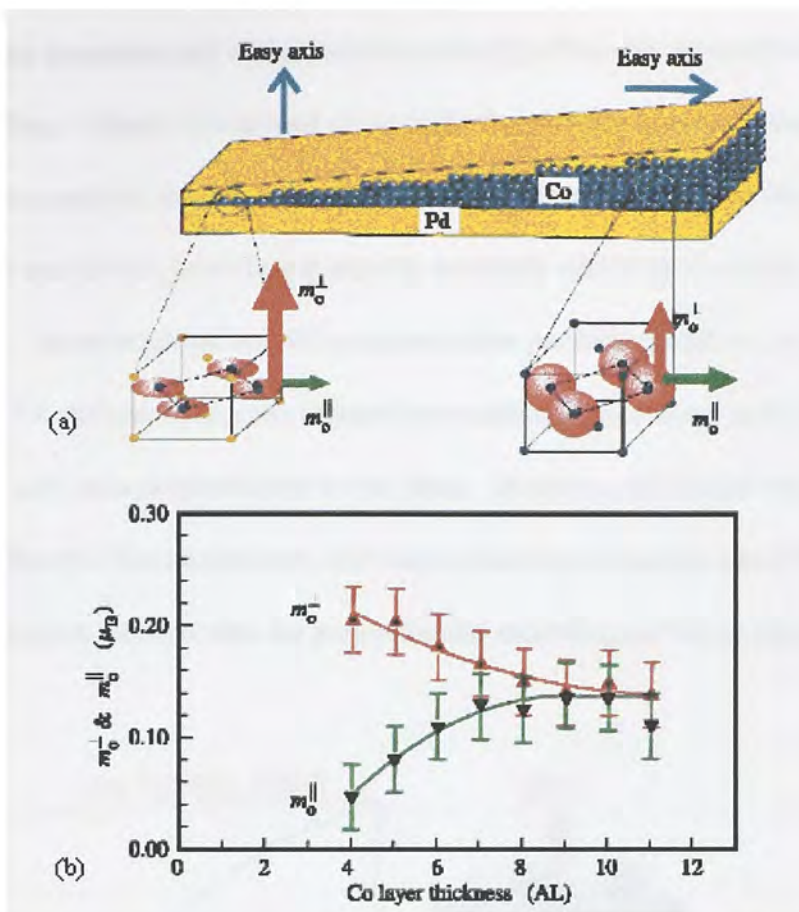
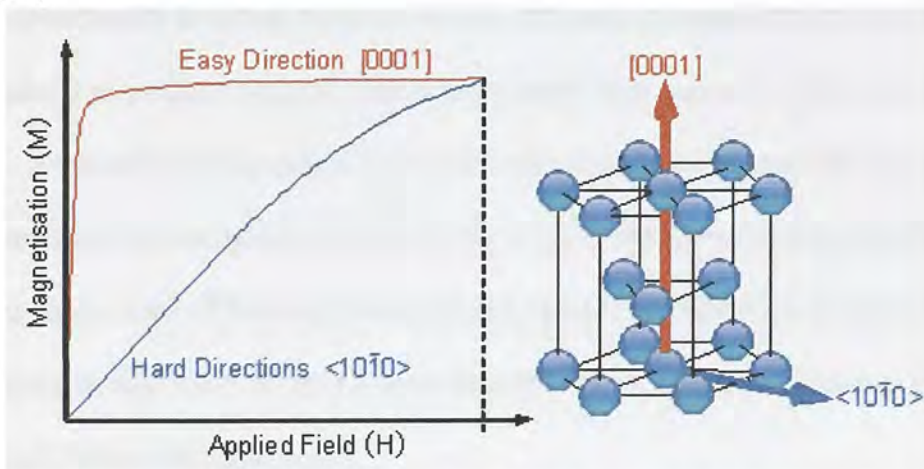


Figure 12: (a) Interfacial and crystalline anisotropy orienting the easy axis and (b) thickness dependence of perpendicular anisotropy due to anisotropy [12]

One of the more influential parameters on interfacial surface anisotropy is the surface roughness between two different layers. Surface roughness strongly influences the magnetization and hysteresis on magnetic thin films. Surface steps tend to induce an in-plane uniaxial magnetic anisotropy, with an easy axis parallel to the step direction [13]. The dependence of perpendicular anisotropy on surface roughness becomes more prevalent at monolayers, identified by larger surface-to-volume ratios. The surface-to-volume ratio corresponds to the thin magnetic layers applied in multilayers, where the diameter of a cobalt and palladium atom is approximately 0.22 nm and 0.28 nm, respectively.



Crystalline structures and orientation dramatically affect the perpendicular anisotropy of a film. Cobalt's hexagonal close packed crystalline structure promotes the exploitation of this material due to its beneficial inherent perpendicular anisotropy compared to iron and nickel, other ferromagnetic materials which form a cubic crystalline structure instead. An example of cobalt hexagonal close packed crystalline structure is shown in Figure 13, demonstrating the induced perpendicular anisotropy generated by an alignment of the easy axis perpendicular to the plane. However, for thicker layers of cobalt, on the order of a few nanometers, the shape anisotropy dominates and favors an in-plane magnetization, unfavorable for perpendicular recording and three-dimensional media [14].



**Figure 13: Perpendicular anisotropy due to cobalt hexagonal closed packed structure**

### 3.2 Physics of Three-Dimensional Media

Two different modes of 3-D recording have been investigated regarding the addressing of individual magnetic layers, referred to as multi-level 3-D and absolute 3-D modes. In the multi-level 3-D mode, a 3-D space is occupied for recording; however, its degree of utilization is determined by the instrument for data access during reading and writing procedures, rendering it as a non-effective technique [8]. In multi-level 3-D mode, when the signal recorded or read from a cell stack is defined by a recording transducer located above the stack, the information recorded in all  $N$  layers of the cell contribute to each signal level as shown in Figure 14a [8]. The number of signal levels  $L$  may be considerably less than the total number of layers, determined by the capability of the transducer to produce a signal with an adequately large signal-to-noise ratio (SNR) for the  $L$  levels to be distinguished from each other during reading and writing, where the areal density would increase by a factor of  $\log_2 L$  [8]. When operating in absolute 3-D recording mode, each  $n^{\text{th}}$  layer may be accessed separately as shown in Figure 14b. The areal density in absolute 3-D recording mode increases by a factor of  $N$  layers, providing much larger total areal densities [8]

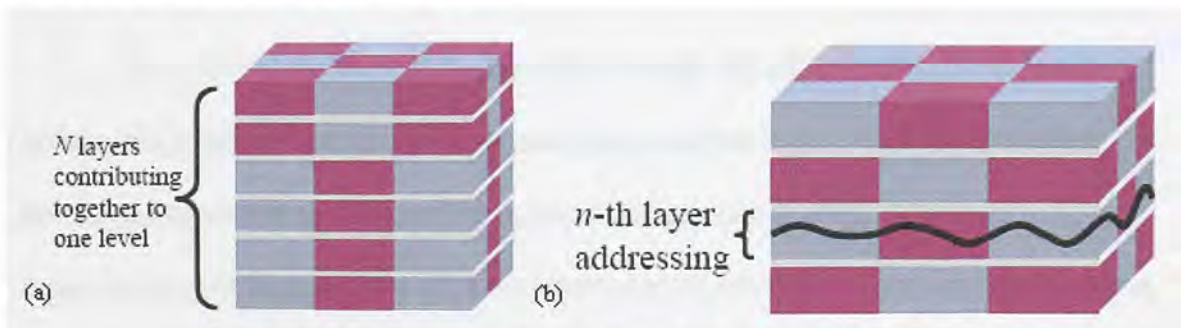
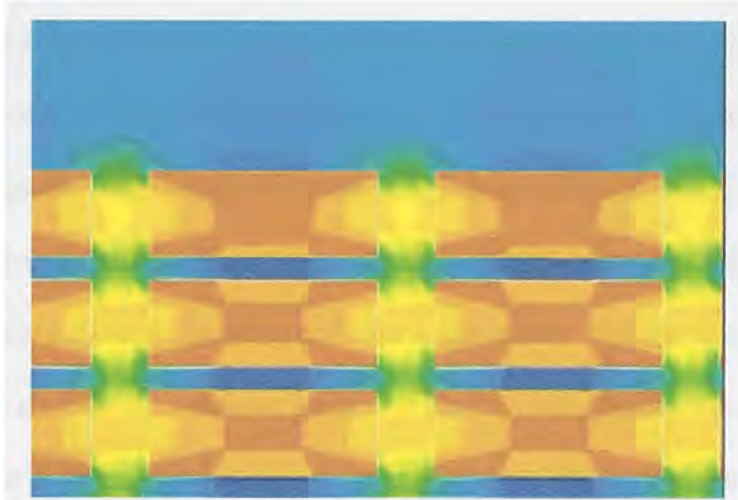


Figure 14: (a) 3-D multi-level and (b) 3-D absolute recording modes [8]

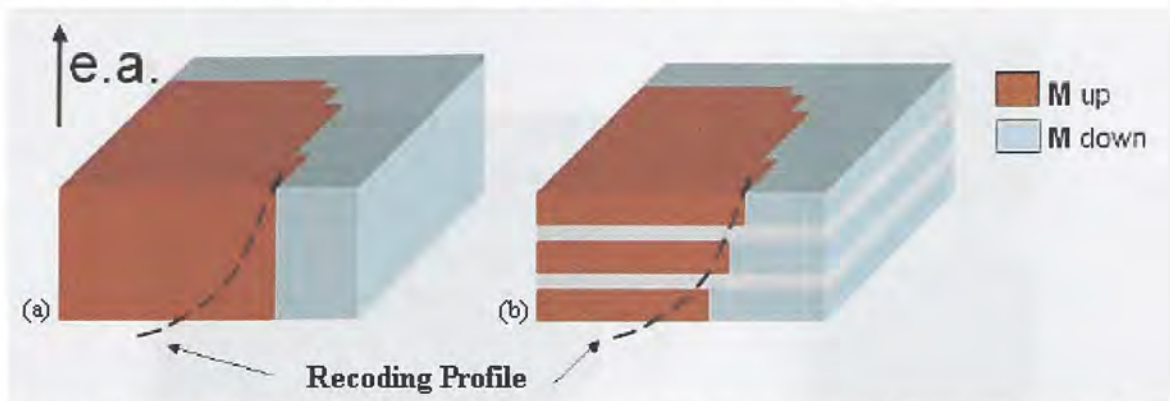
Three-dimensional media is fabricated as a stack of magnetic layers separated from each other by thin non-magnetic interlayers. Within the stack, each magnetic layer and non-magnetic interlayer is approximately 5~10 and 1~2 nm thick, respectively, where high surface-induced perpendicular anisotropy materials are vital in generating this effect, typically cobalt/platinum or cobalt/palladium multilayers. The difference between the multilayers exploited for 3-D recording and the multilayers used for perpendicular recording is that for 3-D recording, the significance of the non-magnetic interlayers is to break the exchange coupling between adjacent magnetic layers, illustrated through simulations on Figure 15.



**Figure 15: Magnetic layers exchange decoupled by non-magnetic layers**

The effect of the decoupling between the magnetic layers results in magnetic layers, independently manipulated for recording, whereas in perpendicular recording, the non-magnetic recording does not break the exchange coupling [8]. Therefore, magnetization of the magnetic adjacent layers may be oriented in opposite directions due to the lack of exchange coupling between the magnetic layers. Alternatively, if a thinner non-magnetic interlayer was implemented, the exchange coupling would be sufficient to

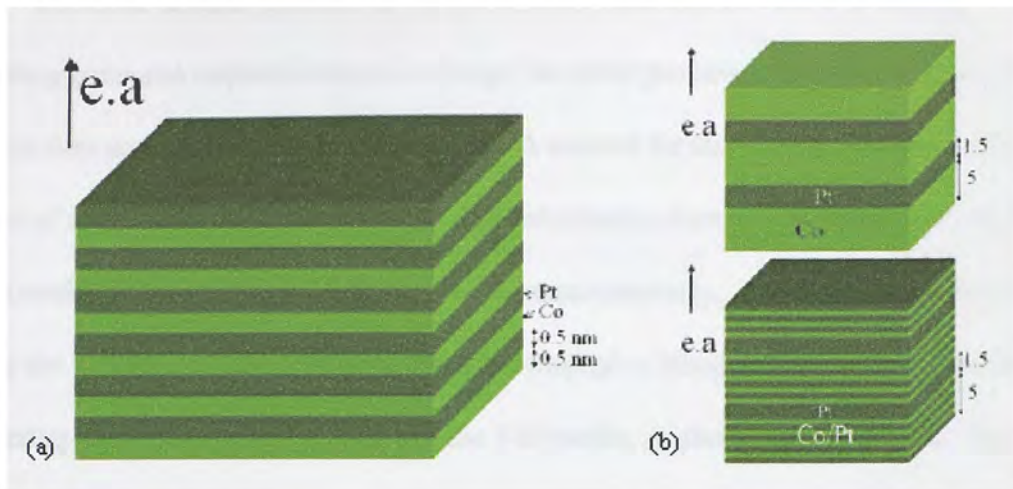
orient all the magnetic layers within a cell in the same direction, traditionally applied to perpendicular recording, illustrated in Figure 16a and Figure 16b [8].



**Figure 16: Simulations of effect of interlayer thickness where (a) the magnetic layers are coupled and (b) the magnetic layers are decoupled [8]**

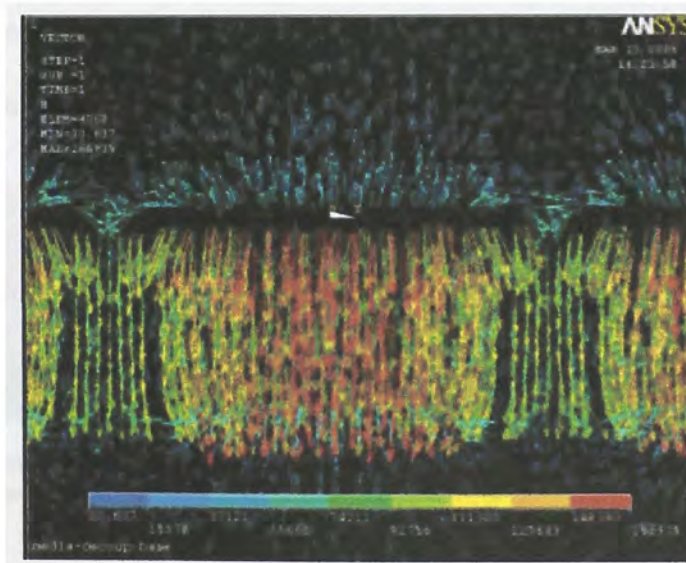
Thinner multilayers may also be utilized as a single magnetic layer comparable to the single layer of the magnetic layer in a cell of 3-D multilayers. Within a stack of multilayers, adjacent single magnetic layers (a high perpendicular anisotropic material or a composite of cobalt/palladium multilayers) are divided by relatively thick palladium layers to break the exchange coupling between single layers. Each single layer may consist of either an absolute magnetic layer or a stack of cobalt/palladium multilayers behaving similar to the absolute magnetic layer, shown in Figure 17a and Figure 17b. However, when realizing the case where only cobalt is used for magnetic layers, surface effects are minimized if the non-magnetic interlayers are sufficiently thick. The outcome is that magnetic anisotropy is determined by crystalline and shape anisotropy, where magnetization may be randomly oriented in-plane instead of perpendicular to the plane. Alternately, cobalt/palladium multilayers have relatively small palladium interlayers, less than roughly 1 nm, providing sufficient exchange coupling between the adjacent cobalt layers and creating strong surface-dominated perpendicular anisotropy.

Cobalt<sub>70</sub>Chromium<sub>18</sub>Platinum<sub>12</sub> (Co<sub>70</sub>Cr<sub>18</sub>Pt<sub>12</sub>) alloy is an additional alternative for magnetic layer implementation due to its higher perpendicular anisotropy.



**Figure 17: (a) Co/Pt stack for perpendicular recording and (b) 3-D multilayers Co (top) used as a magnetic layer and Co/Pt (bottom) thin layers that constitutes a single magnetic layer [8]**

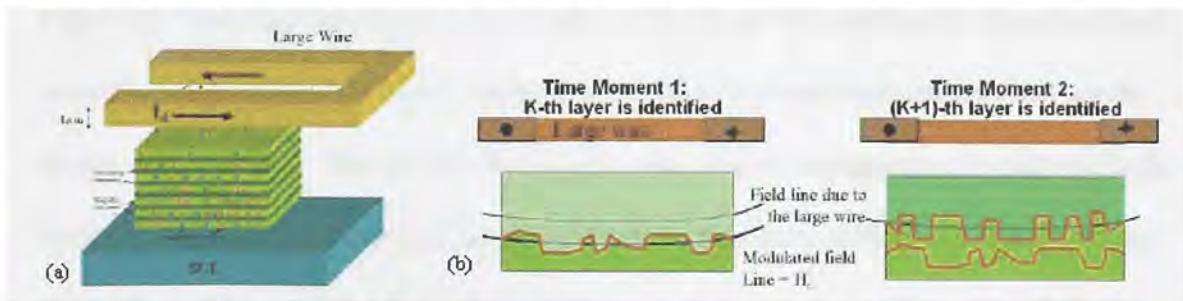
Due to perpendicular anisotropy, demagnetization fields are oriented normal to the plane, where demagnetization fields are dramatically reduced, shown in Figure 18. The demagnetization field of perpendicular media exhibits lower values compared to longitudinal media, broadening the magnetic transitions in longitudinal media [15].



**Figure 18: Simulation of demagnetization field within a perpendicular magnetic layer**

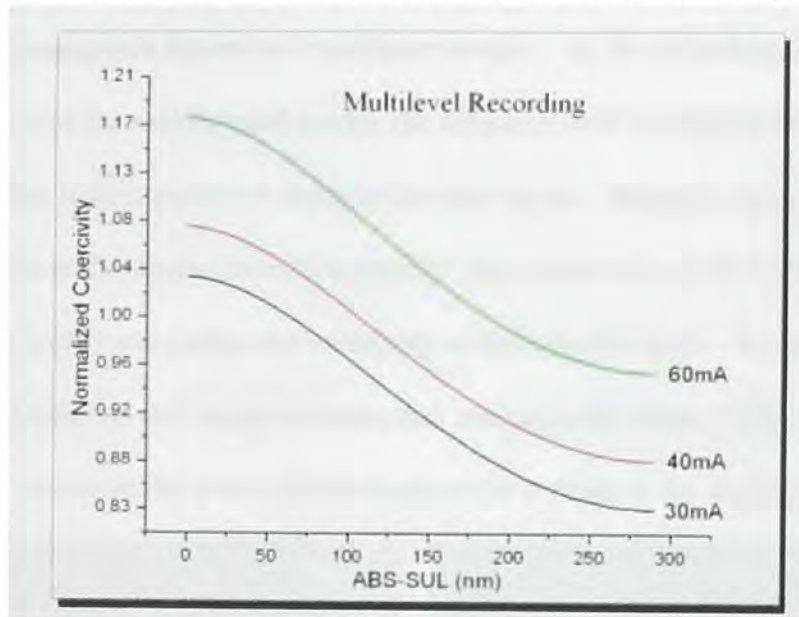
### 3.3 Writing on Three-Dimensional Media

There are several potential methods to write information onto 3-D media, consisting potential implementation to forego the write process is through magnetically induced data access using a variable current. A control for the writing process could consist of a grid of crossing word lines. The information from a horizontal layer on the media could be essentially recorded and read instantaneously. To identify each layer during the writing process, a current is guided through a biasing wire on top of the media, generating a large bias perpendicular to the 3-D media, as shown in Figure 19a. The biasing field may be modified by varying the current in the wire. Recording is processed sequentially, where the current is sufficient to produce a large field relative to the coercivity of the bottom layer, illustrated in Figure 19b [8]. In succession, current through the word lines is generated to manipulate the field in the layer, essentially recording the field pattern generated onto the bottom layer [8]. Afterwards, the current in the large wire is reduced and reversed to identify the next layer above, where another set of signals is guided through the word lines and recorded onto that layer [8]. This process is repeated sequentially until the top layer is reached.



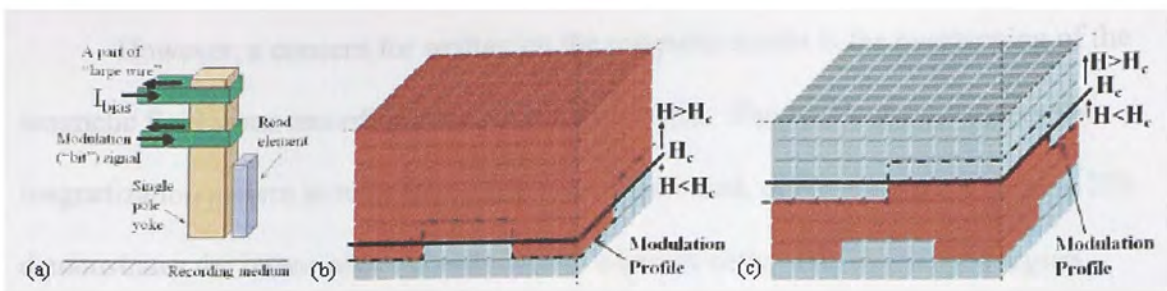
**Figure 19: (a) Identification of layers during writing and (b) cross-sectional diagrams showing two time moments where field due to the biasing wire is used to identify layers [8]**

The variation of the current to effectively write on different levels within a multilayer is exemplified in Figure 20. The coercivity in the diagram is normalized to 1.00, signifying the coercivity for that magnetic layer, demonstrated in the diagram that sufficient effective field, or correspondingly the current, to record on any layer must be over the coercivity of that layer. The simulation shows that larger current, correlating to higher fields, is necessary to overcome the coercivity field of a layer deep into the media.



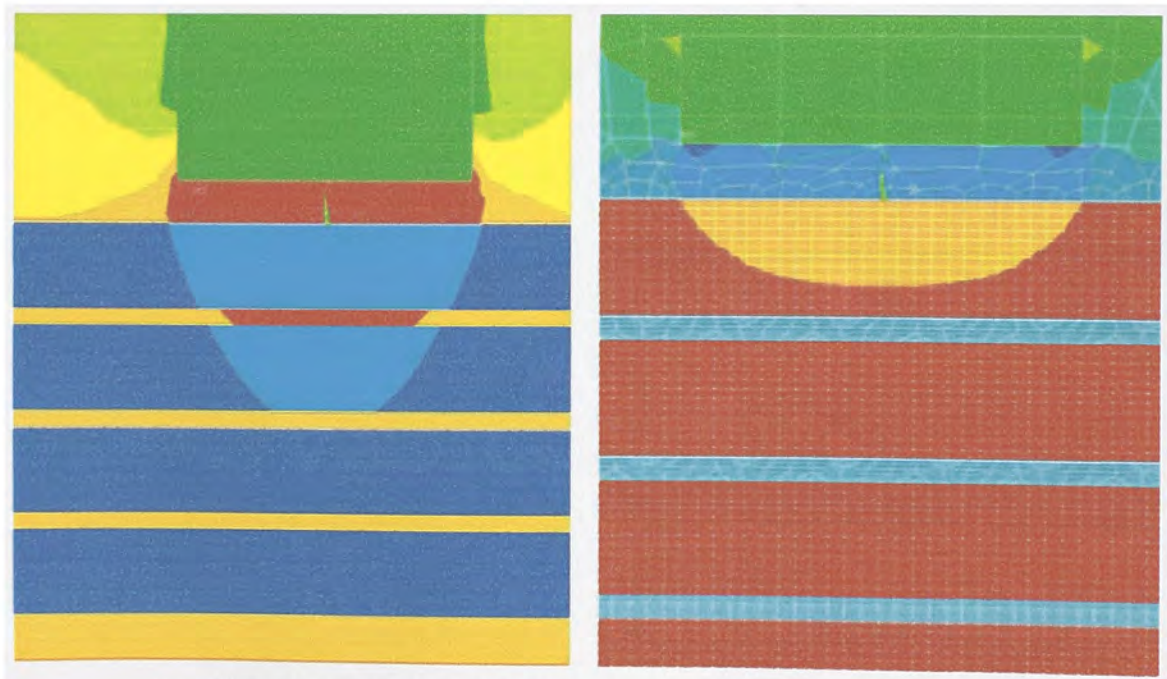
**Figure 20: Multilevel recording through variation of write current**

A diagram of a single grid structure located above the media is displayed in Figure 21. The diagram consists of a section of the large wire and the bit signal wrapped around a rod composed of a soft magnetic material with a read element attached nearby shown in Figure 21a. The rod acts as a single pole head as implemented in perpendicular recording [8]. Two instances of the magnetization allocation, during the writing process in a section of the media, where the distribution is deep into the media and partially into the media, displayed in Figure 15b and Figure 15c, respectively.



**Figure 21: (a) Single grid structure and (b) magnetization near (c) and far from the bottom layer [8]**

Figure 22 illustrates the effective magnetic fields penetrating through the magnetic layers and non-magnetic layers in a multilayer sample. As the recording field is applied to all the levels of the multilayered media, the effective field in sequentially lower layers decreases as the field is analyzed closer to the base layers. Magnetic layers, from the air bearing surface of the media down to a specific layer accessed, are all written on when the recording profile overcomes the coercivity of that specific layer. It is exemplified through the simulation that larger currents, and consequently larger fields, are necessary to efficiently record on the lower layers closer to the bottom of the multilayered sample.



**Figure 22: Field penetrating through multilayers during recording**



However, a concern for writing on the magnetic media is the overlapping of the magnetic field when recording onto adjacent bits cells. Figure 23a demonstrates the magnetization pattern in recording process on a saturated, or erased, media. Figure 23b demonstrates the issues when recording onto adjacent cells. The overlapped region defines the region where the information is ineffective. The overlapped region may be considered ineffective because the region may have remanence magnetization from either of the two adjacent bit cells.

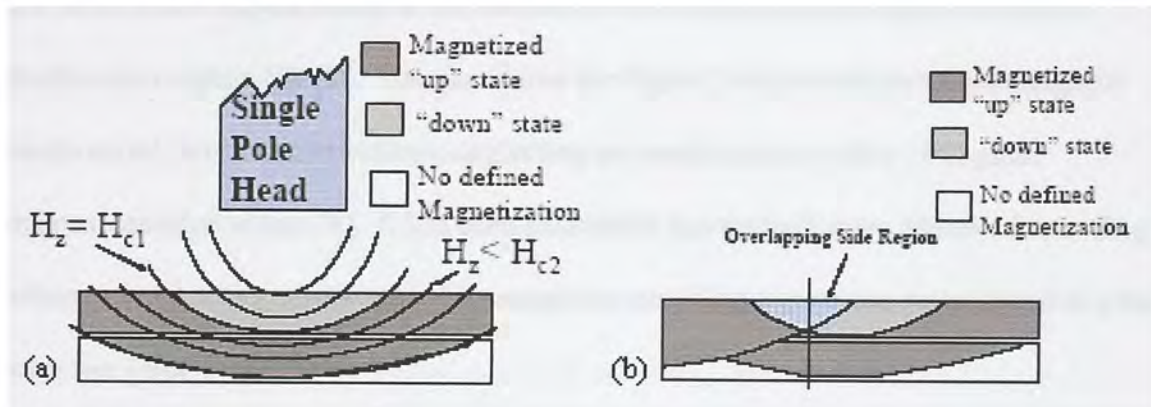


Figure 23: Recording on (a) an erased media (b) and on previously recorded adjacent cells [8]

### 3.4 Reading on Three-Dimensional Media

The most conceptual implementation to reading from 3-D magnetic media is direct reading of the magnetic field from above. A giant magnetoresistive (GMR) sensor could be utilized to read the magnetic signal emitting from the media in each bit cell. The state of the individual layers can be determined by analyzing the net magnetic field for different magnetization patterns, illustrated in Figure 24a [8]. The calculated signal levels decreases exponentially as the number of recording magnetic layers increases, displayed in Figure 24b [8]. The simulation for Figure 24b assumes patterned magnetic media on all three axial directions, neglecting any media noise, with a  $10 \Omega$  giant magnetoresistive sensor [8]. It has been postulated that through more advanced encoding schemes, a 10 dB signal-to-noise ratio magnetic recording system can be analyzed at a bit error rate (BER) of  $10^{-9}$  [8].

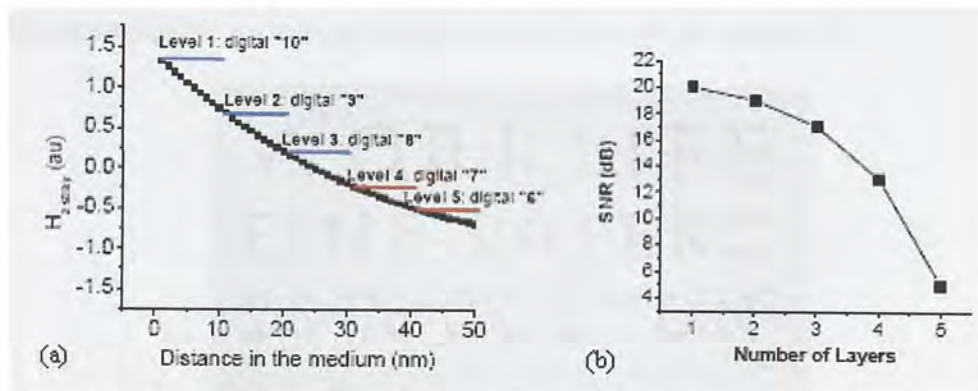
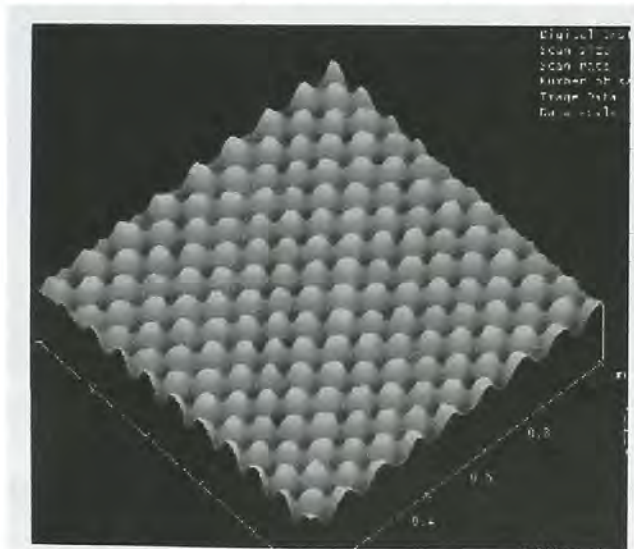


Figure 24: (a) Stray field versus digital level (b) and signal-to-noise ratio versus number of layers [8]

### 3.5 Patterned Media

A viable approach to extending the superparamagnetic limit past its current bound for perpendicular and three-dimensional media is the patterning of the magnetic media, shown in Figure 25. Patterned media enhances the thermal activation volume, increasing the ratio which determines stability in a grain [7]. Patterning of the media decreases the exchange coupling between adjacent grains, forcing the patterned bit to behave similar to single domain [7]. Additionally, maximizing the bit-to-bit spacing in patterned media for a given areal density assists minimization of influence of neighboring bits, enabling higher efficiency write poles, and maximizing readback resolution [7]. It has also been demonstrated through past simulations that recording on patterned media allows thicker magnetic layers, important for the implementation of three-dimensional media, where the magnetic spacing between the write pole and the recording layer is always in need for minimizing so that the recording field penetrates through the media [7].



**Figure 25: Patterned media with island diameter of 50 nm by focused ion beam [8]**

### 3.6 Patterned Soft Underlayer

A perpendicular recording system includes a single pole recording head and magnetic media that consist of an upper recording layer and a soft magnetic underlayer, as seen in Figure 26a without the soft magnetic underlayer and in Figure 26b with one. The single pole head is a modification of the common ring head, utilized in longitudinal recording, consisting of a wider gap between the leading pole and the trailing pole trimmed down to 50 nm by a focused ion beam [16]. The purpose of the soft underlayer is to enhance the perpendicular component of the recording field by allowing the magnetic flux to flow back from the leading pole to the trailing pole, where the recording takes place [17]. This effect closes the magnetic loop, head similar to fundamental electronics, where the soft underlayer is described as a mirror effect to the real head, essentially doubling the flux through the recording field [17].

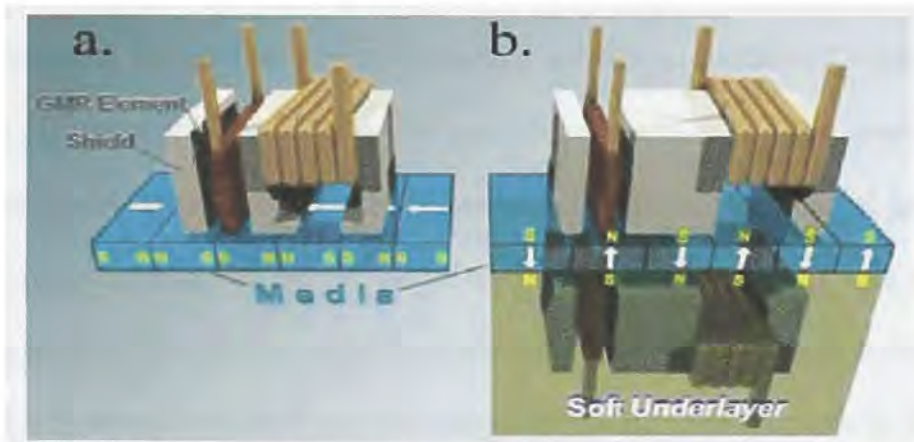
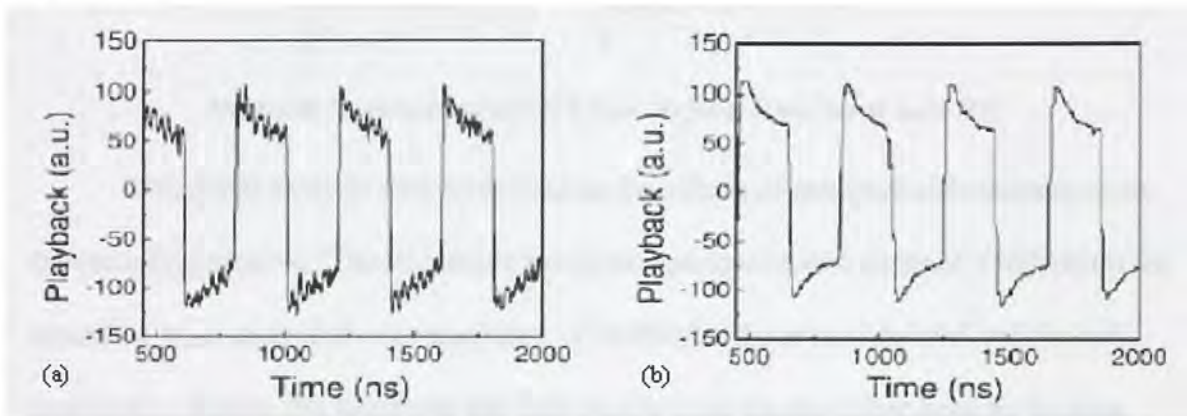


Figure 26: (a) Longitudinal (b) and perpendicular recording with soft underlayer [17]

Soft under layer increases the effective recording field, however, it is also accountable for several performance limiting issues. One issue is the readback signal noise, caused by the free magnetic domain wall movement resulting in magnetic stray

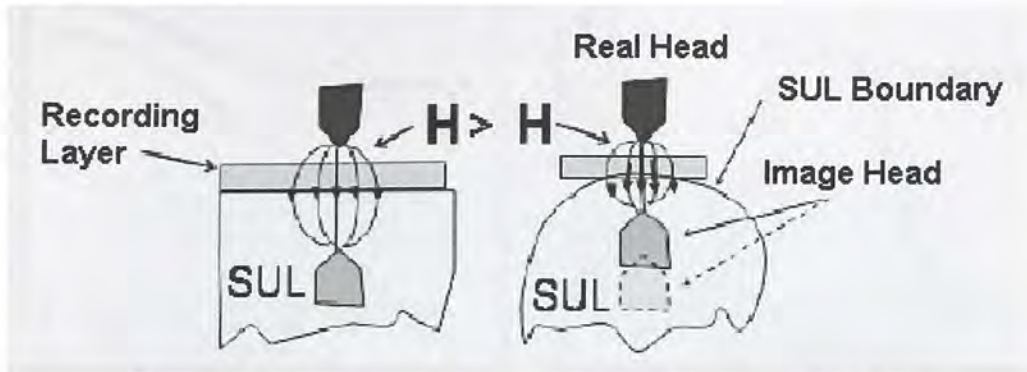
fields apparent as random high frequency noise in the giant magnetoresistive [17]. Nevertheless, the reduction of the noise level was radically reduced when biased, as shown in Figure 27a and Figure 27b, an experimental result accomplished through a Guzik Spinstand [18]. Biasing is accomplished by introducing a constant small magnetic field sufficient to pin the domain walls in place, possibly synchronized within the read cycle [18].



**Figure 27: (a) Noise due to movement of domain walls (b) and reduction of noise with biasing [18]**

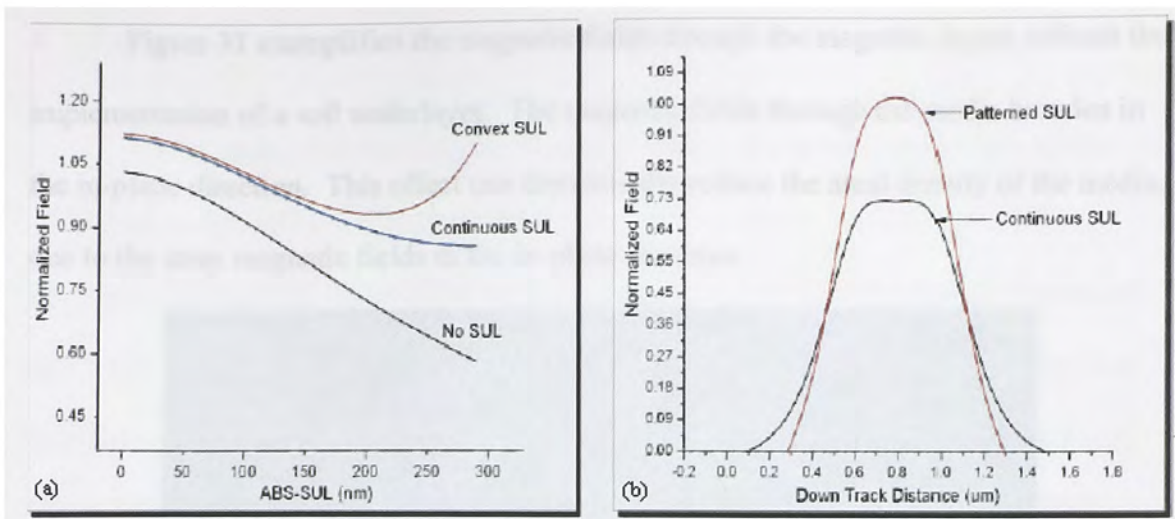
Patterning the soft underlayer is a practical solution to overcome several of the concerns with the application of soft underlayer. In one instance, the continuous soft underlayer would ideally create the perfect mirror image of the real recording head; however, since the magnetic layer is located directly above the soft underlayer, the mirroring effect is reduced, known as the spacing loss [17]. The geometrical shape of the patterned soft underlayer affects the field magnitude and the field dynamics in the recording process [19]. A convex pattern, similar to optical lenses, can be implemented to shift the imaged head closer to the recording layer, by essentially directing the focal point near the recording layer, diminishing spacing losses, as illustrated in Figure 28 [19]. The focusing of the imaged head also provides the effect of increasing the resolution of

the recording layer by converging the magnetic field to a smaller area, allowing for greater areal densities.



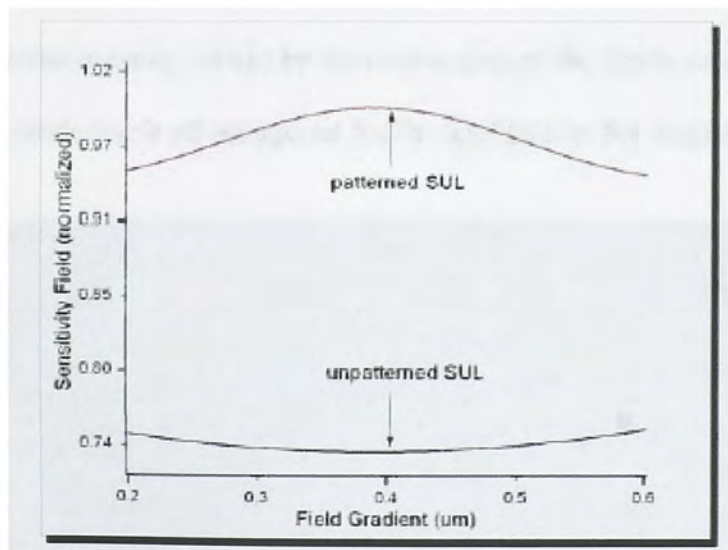
**Figure 28: Convex patterned soft under layer to move image head [19]**

Numerical analysis was performed on the effects of patterned soft underlayer on the recording process. The simulation performed assumes a coercivity of 3500 Oe for the recording layer and relative permeability of 10,000 for the recording head and the soft underlayer. Figure 29a illustrates the field profile from the recording head air-bearing surface (ABS), through the cross-section of the media, down to the soft underlayer. The simulation shows an increase in the field due to the soft underlayer. Additionally, the simulation also demonstrates consistent larger recording fields throughout the media, larger than the coercivity of the media, and double the field of the simulation without a soft underlayer at the soft underlayer-magnetic media interface. Figure 29b exemplifies the magnetic field for the convex patterned and continuous soft underlayer in the direction along the track. The simulation clearly indicates that the convex patterned soft underlayer generates a larger field and exhibits steeper fallout, favorable for smaller bit sizes.



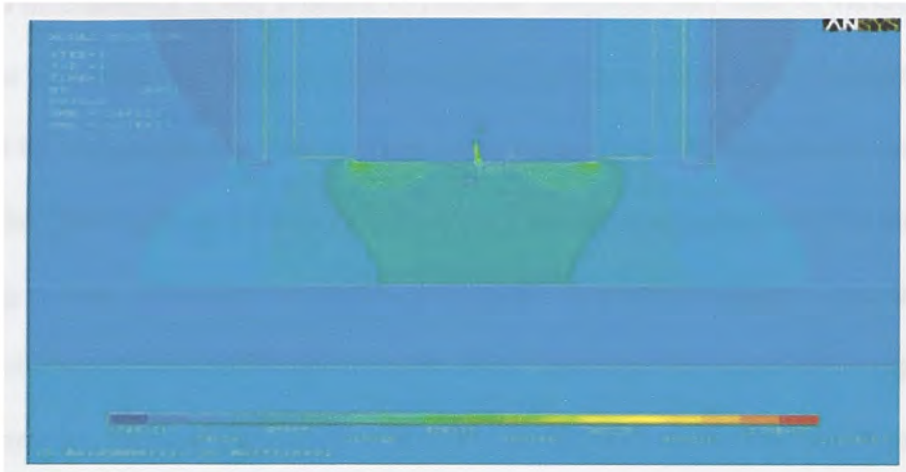
**Figure 29: (a) Effect of soft underlayer through the media (b) and field gradients along the track**

The application of soft underlayer is also an essential part of both the read and write process. According to the reciprocity principle, the readback sensitivity field is enhanced by the assistance of a soft underlayer [20]. An increase in over 35% of the sensitivity field of patterned soft underlayer, compared to unpatterned soft underlay, is shown in Figure 30.



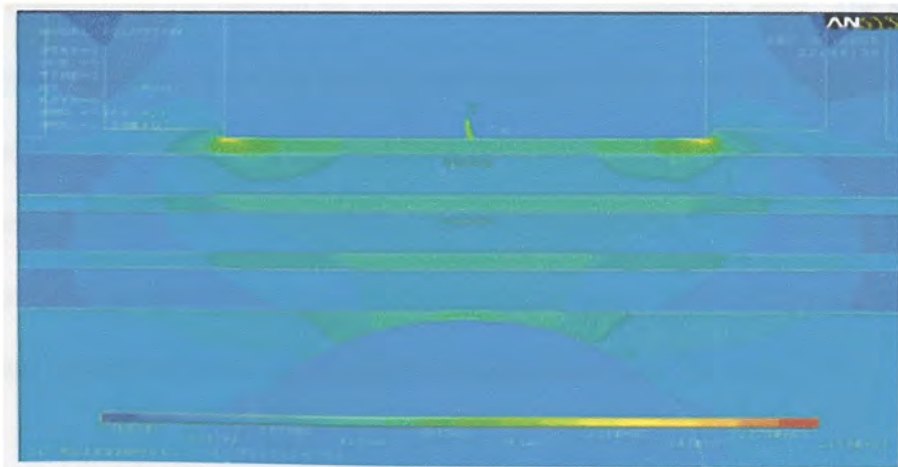
**Figure 30: Effect of patterned soft underlayer on readback sensitivity**

Figure 31 exemplifies the magnetic fields through the magnetic layers without the implementation of a soft underlayer. The magnetic fields through the media broaden in the in-plane direction. This effect can dramatically reduce the areal density of the media, due to the stray magnetic fields in the in-plane direction.



**Figure 31: Fields through magnetic layers without a soft underlayer**

Figure 32 illustrates the magnetic fields through the magnetic layers with the implementation of a convex patterned soft underlayer. The effect of the convex geometrical patterns is easily visible by the converging of the fields, caused by the convex pattern, rendering it advantageous for the applications for magnetic media.



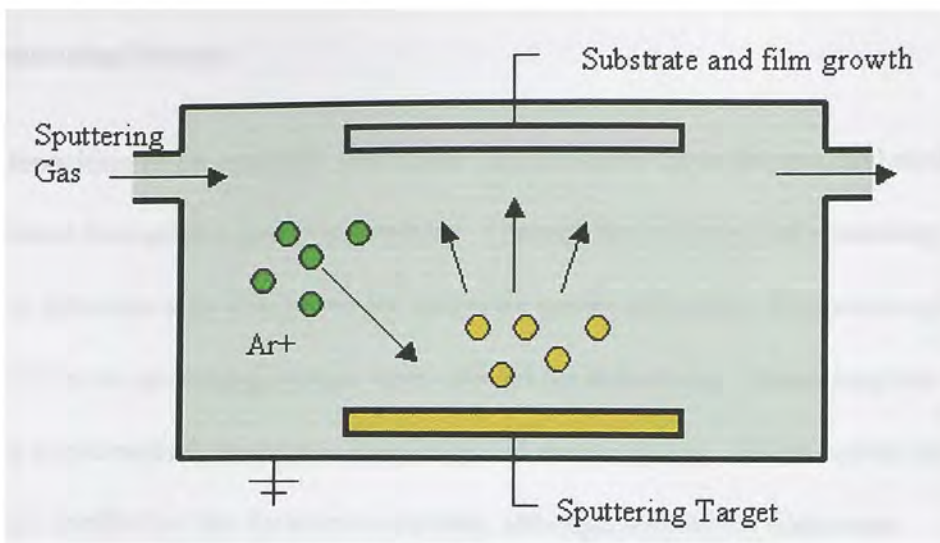
**Figure 32: Fields through magnetic layers with convex patterned soft underlayer**



#### 4. FABRICATION OF THREE-DIMENSIONAL MEDIA

The fabrication of the three-dimensional media was accomplished through the utilization of the sputtering system and the focused ion beam. With the aid of these advanced mechanisms, it was possible to fabricate magnetic thin films of various metals of a range of thicknesses. High precision etching, at scales of ten's of nanometers, was produced by the technique commonly known as ion milling with the focused ion beam.

The fabrication of the three-dimensional memory was grown with the aid of a sputtering system. Thin film deposition through the sputtering system is done by an ejection of atoms from a solid surface, commonly known as the target, by energetic atomic particles within a vacuum as seen in Figure 33. The sputtering system employed consisted of energetic atomic particles coming from ionized Argon gas plasma. The plasma is generated by direct current (DC) or radio frequency (RF) glow discharges of a noble gas. The atoms ejected are then transferred from the source to the sample, depositing the desired alloy onto the sample. Sputtering is largely driven by momentum exchange between the ions and atoms in the material due to collisions. Sputter guns are typically magnetrons that depend on a strong electric and magnetic field. The sputtering process can be disrupted by other electric and magnetic fields near the target. Additionally, small magnetic fields may leak from ferromagnetic targets, resulting in sputter guns typically including strong permanent magnets for compensation. However, the charge build-up can be avoided by the implementation of radio frequency power sources and a matching network to match the impedance onto the load.



**Figure 33: Deposition through a sputtering system [3]**

The focused ion beam is an instrument utilized for several operations. The focused ion beam employs a focused beam of gallium ions. Gallium is chosen because it is simple to build a gallium liquid metal ion source (LMIS). In a gallium liquid metal ion source, the gallium metal is placed in contact with a tungsten needle and heated. Gallium liquefies the tungsten tip, causing a substantially large electric field, greater than  $10^8$  V/cm, to ionize and emit the gallium atoms [3]. The gallium atoms are accelerated to a high energy, approximately 10 keV - 40 keV, and then focused onto the sample by electrostatic lenses [3]. Focused ion beams can image the sample with a spot size on the order of a few nanometers. The manipulation of the current in the focused ion beam may be utilized to etch a small region of a few nanometers with high precision.

## 4.1 Sputtering Process

Deposition of all materials within the fabrication of three-dimensional media was accomplished through the sputtering system. Through the technique of sputtering, it was possible to fabricate very thin layers for magnetic media utilization. Magnetron sputtering sources within the sputtering system were utilized for deposition. Power supplies for sputtering implemented were radio frequency and direct current. Direct current power supplies are ineffective for dielectric materials, although only metal films were fabricated.

Cleansing of silicon wafers before deposition was important for film quality. Cleansing of the wafers involved the processes of normal cleansing, organic cleansing, and oxide cleansing. Deionized water and nitrogen was used to wipe the chemicals and any contaminants before and after every cleansing process and to dry the surface of the wafer, respectively. The chemical solution of 1:5 hydrogen peroxide  $H_2O_2$  and 49% concentrated sulfuric acid ( $H_2SO_4$ ), commonly known as piranha, for metal contaminants and organics was used for the organic cleansing. Organic cleansing removes contaminants such as dust and grease from the silicon surface. Finally, to remove the oxide layer on top, which is formed on the surface by contamination of the metal from air, the wafer is submerged in a 10:1 deionized water and hydrofluoric acid (HF) for ten seconds.

Removal of particles was achieved through the cleansing of the chamber by inducing a low base pressure before the sputtering process. Most importantly, very low base pressures causes water vapor and other organics to degas, decontaminating the

chamber for proper deposition. Base pressures of  $1.0 \times 10^{-6}$  Torr or lower were applied for all experimentations. Flow of argon gas into the chamber was regulated and kept constant throughout most experiments at an appropriate rate of 20 standard cubic centimeters per minute (sccm), the recommended rate for the sputtering system utilized. Additionally, before base pressure was reached by the chamber, 20 sccm of argon gas was flowed into the chamber for 20 minutes by the three sources on the mass flow controller (MFC). The purpose of this procedure was to further decontaminate the chamber by allowing the heavy argon ions to collide with the substrate holder and the chamber walls, removing contaminants that may still have been situated in those areas. Process pressures for suitable deposition in the sputtering system range from approximately 2 mTorr to 10 mTorr. Higher processing pressures lead towards lower rates; however, it also introduces the effect of raising the number of unwanted atoms deposited into the sample. This effect, which may be evident for pressures as low as 10 mTorr, resulted in a process pressure of 5 mTorr implemented for most processes.

The temperature of the sample is also a controlled parameter which was manipulated depending on the desired effect. Higher temperatures inside the chamber before sputtering allow for contaminants to move around and become susceptible to the force of the turbo pump due to the provided thermal energy supplied by the quartz lamp. Larger temperatures result in better uniformity and film quality, specifically crystallography and adhesion. Conversely, larger temperatures also effect the magnetization of the sample, given that it is undesirable to reach temperatures near the Curie temperature. Additionally, higher temperatures may also change the crystallographic structure of materials, an example shown by the transformation of cobalt

from hexagonal closed packed structure to face centered cubic structure at 722 K, unfavorable for three-dimensional media.

The rate of deposition is also immensely dependant on the power driven through the desired target. Larger power levels result in an increased in excited atoms, consequently a higher amount of atoms released from the target and onto the sample. Due to the required precision necessary to deposit thin layers with high accuracy, low deposition rates were implemented. Achievement of low deposition rates was realized by reducing the power driven through the target to its minimum level. However, to ensure proper deposition and uniformity throughout the sample, the power level was increased approximately 5 W above the threshold, for each different target correspondingly, to ignite plasma.

Once the previously mentioned process parameters were chosen, the main objective was to control the thickness of the deposition. Since the thickness of the sample is simply a linear dependence on time, with set parameters, thickness was predicted fairly accurately given that the set process parameters are known and the effect result of deposition rate from the combination of the set process parameters is known as well. Thicknesses deposited may vary between as thin as a few Angstroms to several microns; however, film quality becomes an issue at larger heights, due to stress forces and proper adhesion of the film.

The deposition rates, once all process parameters except time were made constant, were determined for the various materials used. Investigation on the deposited height of the material was achieved through step heights. Step heights were accomplished by covering a small section of the sample by either tape or marker. The outcome was a

section that does not incur deposition, from which the height between this area, and the section that was exposed to deposition, may be compared. The step heights were analyzed with the aid of an atomic force microscope, shown in Table 3, with corresponding process parameters. Through software tools for the atomic force microscope, step heights for two selected area, with and without exposure to deposition, were analyzed, the end result an average of the difference of heights between the two. Several samples were investigated to determine an average of each material and consequently the average deposition rate on the different materials.

<b>Metal</b>	<b>Power</b>	<b>Pressure</b>	<b>Flow</b>	<b>Source</b>	<b>Rate</b>
Chromium	60 W	10 mTorr	35 sccm	RF	0.349 nm/s
Cobalt <sub>10W</sub>	10 W	5 mTorr	20 sccm	RF	0.025 nm/s
Cobalt <sub>20W</sub>	20 W	10 mTorr	35 sccm	RF	0.050 nm/s
Cobalt <sub>35W</sub>	35 W	10 mTorr	35 sccm	RF	0.144 nm/s
Co <sub>70</sub> Cr <sub>18</sub> Pt <sub>12</sub>	20 W	5 mTorr	20 sccm	RF	0.010 nm/s
Palladium <sub>15W</sub>	15 W	5 mTorr	20 sccm	DC	0.222 nm/s
Palladium <sub>20W</sub>	20 W	10 mTorr	35 sccm	DC	0.221 nm/s
Palladium <sub>50W</sub>	50 W	10 mTorr	35 sccm	DC	0.481 nm/s
Permalloy	60 W	10 mTorr	35 sccm	RF	0.165 nm/s
Tantalum <sub>20W</sub>	20 W	5 mTorr	20 sccm	RF	0.047 nm/s
Tantalum <sub>35W</sub>	35 W	10 mTorr	35 sccm	RF	0.022 nm/s

**Table 3: Deposition rates established for different metals**

## 4.2 Deposition of Soft Magnetic Underlayer

Prior to the fabrication of the magnetic layers, the soft magnetic underlayer is deposited to take advantage of the several benefits it promotes. As mentioned before, permalloy is employed in three-dimensional media as a soft underlayer due to its exceptionally high relative permeability, approximately 8000 – 100,000. Several permalloy samples were fabricated to examine the effects of thickness of the soft underlayer, shown in Table 4. During the deposition process of the different samples for soft underlayer utilization, two magnets of opposite poles were facing each other, resulting in a field through the sample from one pole to the other. The magnetic field through the deposition process caused the domains to align and become oriented along the direction of the field. Alignment of the alternating domains in the permalloy samples makes it a potential candidate for high frequency applications, such as ultra fast recording and reading.

<b>Metal</b>	<b>Size</b>	<b>Power</b>	<b>Source</b>	<b>Flow</b>	<b>Pressure</b>	<b>Rate</b>	<b>Temperature</b>
Permalloy	40 nm	100 W	RF	20 sccm	10 mTorr	0.187 nm/s	24° C
Permalloy	80 nm	100 W	RF	20 sccm	10 mTorr	0.187 nm/s	24° C
Permalloy	110 nm	100 W	RF	20 sccm	10 mTorr	0.187 nm/s	24° C
Permalloy	230 nm	100 W	RF	20 sccm	5 mTorr	0.187 nm/s	100° C
Permalloy	300 nm	100 W	RF	20 sccm	10 mTorr	0.187 nm/s	100° C
Permalloy	400 nm	100 W	RF	20 sccm	10 mTorr	0.187 nm/s	100° C

**Table 4: Deposition parameters for different permalloy samples**

### 4.3 Focused Ion Beam for Patterning

Permalloy was etched through a process commonly known as ion milling employed by the focused ion beam. A pattern was generated containing a convex shape with 100 nm height and 100 nm island width within a 5  $\mu\text{m}$  by 5  $\mu\text{m}$  square. The pattern generated of 100 nm periodicity, shown in Figure 34 was fabricated to adequately demonstrate the advantageous effects of the pattern SUL with lower resolution. However, it is desirable for future demonstrations to decrease the thickness of the permalloy layer and the height of the convex shapes to approximately 30 nm or less. Additionally, it is also desirable to decrease the periodicity to the same dimensions as the height of the convex shapes, reducing spacing losses and increasing the resolution of the magnetic media, resulting in smaller bit sizes and larger areal density.

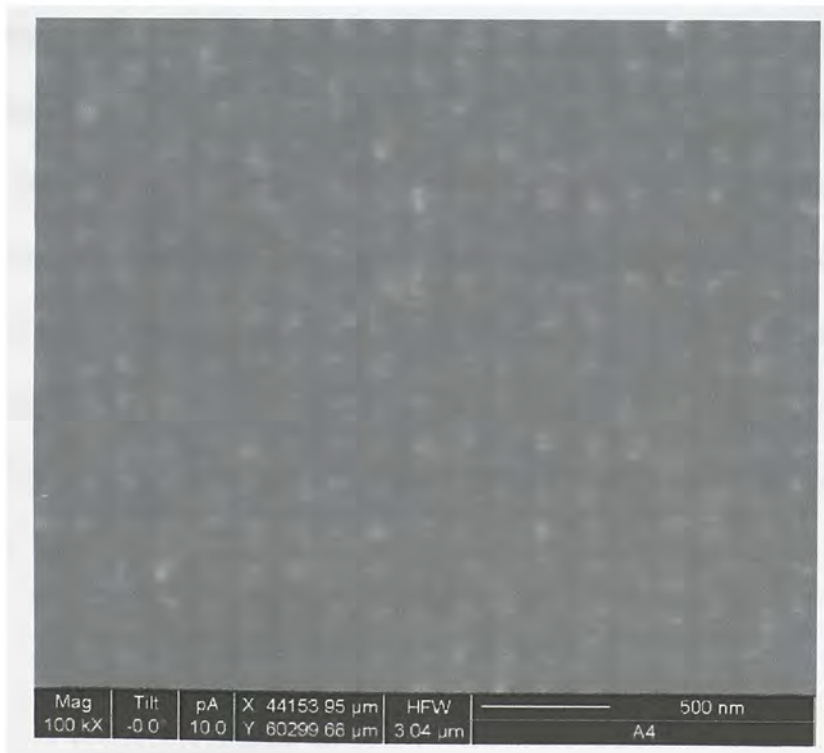


Figure 34: Image of patterned permalloy through the focused ion beam,



#### 4.4 Deposition of Magnetic Layers

The fabrication of the three-dimensional media was achieved through deposition of the metals of cobalt, palladium, tantalum, and the Cobalt<sub>70</sub>Chromium<sub>18</sub>Platinum<sub>12</sub> alloy by the sputtering system. Thin cobalt layers were deposited to attain the magnetic layers, in the multilayered samples, necessary for recording. Cobalt magnetic layers were varied to determine dependence of magnetic behaviors on the thickness. Palladium layers were fabricated to realize the nonmagnetic interlayers, sufficiently thin to yield strong exchange coupling between the cobalt layers. Palladium nonmagnetic layers were also altered to determine dependence of magnetic behaviors on the thickness. Tantalum was utilized as a seedlayer to help promote perpendicular anisotropy within the cobalt magnetic layers. Tantalum thicknesses for seedlayer implementation have been shown to display minimal effects on hysteresis of the magnetic layers above the tantalum seedlayer [21]. Cobalt<sub>70</sub>Chromium<sub>18</sub>Platinum<sub>12</sub> layers were deposited to realize the single magnetic layers. The dependence of magnetic behaviors on the thickness of the varying Cobalt<sub>70</sub>Chromium<sub>18</sub>Platinum<sub>12</sub> layers was also to be examined. The deposition parameters of all the metals utilized to fabricate three-dimensional media, including their different thicknesses for the several multilayer samples, are shown in Table 4. The parameters described for each specific layer ideally could be reproduced and yield the same effects.

<b>Metal</b>	<b>Size</b>	<b>Power</b>	<b>Source</b>	<b>Flow</b>	<b>Pressure</b>	<b>Rate</b>	<b>Time</b>
Cobalt	0.2 nm	10 W	RF	20 sccm	5 mTorr	0.025 nm/s	8 s
Cobalt	0.3 nm	10 W	RF	20 sccm	5 mTorr	0.025 nm/s	12 s
Cobalt	0.4 nm	10 W	RF	20 sccm	5 mTorr	0.025 nm/s	16 s
Cobalt	0.5 nm	10 W	RF	20 sccm	5 mTorr	0.025 nm/s	20 s
Cobalt	0.6 nm	10 W	RF	20 sccm	5 mTorr	0.025 nm/s	24 s
Co <sub>70</sub> Cr <sub>18</sub> Pt <sub>12</sub>	10 nm	20 W	RF	20 sccm	5 mTorr	0.010 nm/s	16 min 22 s
Co <sub>70</sub> Cr <sub>18</sub> Pt <sub>12</sub>	12 nm	20 W	RF	20 sccm	5 mTorr	0.010 nm/s	19 min 38 s
Co <sub>70</sub> Cr <sub>18</sub> Pt <sub>12</sub>	14 nm	20 W	RF	20 sccm	5 mTorr	0.010 nm/s	22 min 55 s
Co <sub>70</sub> Cr <sub>18</sub> Pt <sub>12</sub>	16 nm	20 W	RF	20 sccm	5 mTorr	0.010 nm/s	26 min 11 s
Co <sub>70</sub> Cr <sub>18</sub> Pt <sub>12</sub>	18 nm	20 W	RF	20 sccm	5 mTorr	0.010 nm/s	29 min 27 s
Co <sub>70</sub> Cr <sub>18</sub> Pt <sub>12</sub>	20 nm	20 W	RF	20 sccm	5 mTorr	0.010 nm/s	32 min 44 s
Palladium	0.3 nm	15 W	DC	20 sccm	5 mTorr	0.222 nm/s	1.35 s
Palladium	0.6 nm	15 W	DC	20 sccm	5 mTorr	0.222 nm/s	2.70 s
Palladium	0.9 nm	15 W	DC	20 sccm	5 mTorr	0.222 nm/s	4.05 s
Palladium	1.2 nm	15 W	DC	20 sccm	5 mTorr	0.222 nm/s	5.41 s
Palladium	1.5 nm	15 W	DC	20 sccm	5 mTorr	0.222 nm/s	6.76 s
Palladium	10 nm	15 W	DC	20 sccm	5 mTorr	0.222 nm/s	45.05 s
Tantalum	30 nm	20 W	RF	20 sccm	5 mTorr	0.047 nm/s	10 min 38 s

**Table 4: Deposition layers for different multilayer samples**

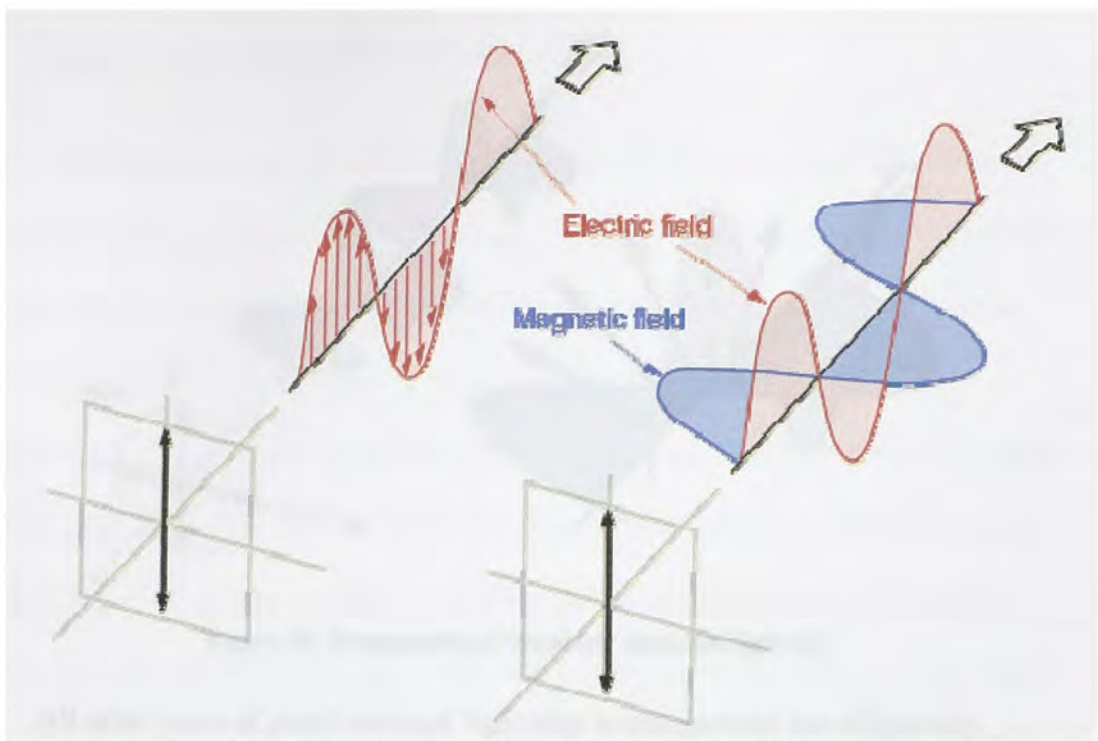
## 5. RESULTS - MAGNETO-OPTICAL KERR EFFECT SYSTEM SETUP

The magneto-optical Kerr effect magnetometer measures the magnetization of a desired sample by changing the external magnetic field applied to the sample. The change in magnetization of the sample is measured by the direct change of the linear polarized light from a laser to elliptically polarized light reflected off the sample. Through the variation of the external applied magnetic field, proper hysteresis curves may be derived by the system. The measured magnetic behavior, acquired from the magneto-optical Kerr effect magnetometer, is obtainable for longitudinal, transverse, and polar modes, for parallel to the plane in two different orientations and for perpendicular to the plane measurements, resulting in a flexible system for magnetic analysis. The magneto-optical Kerr effect magnetometer contains a laser to generate the analyzed change in light, an electrical chopper to sample the light, two poles of a magnet to produce external magnetic fields onto the sample, a quarter-wave plate to maximize the effects of polarization, an additional polarizer, a photodetector to sense the light, and a lock-in amplifier to analyze the signal. Additionally, the LABVIEW software is utilized to control the field in the magnets, read the current applied field through the Hall effect sensor placed between the magnets, and obtain the measurements through the lock-in amplifier.

## 5.1 Polarization of Light

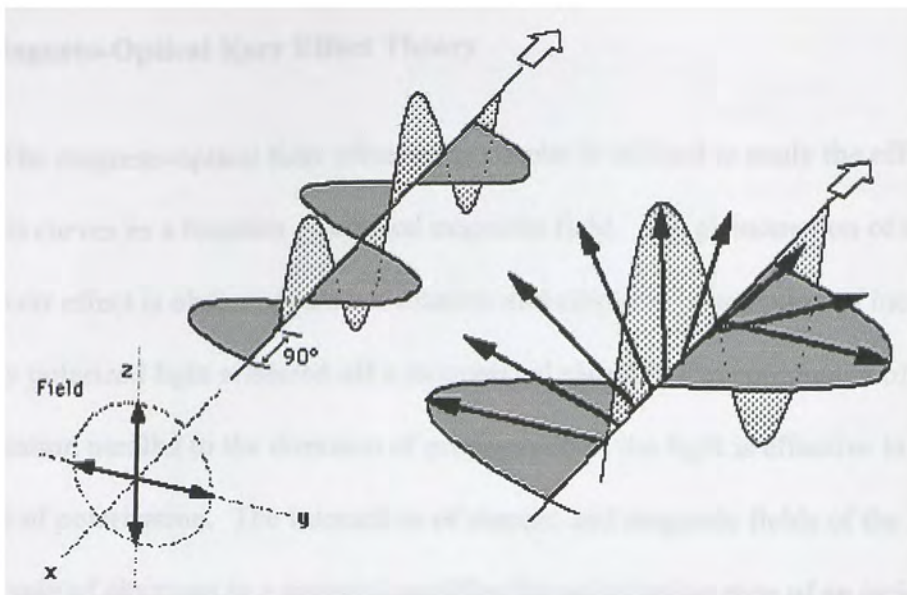
Light waves are like all other electromagnetic waves, consisting of electric and magnetic fields perpendicular to the direction of propagation. The electric and magnetic fields of light waves are also perpendicular to each other. These simple harmonic waves also have characteristic electric vectors that vary in a sinusoidal manner, where the two components of the electric field, which are within a two dimensional plane perpendicular to the direction of propagation, have the same frequency [3]. However, the two components of the electric field may not have the same amplitude or phase. By considering the shape traced out in a fixed plane by the electric vector as a wave passes over it, the polarization state is obtained. The three types of polarization which a light wave may exhibit are linear polarization, circular polarization, and elliptical polarization, where the latter is the most common of the three.

Linearly polarized light is the simplest form and a special case of propagation for an electromagnetic wave. For linearly polarized light, the electric and magnetic fields have the same amplitude and are also in exact phase with each other, illustrated in Figure 34. The direction of the electric field lies within a vector with a constant angle in the plane. Linearly polarized light may consist of an electric field which has a vector, in the plane of propagation, of any random, constant angle. The amplitude of the vector depends on the relative amplitude of the two components, the phase of the light wave at that specific moment.



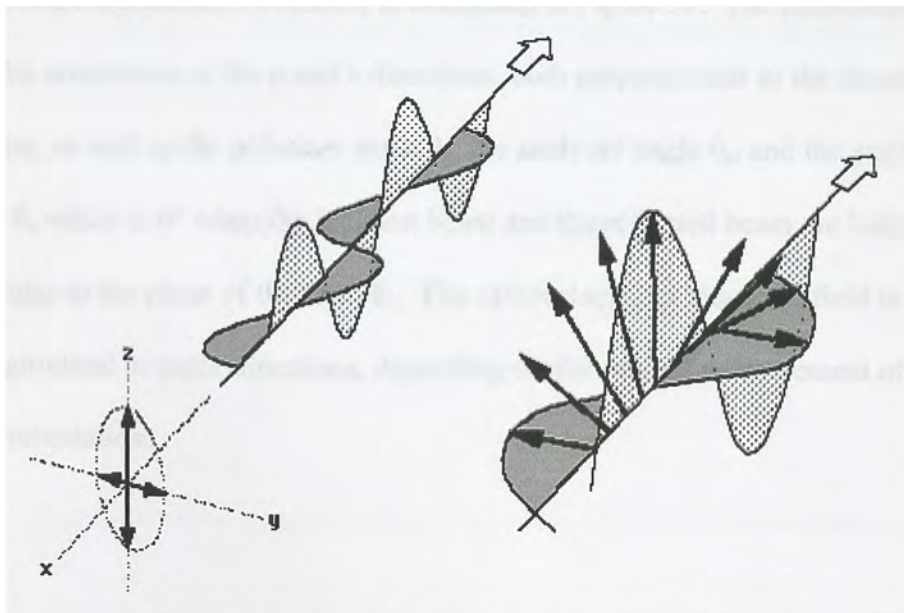
**Figure 35: Propagation of linearly polarized light [3]**

Another special case of polarization of light is circular polarization. Circularly polarized light consists of two perpendicular electromagnetic plane waves of equal amplitude and  $90^\circ$  difference in phase, illustrated in Figure 35. For circularly polarized light, at the moment when one component of the electric field is at its maximum, the perpendicular component is always at its minimum. The two components may have two different phase possibilities within a Cartesian coordinate system defined by the propagation of the light aligned with the x direction. In the first case the z component is  $90^\circ$  ahead of the y component. In contrary, the second case has the z component  $90^\circ$  behind the y component. Viewing the electric vector approaching through the x direction, a circle is formed by the alternating components, where the rotation of the electric vector can be observed as exhibiting either a clockwise or counterclockwise rotation, defined as right-circularly or left-circularly polarized light, respectively.



**Figure 36: Propagation of circularly polarized light [3]**

All other cases of polarization of light may be categorized into elliptically polarized light. Perpendicular electrical components may be  $90^\circ$ , similar to circular polarization, but have different amplitudes, resulting in the electric vector forming an ellipse. Elliptically polarized light also includes the general case in which the perpendicular components are not in  $90^\circ$  phase with each other.



**Figure 37: Propagation of elliptically polarized light [3]**

## 5.2 Magneto-Optical Kerr Effect Theory

The magneto-optical Kerr effect magnetometer is utilized to study the effect of hysteresis curves as a function of applied magnetic field. The phenomenon of magneto-optical Kerr effect is observed as a net rotation and elliptical polarization of incident vertically polarized light reflected off a magnetized sample. The component of magnetization parallel to the direction of propagation of the light is effective in rotating the plane of polarization. The interaction of electric and magnetic fields of the waves with the spin of electrons in a material modifies the polarization state of an incident electromagnetic wave [22]. The magnitude of the change in polarization is proportional to the magnetization of the sample. The rotation of the reflected polarized light off the sample  $\theta_k$  is minimal for paramagnetic materials, however, for ferromagnetic materials, the Kerr effect causes rotations which could be measured. The geometry of the incident and reflected light off a magnetized sample, with magnetized components in the transverse and longitudinal directions, is illustrated in Figure 37. The illustration also displays the orientation of the p and s directions, both perpendicular to the direction of propagation, as well as the polarizer angle  $\theta_p$ , the analyzer angle  $\theta_a$ , and the angle of incidence  $\theta$ , which is  $0^\circ$  when the incident beam and the reflected beam are both perpendicular to the plane of the sample. The external applied magnetic field is oriented in the longitudinal or polar directions, depending on the desired measurement of magnetic orientation.

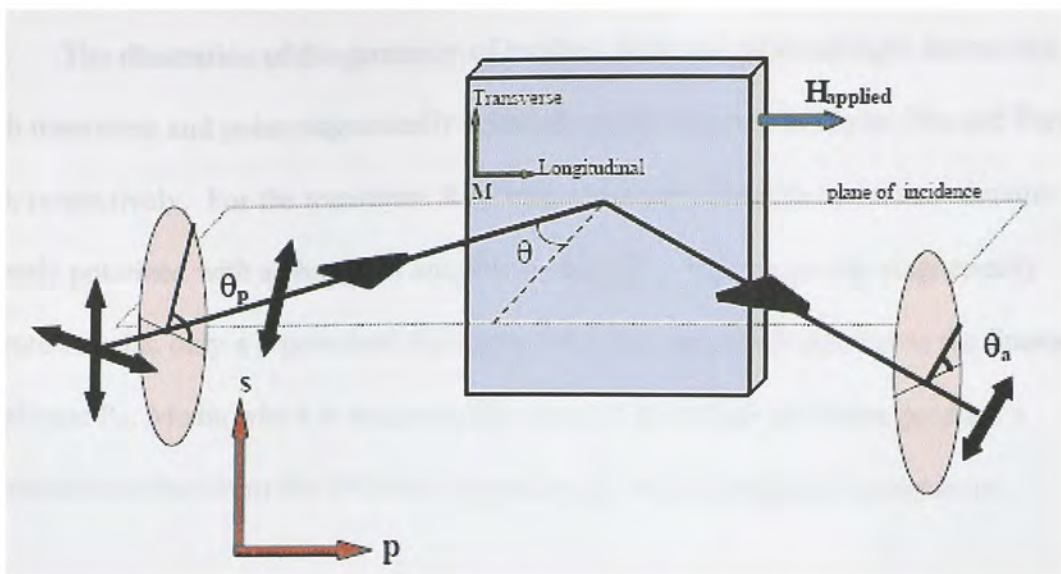


Figure 38: Reflection geometry off a magnetized sample and orientation of  $p$  and  $s$  directions [22]

The illustration of the geometry of incident light and reflected light interacting with longitudinal magnetically oriented media is shown in Figure 38a and Figure 38b through  $p$ -polarized and  $s$ -polarized incident beams, respectively. From the illustration, it is evident that the direction of the energy vector, known as the Kerr amplitude  $R_K$ , in the reflected beam is opposite to the direction of the energy vector in the incident beam. The direction of longitudinal magnetic orientation of the media produces the same end result as its opposing direction counterpart.

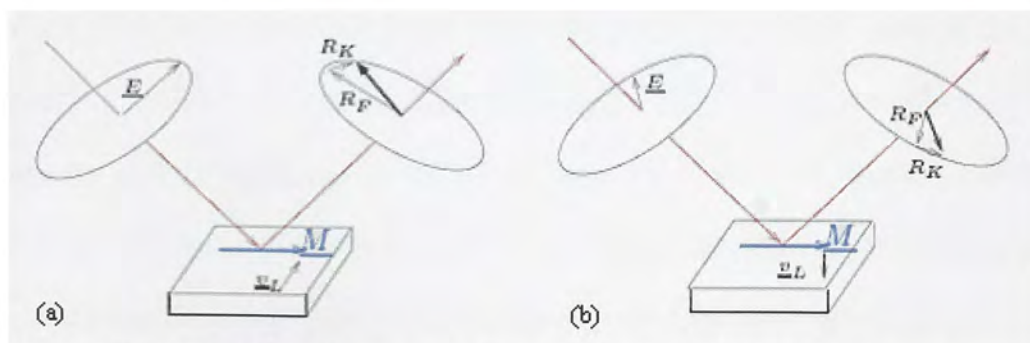
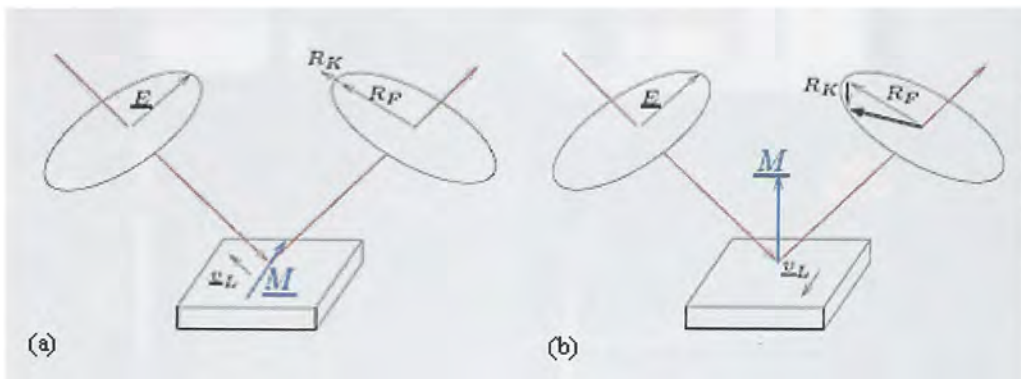


Figure 39: (a) Longitudinal  $p$ -polarized (b) and  $s$ -polarized incident beams



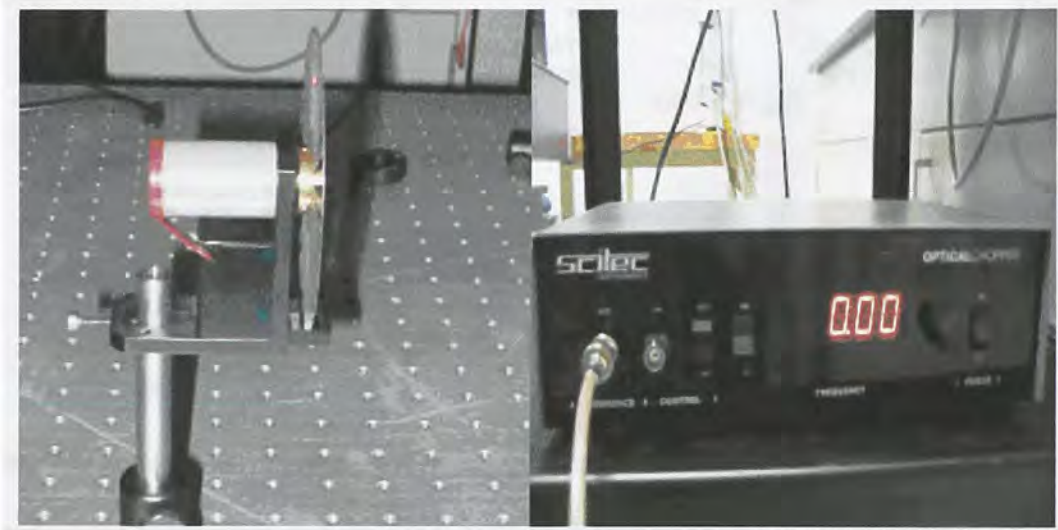
The illustration of the geometry of incident light and reflected light interacting with transverse and polar magnetically oriented media is shown in Figure 39a and Figure 39b, respectively. For the transverse Kerr effect scenario, the reflected beam remains linearly polarized with a change in amplitude only [22]. For transverse magnetically oriented media, only a p-polarized light generates Kerr amplitude parallel to the Fresnel amplitude  $R_F$ . Media which is magnetically oriented in several directions produce a combination effect from the different interaction of each orientation's component.



**Figure 40: (a) Transverse aligned (b) and polar aligned incident reflection beams**

### 5.3 Magneto-Optical Kerr Effect Setup

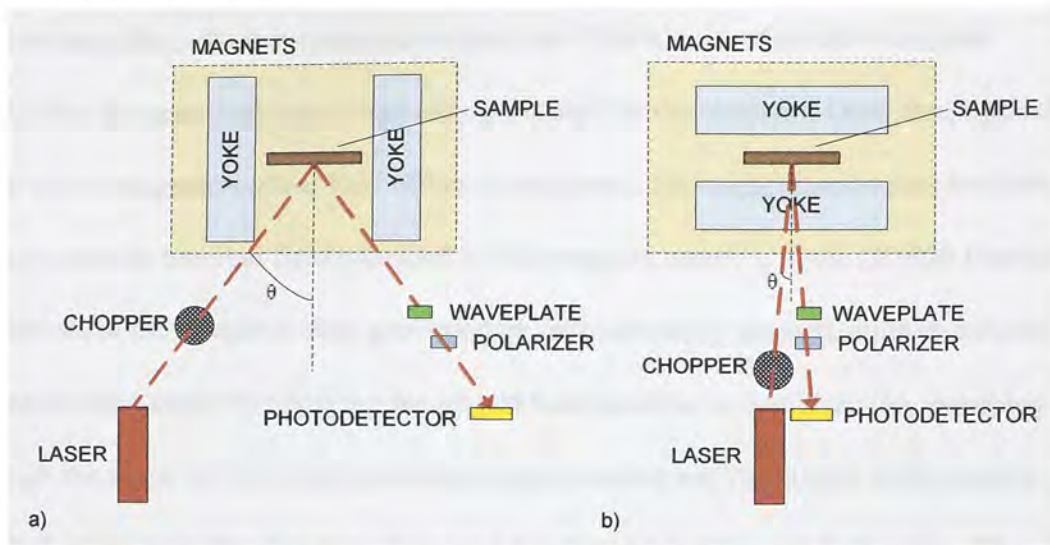
The magneto-optical Kerr effect magnetometer consists of a 632.8 nm Helium-Neon laser that directs a vertically linearly polarized focused beam towards the desired sample. The beam is then pulsed by an optical chopper at a 1 kHz frequency. The optical chopper and the controller for the chopper are shown in Figure 34.



**Figure 41: Optical chopper to pulse the laser and the controller to adjust the frequency**

After the light is chopped, it is reflected off the sample that is positioned between two poles of a magnet. The magnets may induce a magnetic field that can vary from -2 Tesla to 2 Tesla by changing the current through the magnets. The two poles of the magnets may be oriented for either longitudinal and transverse modes or polar mode, by aligning the poles of the magnet parallel to the plane, or normal to the plane, respectively. Depending on the mode which the sample is investigated, the angle of reflection of the light on the sample is either  $0.5^\circ$  with the normal to the plane and a full angle of  $1^\circ$  to analyze perpendicular components of the magnetization, as shown in Figure 35a, or  $45^\circ$

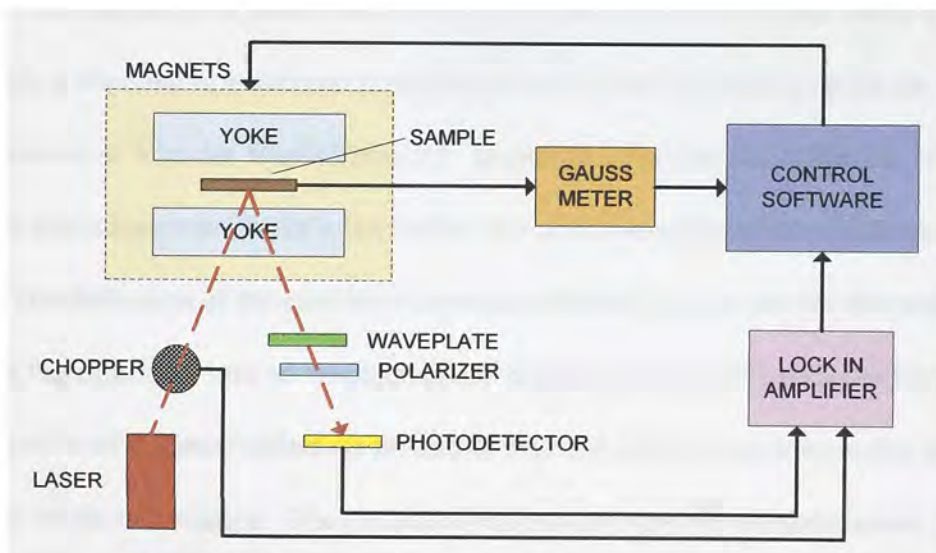
with the normal to the plane and a full angle of  $90^\circ$  to analyze longitudinal components as seen in Figure 35b



**Figure 42: (a) Magnets aligned to analyze in longitudinal mode (b) and perpendicular mode**

. The beam is then reflected off the sample is directed towards a quarter-wave plate. The quarter-wave plate divides any polarized light striking it into two components, retarding the component with larger index of refraction by  $90^\circ$  in phase in respect to the component with smaller index of refraction. The outcome is a linearly polarized light containing the change of linear polarization from the reflection off the magnetized sample. After the light passes through the quarter-wave plate, it is then directed through a polarizer oriented horizontally,  $90^\circ$  from the original vertically polarized light. Any light that passes through polarizer is considered the resulting Kerr effect changes from the reflection off the magnetized sample. The outcome of complete absence of light through the polarizer indicates that the reflected light was not polarized and that the sample was not magnetic. Once the light passes through the polarizer, it is then sensed by a photodetector. The photodetector converts the optical signal from the polarizer to an

electric signal. The electrical signal is then analyzed only at the frequency generated from the optical chopper, through the utilization of the lock-in amplifier. Through the lock-in amplifier, all other frequency signals are filtered out except for the signal containing the same reference frequency generated by the chopper. Once the physical setup of the magneto-optical Kerr effect is completed, the magnetization may be derived for any specific external field provided by the magnets, nearly 2 Tesla (20,000 Oersted). Hysteresis of the sample is then generated by first saturating magnetization in a direction normal to the sample by applying the largest field possible in that direction, sweeping through the range of field until saturation magnetization and the largest field possible is reached in the opposite direction, then attaining the original largest field again. The physical setup of the magneto-optical Kerr effect magnetometer is demonstrated in Figure 42.



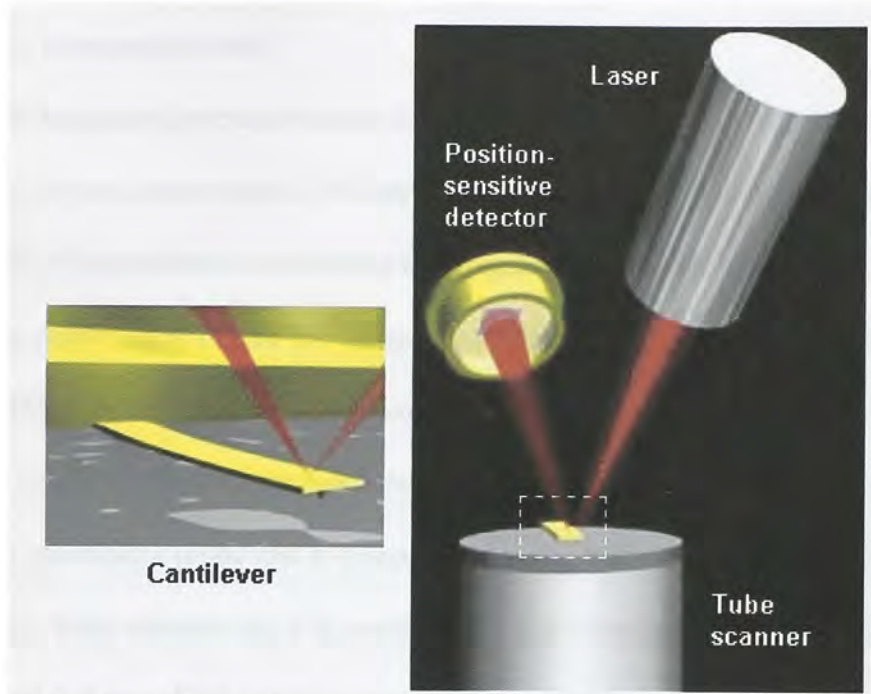
**Figure 43: Magneto-optical Kerr effect magnetometer layout**

## 6. RESULTS - CHARACTERIZATION OF MAGNETIC MEDIA

The characterization of the three-dimensional media was accomplished through the atomic force microscope, magnetic force microscope, magneto-optical Kerr effect magnetometer, and x-ray diffraction system. With the aid of these advanced mechanisms, it was possible to generate topography images, magnetic images, hysteresis curves, and crystallographic structures.

The atomic force microscope is a scanning probe microscope (SPM) that maps the topography onto an image form. The atomic force microscope consists of a cantilever with a sharp probe, or tip, at the end, usually with tip sizes of only a few nanometers. The cantilever utilized in the atomic force microscope is a small beam anchored at one end and open ended at the other. The probe is then brought into close proximity with the surface of the sample to be observed. During the scanning of the sample, while the probe is engaged, it encounters attraction or repulsion forces from interaction of the tip and the sample, known as Van der Waals force [3]. These forces lead to the deflection of the cantilever that adheres to Hooke's law, where the spring constant of the cantilever is known. The deflection of the cantilever is measured using a laser that is reflected from the top of the cantilever into an arrangement of photodetector as illustrated in Figure 34. The utilization of the laser reflection instead of a piezo resistive probe increases the sensitivity of the microscope. The reflection of the laser onto the photodetectors can determine the distance from the probe to the sample by analyzing the offset and direction of the reflection compared to the center of the arrangement of the photodetectors. Scanning of the sample produces an image that corresponds to numerous rows, resulting

in an image of a small area. In most atomic force microscopes, a feedback system is appended to adjust the distance from the probe to the sample to keep the force between the probe and the sample constant, avoiding the risk of damaging the probe by colliding into the surface that may not be completely flat.



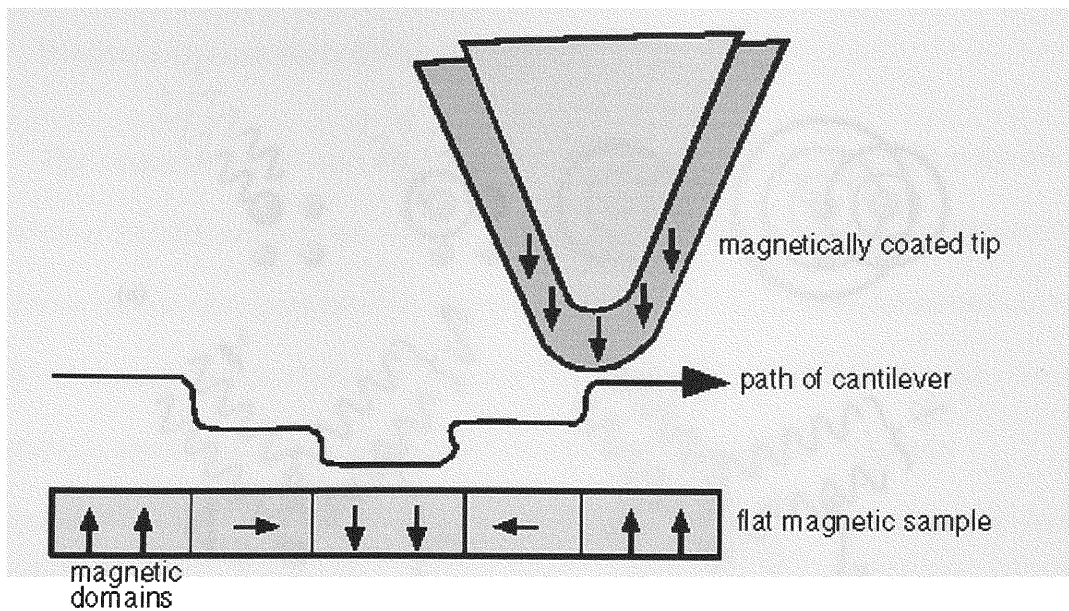
**Figure 44: Atomic force microscope consisting of laser, cantilever, and photodetectors**

Several modes of operation have been developed for the atomic force microscope. Three common modes of operation are known as contact mode, non-contact mode, and dynamic contact mode. In contact mode, the force between the probe and the surface is kept constant during scanning of the sample by maintaining a constant deflection on the cantilever. When operating in non-contact mode, the cantilever is oscillated at its resonance frequency. Due to the interaction forces between the probe and the surface of the sample, the oscillation is modified, providing the desired measurements concerning the sample. Dynamic contact mode operates by oscillating the cantilever as well;

however, the cantilever is oscillated with enough force so that it comes in contact with the sample, where the upward force away from the sample is sufficient to separate the probe from the surface. Several measurements, analysis techniques, and operations can be investigated, such as topography, roughness, and step heights, making the atomic force microscope a resourceful tool.

The magnetic force microscope is also a form of a scanning force microscope, based only on non-contact mode. Magnetic force microscopes can map the spatial distribution of magnetism by measuring the magnetic interaction between the probe and the sample, displayed in Figure 35. Magnetic materials are used for the probe and the sample, adding the capabilities to measure atomic force and magnetic interaction.

Usually, a cantilever used for atomic force microscopes is coated with a magnetic material to assemble a probe that is susceptible to magnetic fields. With the utilization of the magnetic force microscope, it is possible to analyze the magnetic field gradient of the sample, read and record information onto magnetic media, any many other applications. The measuring of the topography and magnetic image of the sample is accomplished by executing a two-pass method. In the first pass, the topography of the sample is determined. During the second run, the cantilever is lifted to a selected height, where the scan is proceeded with the topography of the sample stored, keeping the distance between the cantilever and the surface constant. At this distance away from the sample, during the second run, the Van der Waals force no longer contributes to the attraction or repulsion of the probe, outcome resulting in obtaining only magnetic information of the sample [23].

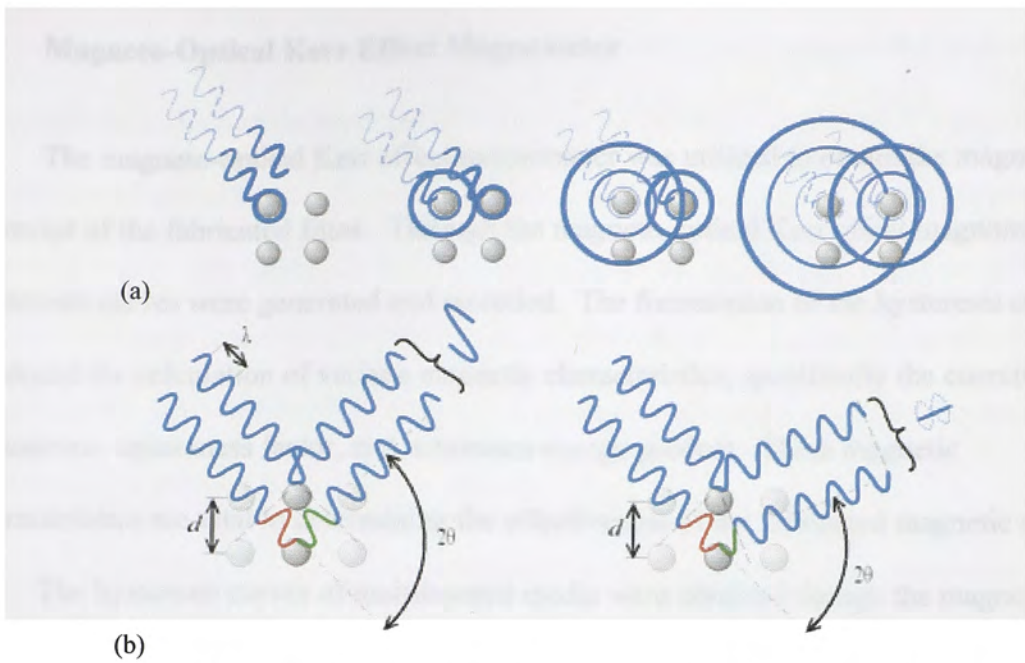


**Figure 45: Magnetic force microscope utilized to analyze magnetic films**

Crystallography of a desired sample can be analyzed by an x-ray diffraction system. Through the x-ray diffraction system, a crystallographic pattern is generated by analyzing and revealing the nature of the lattice. The observed crystal lattice can be determined by using Bragg's law. Bragg's law indicates that when x-rays hit an atom, they force the electronic cloud to move like an electromagnetic wave. The movement of the charges re-radiates waves with the same frequency; however, they are slightly blurred due to the phenomenon known as Rayleigh scattering, shown in Figure 37a [3]. The re-emitted x-rays interact through either constructive or deconstructive interference shown in Figure 37b. The interference is constructive when the phase shift is proportional to  $2\pi$ , expressed by Bragg's law in Equation 24. Bragg's law is expressed by the wavelength of the x-rays  $\lambda$ , the distance between each atom  $d$ , known as the lattice constant, an integer  $n$ , and the angle between the incident x-rays and the scattering planes  $\theta$ .

$$n\lambda = 2d \sin \theta \quad (24)$$





**Figure 46: X-ray diffraction (a) Rayleigh scattering and (b) interference [3]**

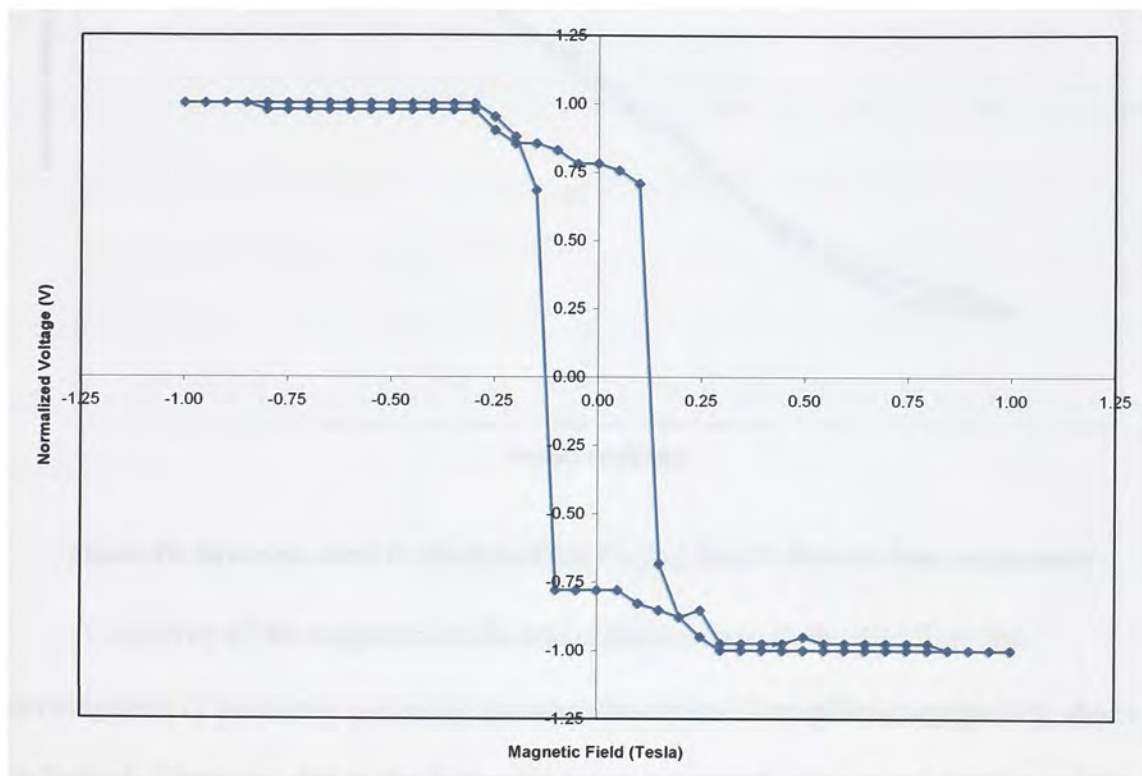
## 6.1 Magneto-Optical Kerr Effect Magnetometer

The magneto-optical Kerr effect magnetometer was utilized to obtain the magnetic behavior of the fabricated films. Through the magneto-optical Kerr effect magnetometer, hysteresis curves were generated and recorded. The formulation of the hysteresis curves produced the calculation of various magnetic characteristics, specifically the coercivity, remanence, squareness factor, and maximum energy product. These magnetic characteristics are vital to determining the effectiveness of the fabricated magnetic media.

The hysteresis curves of multilayered media were obtained through the magneto-optical Kerr effect magnetometer. An optimization of cobalt/palladium multilayers, implemented as a stack and acting as one single magnetic layer, was shown through the characterization of the magnetic behavior. The determination of the coercivity, squareness factor, coercive squareness, remanence, and maximum energy product was analyzed through the variation of cobalt and palladium layers within a stack and the number of layers  $N$  within a stack.

The thickness of the cobalt magnetic layers was investigated from one monolayer, approximately 0.2 nm, to 0.6 nm by divisions of 0.1 nm (0.2 nm, 0.3 nm, 0.4 nm, 0.5 nm, and 0.6 nm). The thickness of the palladium nonmagnetic layers was examined from one monolayer, approximately 0.3 nm, to 1.5 nm by divisions of 0.3 nm (0.3 nm, 0.6 nm, 0.9 nm, 1.2 nm, and 1.5 nm). The dependence of the magnetic behaviors of the magnetic media was also examined as a function of layers  $N$  in one stack, implemented as one magnetic behavior. The number of layers  $N$  in one stack were varied from one layer of cobalt and palladium up to forty layers ( $N = 1, 3, 5, 10, 15, 20, 25, 30,$  and  $40$ ).

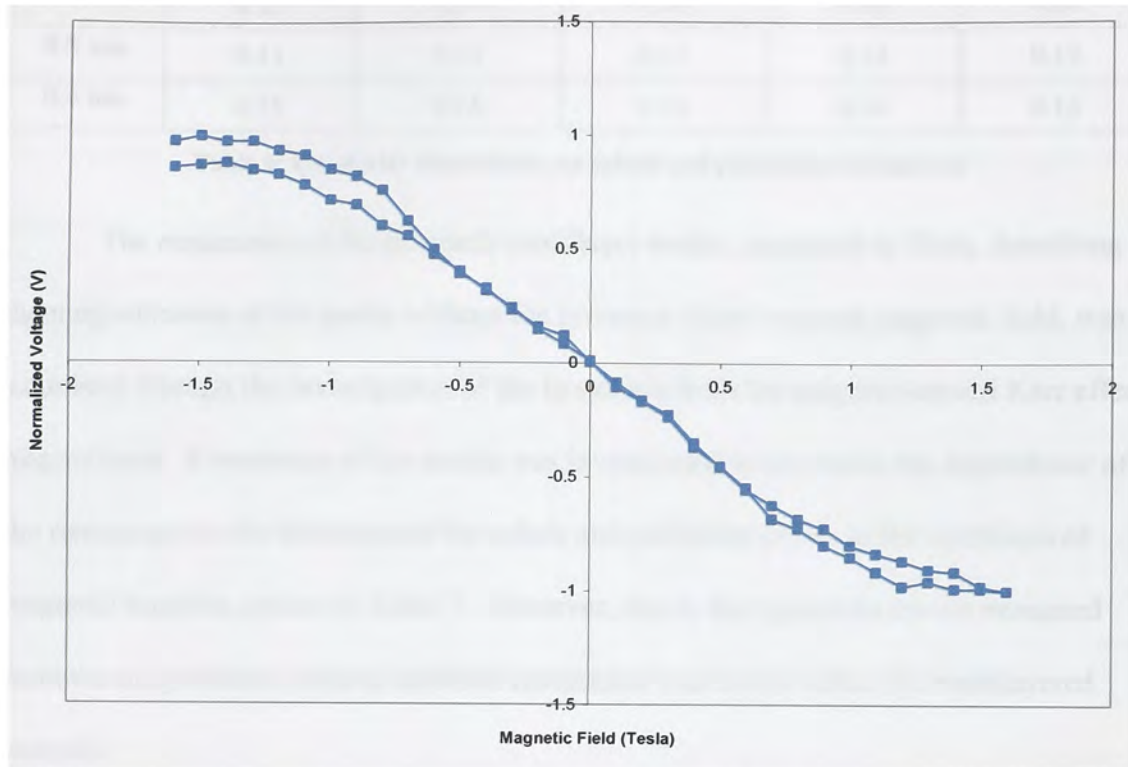
The magneto-optical Kerr effect magnetometer was used to analyze the magnetic properties of in-house fabricated cobalt/palladium multilayered samples. Twenty-five of the fabricated samples were of one stack consisting of fifteen magnetic and non-magnetic layers ( $N = 15$ ). The hysteresis curves observed from the magneto-optical Kerr effect magnetometer were recorded and plotted. As an example, displayed in Figure 46 are the plotted results from the multilayered sample consisting of a thickness of 0.5 nm and 0.9 nm cobalt and palladium layers, respectively.



**Figure 47: Hysteresis curve for fabricated multilayer sample observed from magnetometer**

The thickness of the  $\text{Co}_{70}\text{Cr}_{18}\text{Pt}_{12}$  magnetic layers was investigated from 0.1 nm, to 0.9 nm by divisions of 0.1 nm (0.1 nm, 0.2 nm, 0.3 nm, 0.4 nm, 0.5 nm, 0.6 nm, 0.7 nm, 0.8 nm, and 0.9 nm). The magneto-optical Kerr effect magnetometer was utilized to examine the magnetic behavior of in-house fabricated  $\text{Co}_{70}\text{Cr}_{18}\text{Pt}_{12}$  samples. The

hysteresis curves observed from the magneto-optical Kerr effect magnetometer were recorded and plotted. As an example, displayed in Figure 47 are the plotted results from the  $\text{Co}_{70}\text{Cr}_{18}\text{Pt}_{12}$  sample consisting of a thickness of 5 nm.



**Figure 48: Hysteresis curve for fabricated  $\text{Co}_{70}\text{Cr}_{18}\text{Pt}_{12}$  sample observed from magnetometer**

Coercivity of the magnetic media was collected through the data from the investigation of hysteresis curves by the magneto-optical Kerr effect magnetometer, shown in Table 6. However, due to the hysteresis curves measured, none or minimal coercivity was found within the multilayered samples. Coercivity of the multilayered media ideally possesses a dependence on the thickness of the magnetic and nonmagnetic layers, cobalt and palladium for the implemented multilayers, respectively.

<b>Cobalt Thickness</b>	<b>Coercivity (Tesla)</b>				
	<b>Palladium 0.3 nm</b>	<b>Palladium 0.6 nm</b>	<b>Palladium 0.9 nm</b>	<b>Palladium 1.2 nm</b>	<b>Palladium 1.5 nm</b>
<b>0.2 nm</b>	0.04	0.04	0.05	0.05	0.03
<b>0.3 nm</b>	0.07	0.05	0.08	0.03	0.07
<b>0.4 nm</b>	0.11	0.09	0.10	0.08	0.08
<b>0.5 nm</b>	0.15	0.12	0.13	0.14	0.12
<b>0.6 nm</b>	0.15	0.15	0.14	0.14	0.13

**Table 6: Coercivity dependence on cobalt and palladium thicknesses**

The remanence of the magnetic multilayer media, measured in Tesla, describing the magnetization of the media without the presence of any external magnetic field, was examined through the investigation of the hysteresis from the magneto-optical Kerr effect magnetometer. Remanence of the media was investigated to determine the dependence of the remanence on the thickness of the cobalt and palladium layers in the multilayered magnetic samples, shown in Table 7. However, due to the hysteresis curves measured from the magnetometer, none or minimal remanence was found within the multilayered samples.

<b>Cobalt Thickness</b>	<b>Remanence (Tesla)</b>				
	<b>Palladium 0.3 nm</b>	<b>Palladium 0.6 nm</b>	<b>Palladium 0.9 nm</b>	<b>Palladium 1.2 nm</b>	<b>Palladium 1.5 nm</b>
<b>0.2 nm</b>	0.03	0.02	0.02	0.04	0.03
<b>0.3 nm</b>	0.21	0.20	0.19	0.22	0.17
<b>0.4 nm</b>	0.47	0.52	0.48	0.43	0.43
<b>0.5 nm</b>	0.85	0.79	0.78	0.69	0.73
<b>0.6 nm</b>	0.86	0.82	0.77	0.71	0.70

**Table 7: Remanence dependence on cobalt and palladium thicknesses**

The squareness factor of the multilayered media was calculated by determining the ratio of the remanence by the saturation magnetization obtained from the investigation. The impact of the distinct cobalt and palladium thickness on squareness factor of all the fabricated magnetic media is shown in Table 8. Larger squareness factors induce thermal stability and noise reduction to magnetic media. However, due to the hysteresis curves measured, squareness factor was minimal for all samples due to the absence of remanence within the multilayered samples.

<b>Cobalt Thickness</b>	<b>Squareness Factor</b>				
	<b>Palladium 0.3 nm</b>	<b>Palladium 0.6 nm</b>	<b>Palladium 0.9 nm</b>	<b>Palladium 1.2 nm</b>	<b>Palladium 1.5 nm</b>
<b>0.2 nm</b>	0.03	0.02	0.02	0.04	0.03
<b>0.3 nm</b>	0.21	0.20	0.19	0.22	0.17
<b>0.4 nm</b>	0.47	0.52	0.48	0.43	0.43
<b>0.5 nm</b>	0.85	0.79	0.78	0.69	0.73
<b>0.6 nm</b>	0.86	0.82	0.77	0.71	0.70

**Table 8: Squareness factor dependence on cobalt and palladium thicknesses**

The coercive squareness of the magnetic media was calculated by the determining the ratio of the magnetic field at the intersection of the tangent line at the coercivity and the vertical line crossing through the remanent magnetization by the coercivity, obtained from the investigation. The influence of the various cobalt and palladium thicknesses on coercive squareness of the fabricated magnetic media is shown in Table 9. Larger coercive squareness also induces thermal stability and noise reduction to the magnetic media. However, due to the hysteresis curves measured, coercive squareness factor was minimal for all samples due to the absence of remanence and coercivity within the multilayered samples.

Cobalt Thickness	Coercive Squareness				
	Palladium 0.3 nm	Palladium 0.6 nm	Palladium 0.9 nm	Palladium 1.2 nm	Palladium 1.5 nm
0.2 nm	0	0	0	0	0
0.3 nm	0.16	0.13	0.16	0.18	0.17
0.4 nm	0.38	0.51	0.45	0.46	0.49
0.5 nm	0.66	0.64	0.69	0.63	0.65
0.6 nm	0.70	0.67	0.67	0.71	0.70

**Table 9: Coercive squareness factor dependence on cobalt and palladium thicknesses**

The maximum energy product was calculated by obtaining the largest fitting rectangle in the second quadrant of the hysteresis loop. The dependence on the thickness of the cobalt magnetic layer and palladium nonmagnetic layer is exhibited in Table 10.

Cobalt Thickness	Maximum Energy Product (Tesla <sup>2</sup> )				
	Palladium 0.3 nm	Palladium 0.6 nm	Palladium 0.9 nm	Palladium 1.2 nm	Palladium 1.5 nm
0.2 nm	0.00	0.00	0.00	0.00	0.00
0.3 nm	0.01	0.02	0.02	0.01	0.01
0.4 nm	0.04	0.05	0.05	0.05	0.05
0.5 nm	0.09	0.08	0.10	0.11	0.09
0.6 nm	0.11	0.10	0.12	0.11	0.10

**Table 10: Maximum energy product dependence on cobalt and palladium thicknesses**

The magnetic behaviors of coercivity, remanence, squareness factor, and maximum energy product all should ideally vary on the number of layer repetitions of the magnetic and nonmagnetic layers as seen in Table 11. Layers considered for layer repetitions consisted each of one cobalt level and one palladium level. The amount of layer repetitions in a stack, behaving as one magnetic layer, was varied to show the magnetic behaviors within a range that exhibited their fluctuations. Each layer repetition represents a 0.6 nm cobalt layer stacked with a 0.9 nm palladium layer.

Layers Repetitions	Coercivity	Remanence	Squareness Factor	Coercive Squareness	Maximum Energy Product
1	0.06	0.81	0.81	0.19	0.01
3	0.07	0.61	0.61	0.64	0.07
5	0.07	0.73	0.73	0.53	0.10
10	0.10	0.79	0.79	0.68	0.11
15	0.14	0.77	0.77	0.67	0.12
20	0.16	0.78	0.78	0.70	0.12
25	0.15	0.75	0.75	0.71	0.12
30	0.18	0.68	0.68	0.68	0.13
40	0.20	0.79	0.79	0.72	0.14

**Table 11: Magnetic behavior dependence on layer repetition of cobalt and palladium**

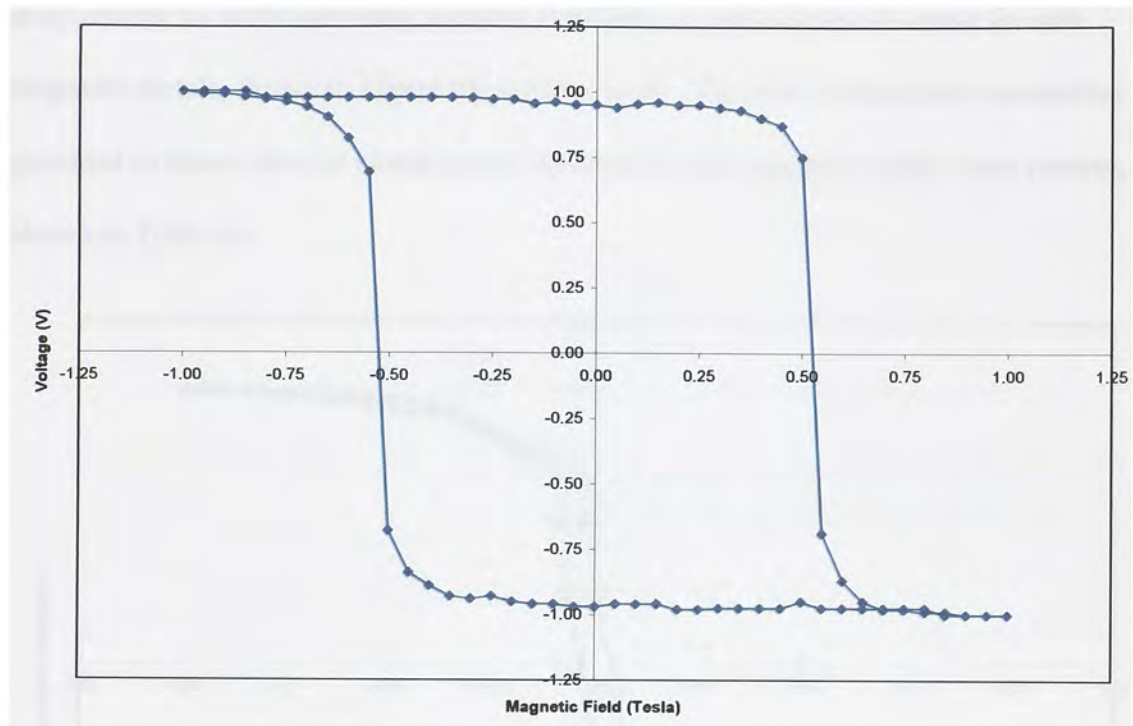
The various magnetic behaviors of  $\text{Co}_{70}\text{Cr}_{18}\text{Pt}_{12}$  magnetic films are displayed in Table 12 as a function of the thickness. The alloy was implemented as a magnetic layer, from 1 nm to 9 nm. The nine magnetic films were all deposited on a 10 nm palladium seedlayer. Only one magnetic layer was deposited to analyze the magnetic characteristics without the interdependence several magnetic and non-magnetic layers may generate.

$\text{Co}_{70}\text{Cr}_{18}\text{Pt}_{12}$ Thickness	Coercivity	Remanence	Squareness Factor	Coercive Squareness	Maximum Energy Product
1 nm	0.00	0.00	0.00	0.00	0.00
2 nm	0.00	0.00	0.00	0.00	0.00
3 nm	0.00	0.00	0.00	0.00	0.00
4 nm	0.00	0.00	0.00	0.00	0.00
5 nm	0.00	0.00	0.00	0.00	0.00
6 nm	0.00	0.00	0.00	0.00	0.00
7 nm	0.00	0.00	0.00	0.00	0.00
8 nm	0.00	0.00	0.00	0.00	0.00
9 nm	0.00	0.00	0.00	0.00	0.00

**Table 12: Magnetic behavior dependence on  $\text{Co}_{70}\text{Cr}_{18}\text{Pt}_{12}$  magnetic layer thickness**



The magnometer was used to analyze the magnetic properties of a cobalt/palladium sample obtained from the University of Houston. The characteristics of the sample were fifteen cobalt and palladium layers layers of 0.6 nm and 1.2 nm thickness, respectively. Results for the sample displayed a typical hysteresis curve for perpendicular media, seen in Figure 47. The observed magnetic behavior provided evidence that multilayers exhibit magnetic features and that the magnometer functioned properly, shown in Table 13.

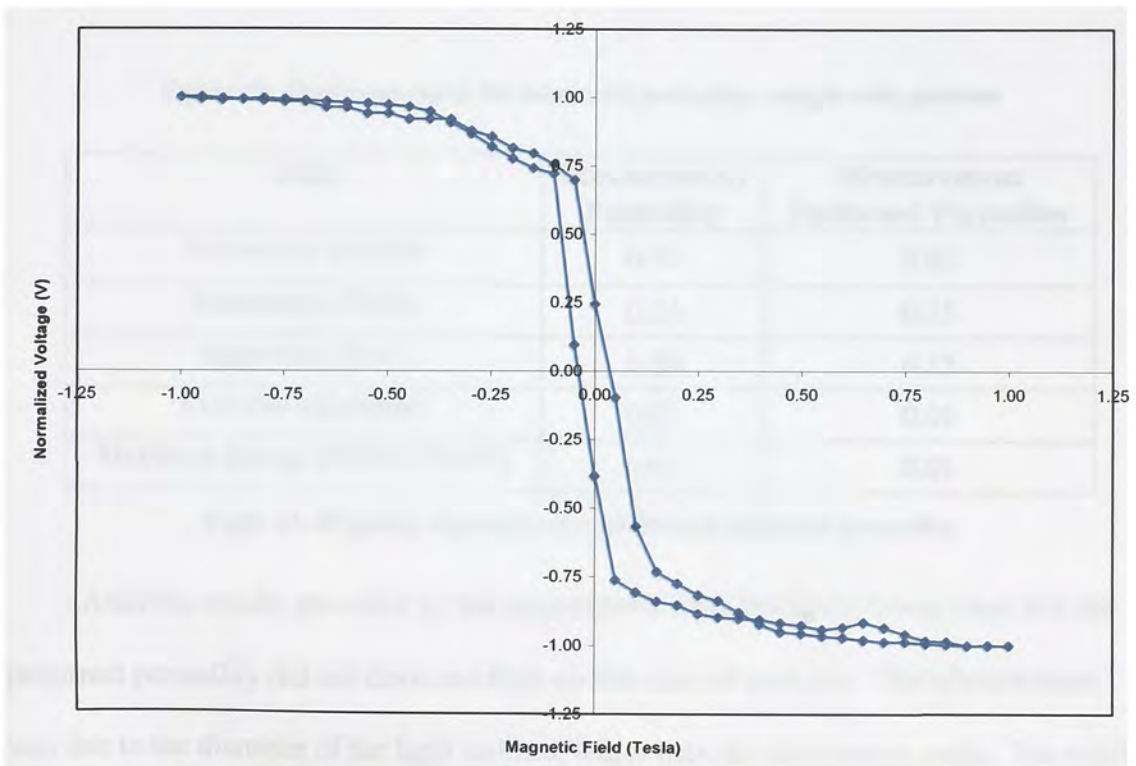


**Figure 49: Hysteresis curve for Co/Pd sample observed from magnometer**

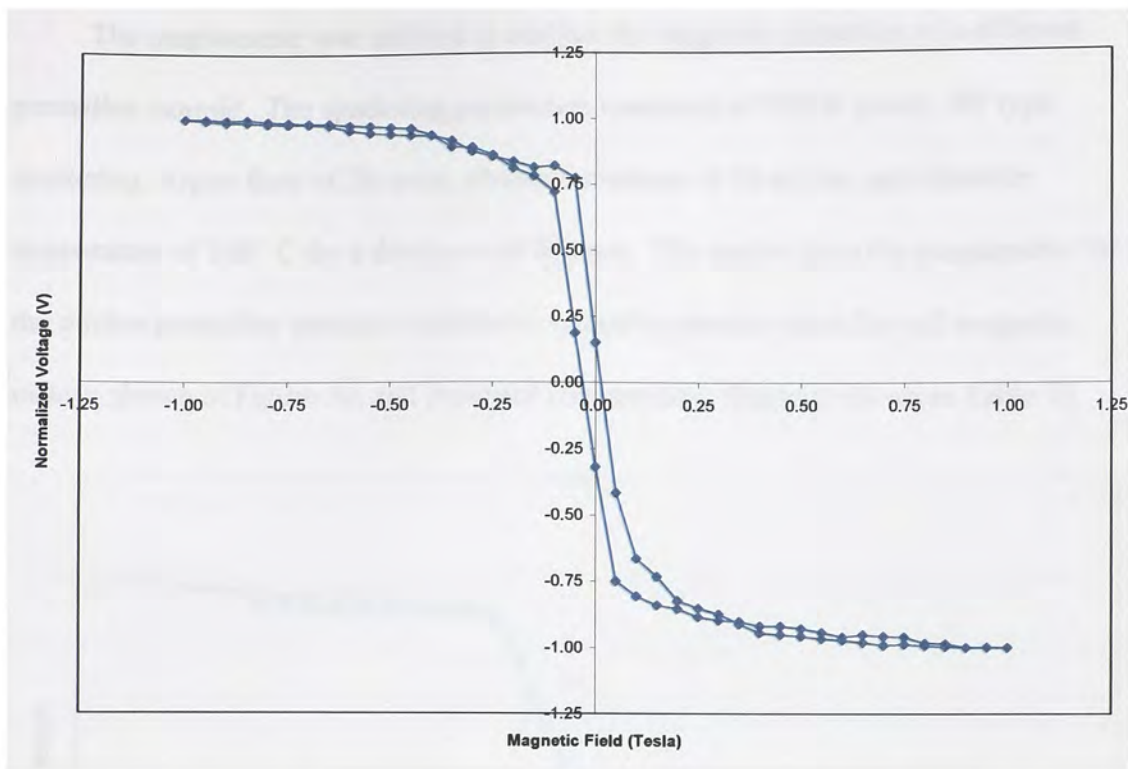
Unit	Measurement
Coercivity (Tesla)	0.53
Remanence (Tesla)	0.95
Squareness Factor	0.95
Coercive Squareness	0.91
Maximum Energy Product (Tesla <sup>2</sup> )	0.39

**Table 13: Magnetic characteristics of Co/Pd sample**

The magneto-optical Kerr effect magnetometer was also utilized to analyze the magnetic properties of two different permalloy samples. Both samples were nearly identical, with sputtering parameters of 100 W power, RF type sputtering, Argon flow of 20 sccm, chamber pressure of 10 mTorr, and chamber temperature of 24° C for a thickness of 110 nm. The second permalloy sample was then patterned with the focused ion beam, forming a periodicity pattern of 100 nm. The measured results from the magnetometer for both permalloy samples exhibited a typical hysteresis curve for soft magnetic metals, shown in Figure 48 and Figure 49. The observed magnetic properties provided evidence that the characteristic features for soft magnetic metals were present, shown in Table 14.



**Figure 50: Hysteresis curve for fabricated permalloy sample without patterns**



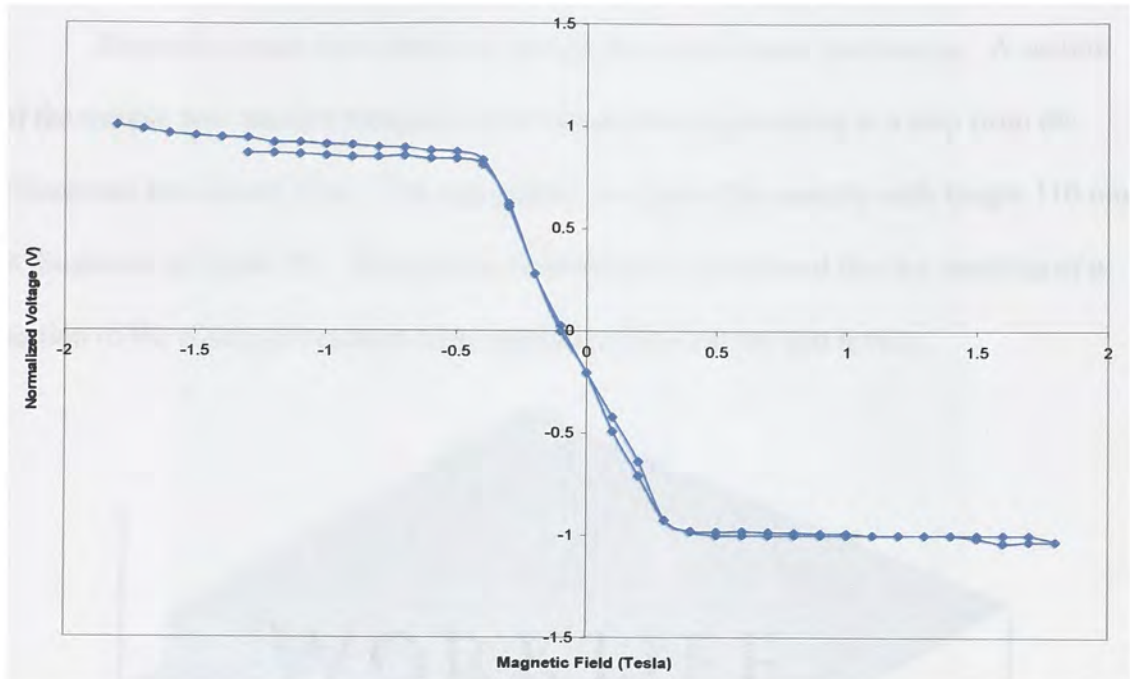
**Figure 51: Hysteresis curve for fabricated permalloy sample with patterns**

Unit	Measurement Permalloy	Measurement Patterned Permalloy
Coercivity (Tesla)	0.05	0.02
Remanence (Tesla)	0.24	0.15
Squareness Factor	0.24	0.15
Coercive Squareness	0.01	0.01
Maximum Energy Product (Tesla <sup>2</sup> )	0.01	0.01

**Table 14: Magnetic characteristics of flat and patterned permalloy**

After the results provided by the magnometer were finalized, it was clear that the patterned permalloy did not have an effect on this type of analysis. This phenomenon was due to the diameter of the light utilized, larger than the micrometer scale. The results observed from the magnometer provide average magnetic behavior much larger in scale than nanometers, causing the nanometer patterns to become negligible.

The magnetometer was utilized to analyze the magnetic properties of a different permalloy sample. The sputtering parameters consisted of 100 W power, RF type sputtering, Argon flow of 20 sccm, chamber pressure of 10 mTorr, and chamber temperature of 100° C for a thickness of 400 nm. The results from the magnetometer for the thicker permalloy samples exhibited a typical hysteresis curve for soft magnetic metals, shown in Figure 50, and provided characteristic features, shown in Table 15.



**Figure 52: Hysteresis curve for fabricated permalloy sample of 400 nm**

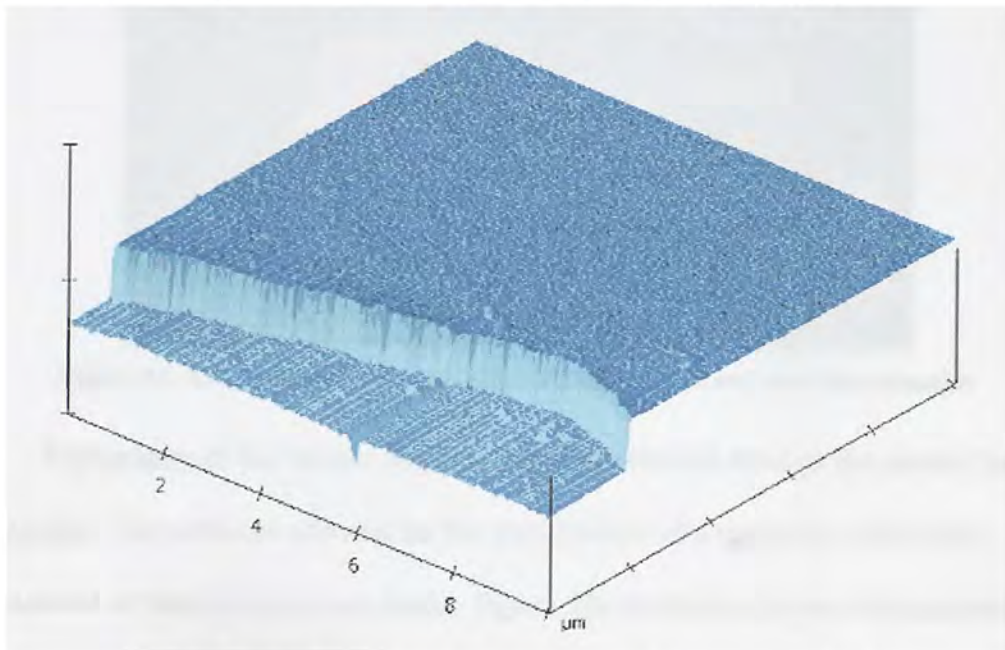
Unit	Measurement Permalloy
Coercivity (Tesla)	0.00
Remanence (Tesla)	0.00
Squareness Factor	0.00
Coercive Squareness	0.00
Maximum Energy Product (Tesla <sup>2</sup> )	0.00

**Table 15: Magnetic characteristics of flat and patterned permalloy**

## 6.2 Atomic Force Microscopy

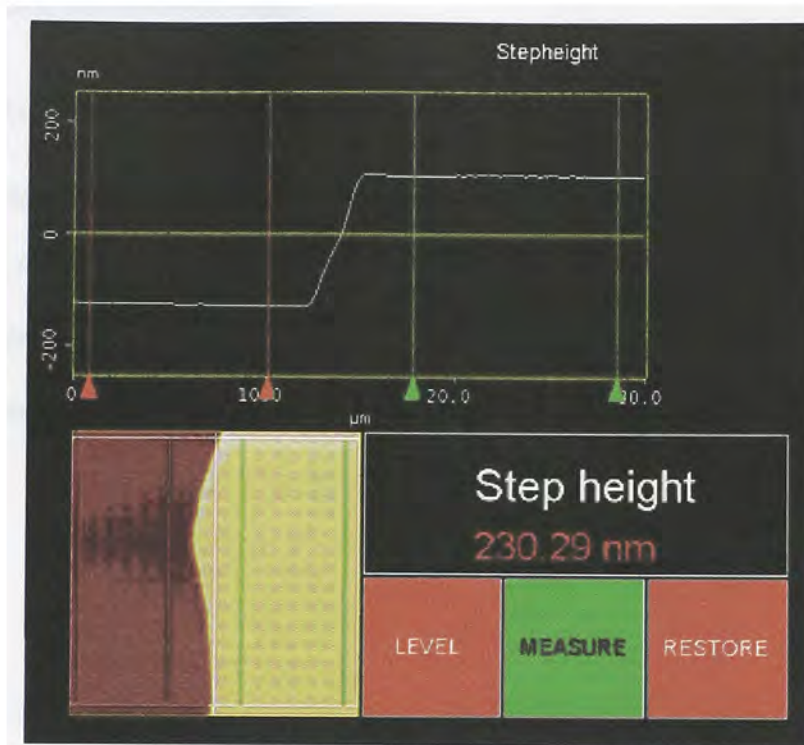
The atomic force microscope was mainly utilized to obtain the deposition rates of sputtering by viewing the step heights and to observe the topography of certain samples. Through the accurate precision of the probe, nanometer resolution was obtainable. The resolution was sufficient to analyze nanometer thin films or larger. Computational analysis was performed by the software, Nanoscope, providing results in an image form.

Deposition rates were obtained through the atomic force microscope. A section of the sample was masked through the deposition process, resulting in a step from the silicon and the desired layer. The topography of a permalloy sample with height 110 nm is illustrated in Figure 50. Through the illustration, it is observed that the masking of a section of the silicon provided a clear separation between the two levels.



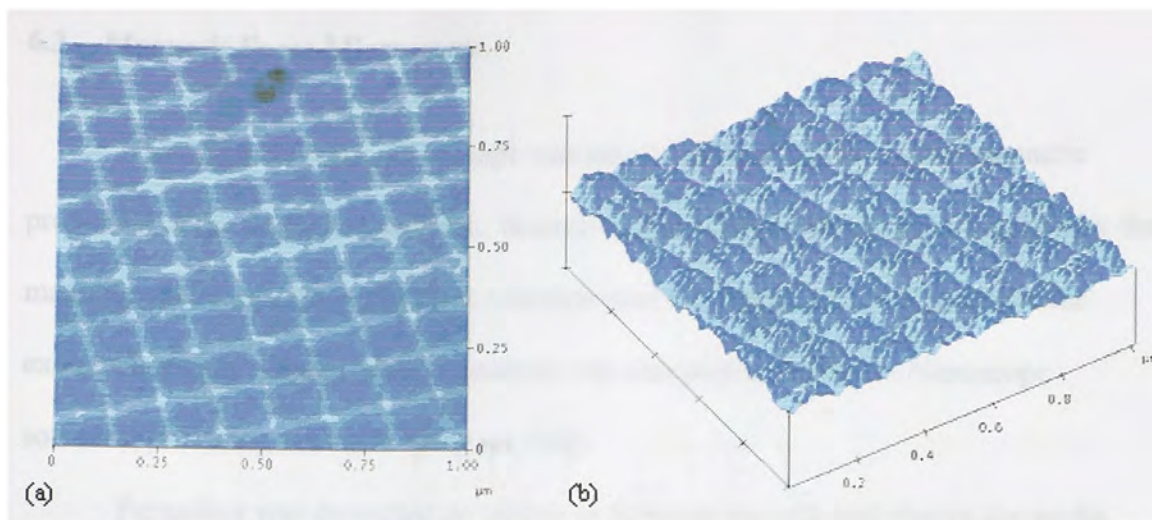
**Figure 53: AFM image in 3D of step coverage for rate determination**

The software for the atomic force microscope allowed for the determination of step heights on a sample. Within the software, the step height tool calculated the difference of heights between two distinct regions, exemplified in Figure 51 for a 230 nm thick permalloy sample. After the two different regions within a sample are chosen for comparison, the software calculates the average height for both regions and takes the difference.



**Figure 54: AFM utilization for step height measurements and rate determination**

Topography of the desired samples was also obtained through the atomic force microscope. The software allowed for the visualization of a sample in either two-dimensional or three-dimensional mode. Figure 52a illustrates the two-dimensional visualization and Figure 52b shows the three-dimensional mode of a patterned permalloy sample. Through the illustration, the 100 nm periodicity etched by the focused ion beam is clearly visible, confirmed by the calculated spectral frequency through the software.



**Figure 55: (a) AFM image of a patterned permalloy sample in 2D mode (b) and in 3D mode**

Topography of a sputter permalloy sample can be seen in Figure 53. It is visible that the scan through the sample resulted in a continuous sample which is mostly flat. The monotone image confirms that the deposited sample is not rough and contains very few discrepancies.

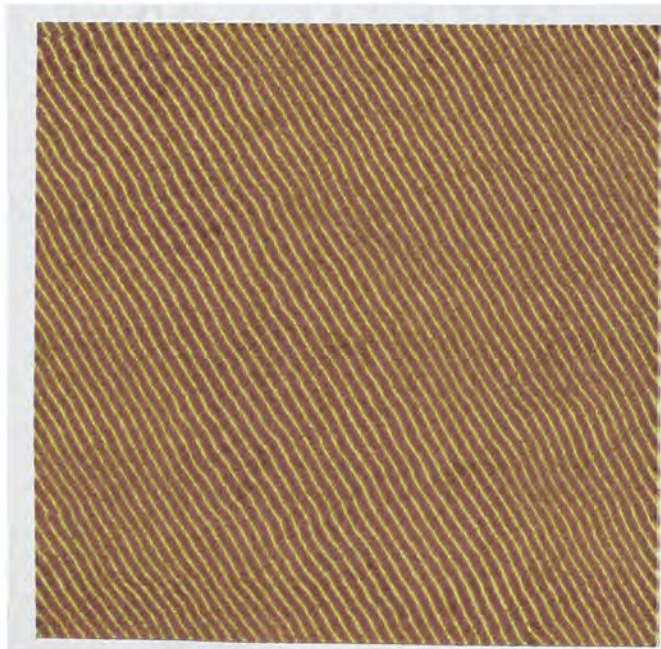


**Figure 56: AFM image of sputtered permalloy at 100 nm**

### 6.3 Magnetic Force Microscopy

The magnetic force microscope was mainly utilized to observe the magnetic properties of the fabricated samples. Scanning of the sample generates fluctuation by the magnetic probe, resulting in precise calculation of the magnetization throughout the examined region. Computational analysis was also performed by the Nanoscope software, providing results in an image form.

Permalloy was deposited on silicon to fabricate the soft underlayers for media recording and reading enhancement. During the deposition process several permalloy samples, magnets were aligned across the sample, inducing a field through the silicon. The result was the phenomenon known as stripe domains. Stripe domains are very thin domains which stretch long through the sample, seen in Figure 54. They are considered to be practical for high speed applications, important for ultra fast reading and writing.



**Figure 57: MFM image of permalloy with domains aligned**



## 6.4 X-Ray Diffraction

Crystallography of the deposited metals was investigated through x-ray diffraction. By means of x-ray diffraction, the contents and crystal structure of a sample may be analyzed. X-ray diffraction was utilized to examine and verify the structures of the isolated metals deposited on a silicon wafer and on the same metals on multilayer samples. The diffractometer, within an x-ray diffraction system, measures twice the angle theta, defined by the angle of diffraction, commonly regarded as 2-theta.

Palladium was deposited through sputtering onto a silicon wafer for crystallographic investigation. Palladium, on a silicon wafer, was observed through x-ray diffraction, shown in Figure 55. The 2-theta scan clearly indicated a cubic face centered crystal structure for the palladium layer, its typical crystallographic arrangement.

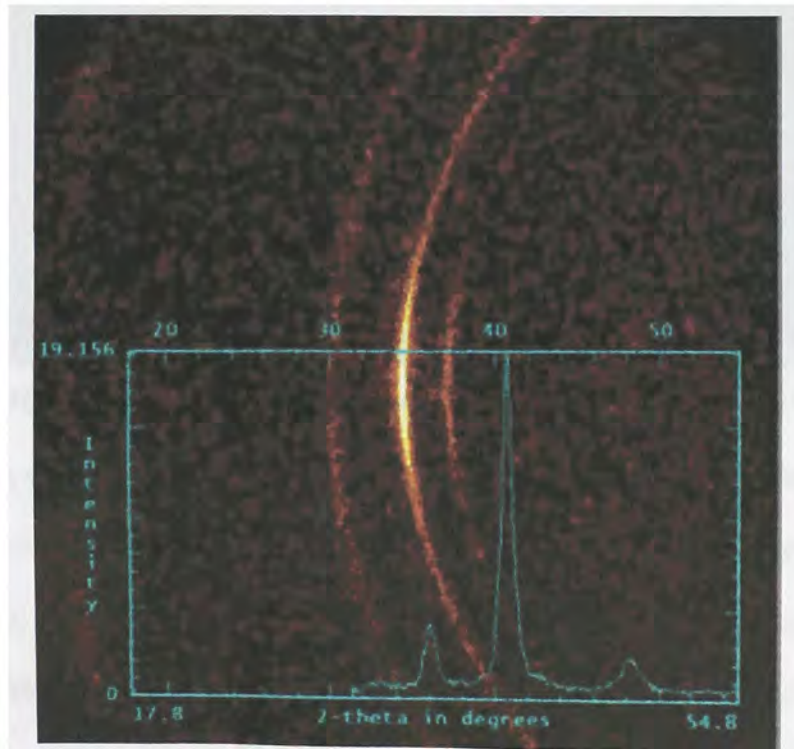
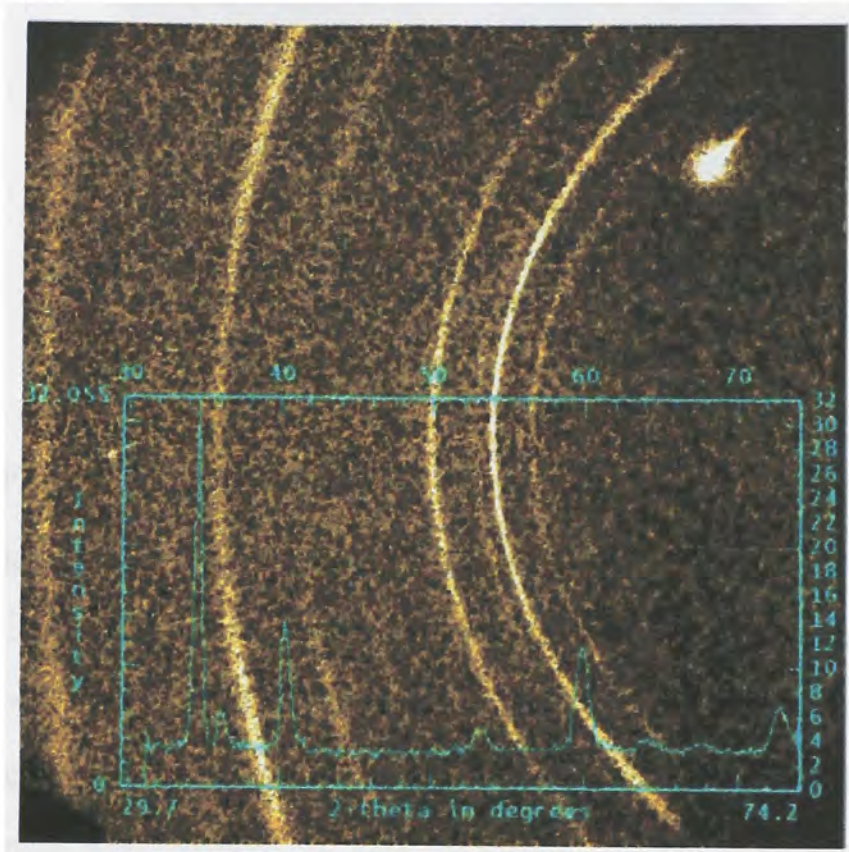


Figure 58: X-ray diffraction on palladium cubic face centered structure

Tantalum was deposited by means of sputtering onto a silicon wafer for crystallographic examination. Tantalum, isolated on a silicon wafer, was observed through x-ray diffraction, illustrated in Figure 56. The 2-theta scan prominently revealed a cubic body centered crystal organization for the tantalum level, its characteristic crystallographic structure.



**Figure 59: X-ray diffraction on tantalum cubic body centered structure**

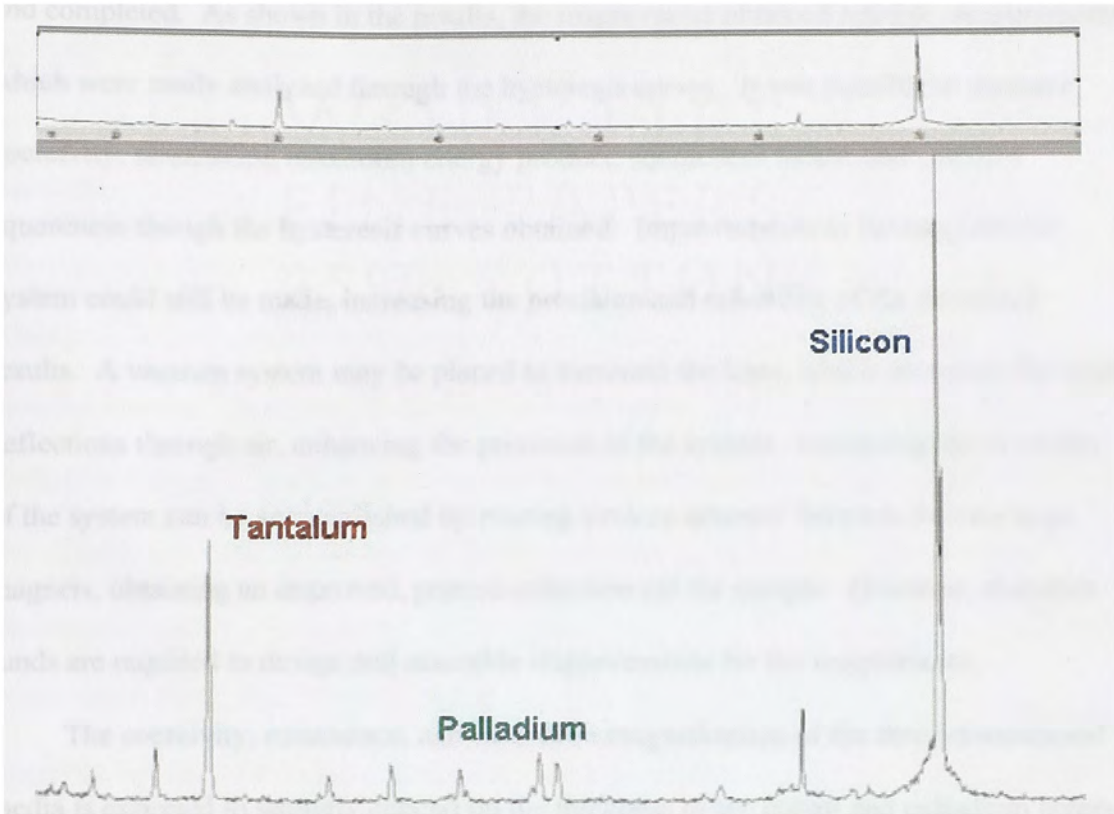
Cobalt was also deposited through sputtering onto a silicon wafer for crystallographic assessment. Cobalt, isolated on a silicon wafer, was observed through x-ray diffraction, as seen in Figure 57. Contrary to the other metals observed, a lack of crystallographic structure for the cobalt layer was observed by the 2-theta scan.



**Figure 60: X-ray diffraction on cobalt**

The analysis of a multilayer sample through x-ray diffraction is illustrated in Figure 58. Prominent metals in the multilayer analyzed are the tantalum seedlayer, palladium nonmagnetic layer, and silicon wafer. Tantalum employed as a thick seedlayer, roughly 30 nm, displayed a clear peak at  $32^\circ$  on the scan, indicating cubic body centered crystal structure. Palladium exploited as a nonmagnetic interlayer of approximately 1 nm, is demonstrated by the small peaks evident near  $40^\circ$  on the scan. These palladium peaks correspond to cubic face centered structure, although they were not prevalent due to the small thicknesses of the palladium layers. The silicon wafer, consisting of the largest thickness within the multilayer sample, was the most apparent structure obtained, at  $70^\circ$  on the scan, during the x-ray diffraction process. Crystal structure on cobalt was undistinguishable within the x-ray diffraction analysis. An explanation for this outcome is that cobalt layers observed were of approximately between 0.3 nm and 0.5 nm, resulting in a thickness of no larger than two atomic layers.

At this thin thickness, insufficient cobalt atoms are available to produce a structured crystal, lacking more atomic layers to emulate bulk properties which would resemble a hexagonal closed packed crystal.



**Figure 61: X-ray diffraction showing peaks for tantalum, silicon, and palladium**

## 7. CONCLUSIONS

The magneto-optical Kerr effect magnetometer setup was successfully developed and completed. As shown in the results, the magnetometer obtained reliable measurements which were easily analyzed through the hysteresis curves. It was possible to measure coercivity, remanence, maximum energy product, squareness factor, and coercive squareness through the hysteresis curves obtained. Improvements to the magnetometer system could still be made, increasing the precision and reliability of the measured results. A vacuum system may be placed to surround the laser, which decreases the small deflections through air, enhancing the precision of the system. Increasing the reliability of the system can be accomplished by placing a micro actuator between the two large magnets, obtaining an improved, precise reflection off the sample. However, abundant funds are required to design and assemble improvements for the magnetometer.

The coercivity, remanence, and saturation magnetization of the three-dimensional media is expected to strongly depend on the thickness of the cobalt and palladium layers. The magnetic layers of lowest thickness are desired for the equation in perpendicular anisotropy, where the perpendicular anisotropy is inversely proportional to the thickness. With a constant palladium nonmagnetic layer, these magnetic characteristics of the media is predicted to be considerably low for a 0.2 nm and 0.3 nm cobalt magnetic layers. The reason for this prediction may be explained by a few reasons due to imperfections in depositing a perfect monolayer of cobalt, virtually impossible by today's standards. First, imperfections in the film may cause the cobalt to separate either in the x or y axis (considering the z axis normal to the plane). These cobalt islands, separated by

palladium, would reduce the exchange coupling of the cobalt atoms deposited for the same monolayer. This effect may lead to several cobalt islands which may not align in the same direction of the net magnetization due to the lack of sufficient exchange energy amongst the cobalt atoms. Additionally, these magnetic characteristics of the 0.2 nm and 0.3 nm cobalt layers may also be low due to imperfections of depositing thin films due to the surface roughness between layers. Interfacial surface anisotropy has been shown to increase as the magnetic and nonmagnetic layers are made thinner; however, surface roughness becomes much more prominent near monolayers, identified by larger surface-to-volume ratios. A step on the palladium or tantalum layer underneath a cobalt layer tends to induce an in-plane uniaxial magnetic anisotropy, with an easy axis parallel to the step direction, resulting in extremely undesirable effect for perpendicular or three-dimensional media. Furthermore, these magnetic characteristics are expected to decrease as the cobalt thicknesses reach near 1 nm. At this range of thicknesses of the cobalt magnetic layers, the interfacial surface anisotropy is reduced, resulting in a decrease of perpendicular anisotropy.

The various fabricated multilayered samples did not exhibit the predicted magnetic behaviors. Magneto-optical Kerr effect microscopy proved unsuccessful in obtaining valid hysteresis curves for those samples. However, it was observed that the magneto-optical Kerr effect magnetometer was functioning properly through the measurements of other magnetic samples. One hypothesis for the absence of glaring perpendicular magnetic characteristics might have been the sputtering system inadequate deposition for ultra thin films. With the lack of extreme heating and rotation during the deposition process, it becomes conceivably difficult to produce excellent quality films, necessary to

produced multilayered media. Large amounts of thickness fluctuations of a layer generate islands of metals and numerous steps between layers, extremely unfavorable for magnetic recording.

With the improvements made to the deposition process, it becomes conceivable to attain and exceed the 1 Tbit/in<sup>2</sup> mark. Through the focused ion beam, it has already become possible to fabricate small patterns in the order of a few nanometers, suitable for extremely small islands sizes necessary to surpass the mentioned mark. Proper thicknesses, in the order of a few Angstroms, have already been attained through sputtering. The only issue arises in obtaining layers with the absence of steps and other imperfections, which extreme heating and rotation of the sample could vastly improve. The tools are already in place to measure and characterize the media, which include the developed magneto-optical Kerr effect magnetometer to measure magnetic characteristics of thin films,

## REFERENCES

- [1] M. H. Kryder, "Data storage technologies for advanced computing," *Scientific American*, vol. 117, pp. 72, 1987.
- [2] F. Liu, "Demonstration of density above 100 Gbit/in<sup>2</sup> with perpendicular magnetic recording," presented at NAPMRC'04, Boulder, Colorado, 2004.
- [3] Wikipedia: The Free Encyclopedia. 2006. Wikimedia Foundation. 2006, <http://en.wikipedia.org>.
- [4] B. M. Moskowitz, "Classes of Magnetic Materials," presented at Environmental Magnetism Workshop, Institute for Rock Magnetism, 1991.
- [5] W. D. Callister, *Materials Science and Engineering: An Introduction*. John Wiley and Sons, 2005.
- [6] K. Fukumoto, "Magnetization reversal dynamics in magnetically coupled trilayer systems," M.S thesis, University of Freie Berlin, 2005.
- [7] E. Chunsheng, D. Smith, J. Wolfe, D. Weller, S. Khizroev, and D. Litvinov, "Physics of patterned magnetic medium recording: Design considerations," *Journal of Applied Physics*, vol. 98, 2005.
- [8] S. Khizroev, Y. Hijazi, N. Amos, R. Chomko, and D. Litvinov, "Physics consideration in the design of three-dimensional and multi-level magnetic recording," *Journal of Applied Physics*, vol. 100, 2006.
- [9] G. Hu, T. Thomson, M. Albrecht, M. E. Best, B. D. Terris, C. T. Rettner, S. Raoux, G. M. McClelland, and M. W. Hart, "Magnetic and recording properties of Co/Pd islands on prepatterned substrates," *Journal of Applied Physics*, vol. 95, 2004.
- [10] K. Kyuno, J. G. Ha, R. Yamamoto, and S. Asano, "The effect of crystal orientation on the magnetic anisotropy of Pd/Co metallic multilayers," *Journal of Physics*, vol. 8, 1996.
- [11] P. Bruno and J. Seiden, "Theoretical investigations on magnetic surface anisotropy," *Journal of Applied Physics*, vol. 64, 1988.
- [12] J. Stohr and R. Nakajima, "Magnetic properties of transition-metal multilayers studied with X-ray magnetic circular dichroism spectroscopy," *IBM Journal of Research and Development*, Vol. 42, Number 1, 1998.
- [13] D. Zhao, F. Lui, D. L. Huber, and M. G. Lagally, "Step-induced magnetic-hysteresis anisotropy in ferromagnetic thin films," *Journal of Applied Physics*, vol. 91, 2002.



- [14] A. Hanuschkin, "Magneto-Optical (MO) Data Storage - application of ultrathin Cobalt layers," presented at Tfy-3.474 Materialphysics Seminar, 2005.
- [15] S.X. Wang and A. Taratorin, *Magnetic Information Storage Technology*, Academic Press, 1999.
- [16] D. Litvinov and S. Khizroev, "Focused ion beams in future nanoscale probe recording," *Nanotechnology*, vol. 13, pp 179-184, 2002.
- [17] Y. Hijazi, R. Ikkawi, N. Amos, A. Lavrenov, D. Doria, N. Joshi, R. Chomko, D. Litvinov, and S. Khizroev, "Patterned soft underlayer for perpendicular recording and 3D magnetic recording systems: Numerical Analysis Perspective," Submitted to the *Journal of Applied Physics*.
- [18] S. Khizroev, N. Amos, Y. Hijazi, N. Joshi, and R. Chomko, "Controversy over the need for a soft underlayer in perpendicular magnetic recording," Submitted to the *Journal of Applied Physics*.
- [19] D. Litvinov, M. H. Kryder, and S. Khizroev, "Physics of perpendicular magnetic recording: Playback," *Journal of Applied Physics*, vol. 93, 2003.
- [20] S. Khizroev and D. Litvinov, *Perpendicular Magnetic Recording*, Kluwer Academic Publishers, 2005.
- [21] B. Lu, T. Klemmer, S. Khizroev, J. K. Howard, D. Litvinov, A. G. Roy, and D. E. Laughlin, "CoCrPtTa/Ti Perpendicular Media Deposited at High Sputtering Rate," *IEEE Transactions on Magnetics*, vol. 37, 2001.
- [22] J. Wrona, T. Stobiecki, M. Czapkiewicz, R. Rak, T. Slezak, J. Korecki, C.G. Kim, "R-VSM and MOKE magnetometers for nanostructures," *Journal of Magnetism and Magnetic Materials*, vol. 272, 2004.
- [23] NT-MDT & State Institute for Physical Problems, Moscow, "Magnetic Force Microscopy (MFM)," 2006, [http://www.ntmdt.ru/SPM-Techniques/SPM-Methodology/Magnetic\\_Force\\_Microscopy\\_MFM/text45.html](http://www.ntmdt.ru/SPM-Techniques/SPM-Methodology/Magnetic_Force_Microscopy_MFM/text45.html).